2017

Synthesis, characterization, and enhanced magnetic properties of iron carbide nanomaterials

Brent M. Williams
Virginia Commonwealth University

Synthesis, characterization, and enhanced magnetic properties of iron carbide nanomaterials

A dissertation submitted in partial fulfillment of the requirements for the degree of Doctor of Philosophy at Virginia Commonwealth University

By

Brent M. Williams

B.S, University of West Georgia 2011

Director: Everett E. Carpenter, Professor of Chemistry

Virginia Commonwealth University

Richmond, Virginia August 2017

Acknowledgments

First off I would like to thank my supervisor, Dr. Everett Carpenter and fellow committee members for giving me the opportunity to further my education and to better myself. These past years have been a major time of growth for me, and I would have never made it without the support of the people I surround myself with, who make me strive to do the best that I can achieve. I want to thank my lab mates who made this journey that much more worthwhile to go through. I thank my mother, father, and sister for all the love and care they have given me throughout the years and being great role models throughout my lifetime. Lastly, I thank my extended family and my wonderful circle of friends and loved ones who have kept me afloat at my times of need.

Table of Contents

List of Figures vii

List of Tables xii

Abstract xiii

Chapter 1-Introduction

1.0 Introduction 1

1.1 Overview 2

1.2. Forms of Magnetism 4

1.2.1 Ferromagnetism 5

1.2.2 Magnetocrystalline Anisotropy....6
1.2.3 Antiferromagnetism....7
1.2.4 Nanomagnetism....8
1.2.5 Shape Anisotropy....10
1.2.6 Exchange Anisotropy....11
1.3 Classic Permanent Magnets....13
1.3.1 AlNiCo....15
1.3.2 Hexaferrites....16
1.3.3 Samarium Cobalt....17
1.3.4 Neodynium Magnets....17
1.4 Alternative Permanent Magnets....18
1.4.1 Mn-Al....18
1.4.2 Mn-Bi....19
1.4.3 Cobalt Carbide....20
1.4.4 α-$Fe_{16}N_2$....21
1.4.5 Co-Pt....21
1.4.6 Fe-Pt....22
1.4.7 Iron Carbide....22
1.5 Nucleation and Growth....23
1.6 Synthesis Methods....24
1.6.1 Thermal Decomposition of Precursor....24
1.6.2 Magnetic nanoparticle synthesis with thermal decomposition....25
1.6.3 Amine Reduction of Nanoparticles....29

1.7 Summary of Objectives.....30

Chapter 2-Characterization.....32

2.0 Instrumentation 33

2.1 X-ray Diffraction 33

2.1.2 Peak Determination 35

2.2 Transmission Electron Microscopy 36

2.3 Scanning Electron Microscopy 37

2.4 Energy Dispersive X-ray Spectroscopy.....38

2.5 X-ray Photoelectron Spectroscopy 39

2.6 Vibrating Sample Magnetometer.....41

2.7 Thermal Gravimetric Analysis.....44

2.8 Raman Spectroscopy & Fourier Transform Infrared Spectroscopy 44

Chapter 3- Synthesis of Fe_7C_3 and Fe_3C Nanostructures with Phase and Morphology Control 47

3.1 Overview/Motivation.....48

3.2 Introduction 48

3.3 Experimental 50

3.3.1 Preparation of Iron Carbonate.....50

3.3.2 Cl^- Induced Synthesis of Iron Carbide.....50

3.3.3 Br^- Induced Synthesis of Iron Carbide.....51

3.3.4 Characterization.....51

3.4 Iron Carbide Synthesis with no Surfactant 52

3.5 Fe_3C and Fe_7C_3 Characterization 54

3.6 Magnetic Analysis 59

3.7 Conclusion 63

Chapter 4-Mechanistic Study if Textured Fe_7C_3 Hexagonal Prisms 64

4.1 Overview/Motivation 65

4.2 Introduction 66

4.3 Experimental 66

4.3.1 Synthesis with different alkyl ammonium chlorides 66

4.3.2 CTAC induced synthesis with different aliphatic amines.....67

4.3.3 Characterization 67

4.4 Mechanistic Study of Fe_7C_3 68

4.5 Thermal Stability of Fe_7C_3 77

4.6 Conclusion 80

Chapter 5-Exchange bias and enhanced anisotropy from exchange coupled Fe_3C/CoO nanoaggregates 81

5.1 Overview/Motivation 82

5.2 Introduction 82

5.3 Experimental 83

5.3.1 Synthesis of Fe_3C Nanoparticles 83

5.3.2 Synthesis of Fe_3C/CoO nanoaggregates 84

5.3.3 Instrumentation 84

5.4 Results and Discussion 85

5.5 Conclusion 94

Chapter 6-Synthesis of spring exchange coupled $Fe_7C_3/SrFe_{12}O_{19}$ composites 95

6.0 Overview/Motivation 96

6.1 Introduction 96

6.2 Experimental 97

6.2.1 Sonochemical synthesis of $SrFe_{12}O_{19}$ particles.....98

6.2.2 Partial reduction of $SrFe_{12}O_{19}$ particles 99

6.2.3 Instrumentation 99

6.3 Results and Discussion 99

6.3.1 Partial Reduction of $SrFe_{12}O_{19}$.....99

6.3.2 Time Study 104

6.4 Conclusion 109

Chapter 7-Summary 110

List of Figures

Chapter 1-Introduction

Figure 1.1.1 History of steel, ferrites, AlNiCo, Sm-Co, and neodymium magnets with development of energy product $(BH)_{max}$. Inset pie chart shows the estimated world market percentage for each of the materials. 3

Figure 1.2.1 Generic hysteresis loop for (a) a ferromagnetic and (b) antiferromagnetic material. 5

Figure 1.2.1.1 A schematic of exchange interaction. Due to Hund's rule spins prefer to orient themselves in a parallel fashion lowering their Coulomb energy (Modified from Ref 7).[1] 6

Figure 1.2.2.1 M-H curves of single crystalline iron aligned upon different crystallographic planes (Modified from Ref 5). 7

Figure 1.2.4.1 Schematic of two adjacent domains with a domain wall which slowly orientates its spins 180° in the opposite direction. 9

Figure 1.2.4.2 (a) The schematic represents the change in particle radius and domains influences coercivity. (b) 6 nm, 13 nm, and 23 nm Sm_2Co_{17} (Modified from Ref).....10

Figure 1.2.6.1 Hysteresis curve with exchange bias. (1) Is the material above the Néel temperature an applied field H. (2) Material below the Néel temperature. (3) Material with an applied reverse field. (4) Material with a applied field back to original state. 12

Figure 1.2.6.2 Example of spring exchange magnet with M-H curves of cobalt ferrite and cobalt ferrite/FeCo couple magnets. 12

Figure 1.3.1 M-H curves of typical permanent magnets including Sm-Co, Nd-Fe-B, AlNiCo, and ferrites. 14

Figure 1.3.2. Periodic table color coated for prices of elements from very cheap, cheap, moderately inexpensive, expensive, and very expensive. The magnetic elements are illustrated in bold. 15

Figure 1.4.2.1 M-H curves of MnBi alloy showing an enhanced Hc due to the positive temperature coefficient from 300 K to 400 K. 19

Figure 1.4.3.1 (a) Ms and H_c with change in Co_2C:Co_3C volume ratio. (b) $(BH)_{max}$ versus coercivity for AlNiCo, strontium ferrite, and cobalt carbide. 20

Figure 1.5.1 LaMer diagram schematic. 23

Figure 1.6.2.1 (a) Park et al's synthesis of iron oxide utilizing different bp solvents to get nanoparticles with 5 nm, 9 nm, 12 nm, 16nm, and 22 nm. (b) Zero field cool curve for 5 nm, 9 nm, 12 nm, 16 nm, and 22 nm nanoparticles within a 100 Oe field. 26

Figure 1.6.2.2 (a) Illustration and M-H curve of superparamagnetic iron oxide. (b) Illustration and TEM image of aggregation of nanoparticles. (c) TEM image and M-H curve of ferromagnetic nanoworms. 27

Figure 1.6.2.3 (left) (a,b) cubic, (c,d) truncated cubic, (e,f) cuboctahedral, (g,h) truncated, octahedral, and (i,j) octahedral transmission electron microscopy micrographs. (right) (a) M-H curves for cubic, truncated cubic, cuboctahedral structures. (b) M-H curves for cuboctahedral, truncated, octahedral, and octahedral structures. 29

Figure 1.6.3.1 Mechanism of silver reduction/oleylamine dehydrogenation which results in silver (0) nanoparticles stabilized by amine, imine, or cyano group. 30

Chapter 2-Characterization

Figure 2.1.1 Schematic of Bragg's law where an incident x-ray is diffracted at angle Θ with a wavelength equivalent to a multiple of the incident wavelength. 35

Figure 2.2.1 Basic instrumental components of (a) TEM and (b) SEM. 37

Figure 2.4.1 (a) EDS emission of x-ray from relaxation of electron from outer shell to inner shell. (b) X-ray emission of photoelectron for XPS. 39

Figure 2.5.1 Instrumental schematic of XPS composed of the sample chamber and the concentric hemispherical analyzer. 41

Figure 2.6.1 Main components of a VSM which consist of an electromagnet, pickup coils, piezoelectric material, and a sample holder. 42

Figure 2.8.1 Instrumentation for Fourier transformation infrared spectroscopy which includes an IR source, a moving and fixed mirror, beam splitter, sample cell, and IR sensor. 45

Chapter 3- Synthesis of Fe7C3 and Fe3C Nanostructures with Phase and Morphology Control

Figure 3.4.1. Thermal gravimetric analysis of iron carbonate (dotted line) and iron fumarate (solid line). 52

Figure 3.4.2. Zhang et al. report of increase crystallinity in nanoparticle synthesis with addition of halogen species. 53

Figure 3.5.1. X-ray diffraction patterns for the Fe_xC nanoparticles made (a) without a surfactant, (b) CTAC, and (c) CTAB. References for Fe_3C (PDF 01-089-2722), Fe_7C_3 (PDF 01-089-7273), and Fe_3O_4 (PDF 01-075-0449) are shown for comparison. 55

Figure 3.5.2. SEM images of various phases of Fe_xC samples synthesized using (a) 18.3, (b) 9.15, (c) 4.58, and (d) 2.29 mM CTAC. 57

Figure 3.5.3. (a) Hysteresis of Fe_3C synthesized with CTAB. (b) Scanning electron micrograph of Fe_3C synthesized with CTAB. 58

Figure 3.6.1. M-H curves at 300 K for the samples synthesized at CTAC concentration ranging from 18.3 mM (solid), 9.15 mM (dotted), 4.58 mM (dashed), and 2.29 mM (dashed and dotted). 59

Figure 3.6.2. Extended magnetics study on iron carbide sample synthesized with 4.58 mM CTAC. (a) FC with 500 Oe field, and ZFC study with a 5 K/min sweep rate. (b) Hysteresis at temperatures ranging from 50-300 K. 62

Figure 3.6.3. Extended magnetic study of the Fe_7C_3 hexagonal prisms. (a) FC with 500 Oe field, and ZFC with a 5 K/min sweep rate (b) Hysteresis at different temperatures ranging from 50 K – 300 K. 63

Chapter 4-Mechanistic Study if Textured Fe_7C_3 Hexagonal Prisms

Figure 4.4.1. (a) X-ray diffraction samples synthesized different solutions: octadecylamine, hexadecylamine, tetradecylamine, and dodecylamine with 6.25 mM CTAC with 0.152 g iron acetate. (b) X-ray diffraction of samples synthesized with different ammonium Cl^- salts including CTAC, cetyl pyridium chloride (CPC), distearyldimonium chloride (DSC), and ammonium chloride. Reference patterns for hcp Fe_7C_3, orthorhombic Fe_3C, and fcc Fe_3O_4 are presented below the patterns in both figures. 68

Figure 4.4.2. SEM micrographs of iron carbide synthesized in various aliphatic amines which include (a) octadecylamine, (b) hexadecylamine, (c) tetradecylamine. Figure (d)-(h) represent synthesis of carbide using different Cl^- salts: (d) DSC, (e) CPC, (f) ammonium chloride, (g) and (h) CTAC. 70

Figure 4.4.3. (a) XRD thermal study of the Fe_7C_3 system from 335 °C to reflux at 365 °C for 15 minutes. References for Fe_3C (PDF 01-089-2722), Fe_7C_3 (PDF 01-089-7273), and Fe_3O_4 (PDF 01-075-0449) are shown for comparison. SEM thermal study of formation of Fe_7C_3 prisms from 335 °C to reflux at 365 °C. 72

Figure 4.4.4. Solvent FTIR study taken at temperatures 335 °C, 345 °C, 365 °C, and at reflux for 5 minutes. Figure on the left showing the range from 500 to 1200 cm^{-1}. The right figure shows the range from 1500 to 1700 cm^{-1}. 73

Figure 4.4.5. (a) X-ray diffraction pattern (aligned) prepared by aligning the sample with a neodymium magnetic with the face of the plate's oriented perpendicular to the sample holder. (disoriented) Diffraction pattern with no sample preparation. (b) Transmission electron micrograph of a single Fe_7C_3 hexagonal plate with an inset of the EELS diffraction pattern of the single crystalline structure. 74

Figure 4.4.6. M-H curves for the samples long axis aligned parallel and vertical to the external field. 76

Figure 4.5.1. High temperature x-ray diffraction study of decomposition of Fe_7C_3 starting with 25 °C, 500 °C, and post-anneal (top of figure). (b) TGA-IR of Fe_7C_3 under 100 ml/min N_2 set to 500 °C. 77

Figure 4.5.2. High temperature x-ray diffraction study of decomposition of Fe_7C_3 with 25 °C followed by 500 °C, 400 °C, 300 °C, 200 °C, and post-anneal. 79

Figure 4.5.3. SEM image of Fe_7C_3 after HTXRD Study (a) and (b) of post-annealed samples with fast cooling represented in Figure 4.5.1 respectively. Image (c) and (d) are from the post-annealed sample but upon slow cooling represented in Figure 4.5.2 respectively. 80

Chapter 5-Exchange bias and enhanced anisotropy from exchange coupled Fe_3C/CoO nanoaggregates

Figure 5.4.1. X-ray diffraction of the (a) Fe_3C/CoO and (b) Fe_3C sample as well as the reference patterns for (c) Fe_3C (PDF 01-089-2722) and (d) CoO (PDF 01-089-7099). 85
Figure 5.4.2 Transmission electron microscope images of (a) Fe_3C, (b) Fe_3C/CoO. EELs mapping was done on Fe3C/CoO were (c) shows the sample under regular imaging, (d) shows mapping were the red denotes iron and cyan denotes cobalt. 86

Figure 5.4.3 Raman spectra of Fe_3C sample which shows the graphite band (1580 cm^{-1}) and disorder band (1350 cm^{-1}). 87

Figure 5.4.4 XPS 2p spectra of (a) cobalt and (b) iron from the Fe_3C/CoO sample. 89

Figure 5.4.5 XPS Survey scan of Fe_3C/CoO material with a table of the atomic percentages. 89

Figure 5.4.6 (a) O1s, and (b) C1s XPS spectra for Fe_3C/CoO sample. 90

Figure 5.4.7 M-H curves at 300 K for iron carbide before coating (solid line) and after coating (dashed line) with CoO. 91

Figure 5.4.8 (a) M-T curves of corresponding Fe_3C/CoO sample with a sweep rate of 5 K min^{-1}. (b) M-H curves taken from 50-300 K for Fe_3C/CoO sample. 92

Figure 5.4.9 (a) Exchange bias field and (b) coercive force taken at temperatures ranging from 50-300 K without an external field. 93

Chapter 6-Synthesis of spring exchange coupled $Fe_7C_3/SrFe_{12}O_{19}$ composites

Figure 6.1.1 Depiction of strontium ferrite partially reduced to iron carbide over time. 98

Figure 6.4.1.1 X-ray diffraction of $SrFe_{12}O_{19}/Fe_7C_3$ nanocomposites. (a) $SrFe_{12}O_{19}/Fe_7C_3$ at reflux for 10 minutes. (b) $SrFe_{12}O_{19}/Fe_7C_3$ reaction at reflux for 20 minutes. (c) Strontium ferrite seeds synthesized at 1000 C in air. (d) Strontium ferrite and (e) Fe_7C_3 reference patterns. 101

Figure 6.4.1.2 Scanning electron micrographs of (a) strontium ferrite post annealing, (b) $SrFe_{12}O_{19}/Fe_7C_3$ 10 minutes at reflux, and (c) $SrFe_{12}O_{19}/Fe_7C_3$ 20 minutes at reflux.....101

Figure 6.4.1.3 Room temperature M-H curves for strontium ferrite synthesized at 1000 °C, strontium ferrite/iron carbide composites synthesized at 10 and 20 minutes at reflux, and Fe_7C_3 reference.....103

Figure 6.4.2.1 X-ray diffraction of aliquots from strontium ferrite reduction in oleylamine taken at (c) 335 °C, (d) 345 °C, (e) 355 °C, (f) 360 °C, (g) 360 °C 30 min, (h) 360 °C 60 min with (a) hexagonal Fe_7C_3 and (b) $SrFe_{12}O_{19}$ reference pattern.....105

Figure 6.4.2.2 (a) FT-IR of aliquots taken from ferrite reduction. (b) Bar graph of percent composition of aliquots taken over a temperature range of strontium ferrite and iron carbide calculated from x-ray diffraction and normalized N-H stretch at 790 cm^{-1}.....106

Figure 6.4.2.3 (a) Magnetization (left axis) and coercivity (right axis) versus temperature for samples taken at 335, 345, 355, and 360 °C. (b) Magnetization (left axis) and coercivity (right axis) versus time for samples taken at reflux at time 0, 30, and 60 minutes.

Figure 6.4.2.4 M-H curve of strontium ferrite/iron carbide composites at time 0, 30 min, and 60 minutes at reflux. The strontium original strontium ferrite is plotted as a reference.....108

List of Tables

Chapter 1-Introduction

Table 1.3.1 Structure type, and magnetic properties which include M_s, H_c, K_1, T_c for standard permanent magnets. 14

Chapter 3- Synthesis of Fe_7C_3 and Fe_3C Nanostructures with Phase and Morphology Control

Table 3.5.1. Fe_7C_3 and Fe_3C phase % and crystallite size (nm) for each [CTAC] mM. 56

Table 3.6.1. Magnetic saturation, coercivity, Mr/Ms, and domain size obtained from the M-H curves based on the CTAC concentrations. 61

Chapter 4-Mechanistic Study if Textured Fe_7C_3 Hexagonal Prisms

Table 4.5.1. Energy dispersive x-ray spectroscopy of Fe_7C_3 before and after high temperature x-ray diffraction study. 79

Chapter 5-Exchange bias and enhanced anisotropy from exchange coupled Fe_3C/CoO nanoaggregates

Table 5.4.1 Energy dispersive spectroscopy elemental analysis of the Fe_3C sample and the Fe_3C/CoO. 88

Chapter 6-Synthesis of spring exchange coupled $Fe_7C_3/SrFe_{12}O_{19}$ composites

Table 6.4.1.1 Magnetic values from M-H curve observed in Figure 6.4.1.3. 103

Table 6.4.2.1 Crystal phase percentage of diffraction patterns from time study, calculated from Rietveld refinement. 105

Abstract

SYNTHESIS, CHARACTERIZATION, AND ENHANCED MAGNETIC PROPERTIES OF IRON CARBIDE NANOMATERIALS.

By: Brent Williams, Ph.D

A dissertation submitted in partial fulfillment of the requirements for the degree of Doctor of Philosophy at Virginia Commonwealth University

Virginia Commonwealth University, 2017

Director: Dr. Everett Carpenter

Professor of Chemistry

Permanent magnets are classified as hard magnetic materials with the main purpose of generating flux for applications such as electric motors, turbines, and hard drives. High coercivity, magnetic remanence, and saturation values with high stability are some of the requirements for permanent magnets. Rare-earth magnets including neodymium and samarium based magnets are known to have superior magnetic properties due to their high magnetocrystalline anisotropy. However, due to the price of rare-earth materials development of alternate permanent magnets composed of

inexpensive materials is an ongoing process. Previously cobalt carbide (Co_xC) have shown promise as a potential rare-earth free magnet alternative with magnetic properties comparable to that of hexaferrite materials. Unfortunately, Co_xC magnets have a low magnetic saturation (50 emu g^{-1}) which drastically lowers its energy product. Alternatively, iron carbide has a rather high bulk magnetization value of 140 emu g^{-1} and is composed of naturally abundant materials. The sole issue of iron carbide is that it is considered an intermediate magnet with properties between those of a hard and a soft magnetic material.

The main focus of this work is the enhancement of the hard magnetic properties of iron carbide through size effect, shape anisotropy, magnetocrystalline anisotropy and exchange anisotropy. First a wet synthesis method was developed which utilized hexadecyltrimethylammonium chloride to control particle size, shape, and crystal structure to manipulate the magnetic properties of iron carbide. With this method a semi-hard 50 nm orthorhombic Fe_3C phase and a magnetically soft single crystal hexagonal Fe_7C_3 structure with texture-induced magnetic properties were developed. The properties for both materials were further enhanced through formation of exchange bias Fe_3C/CoO nanoaggregates and spring exchange coupling of the ferromagnetically hard and soft phases of $Fe_7C_3/SrFe_{12}O_{19}$. A 33% increase in coercivity was observed at room temperature for the antiferro/ferromagnetic Fe_3C/CoO in comparison to the bare Fe_3C. While iron carbide enhanced the magnetic saturation and remanence of strontium ferrite. This work concludes that with further development of iron carbide nanocomposites they may be employed as future alternative permanent magnets.

Chapter 1. Introduction

1.1. Overview

The development of permanent magnets has been essential for the evolution of technology since the cultivation of the first permanent magnet at the end of the 19th century. They have found practicality within motors, turbines, computers, electronic gadgets, and electronic generation industries.[2] Due to their ability to perform as green products, such as lowering the amount of CO_2 emission from hybrid/electric vehicles, permanent magnets have been increasingly employed. Within computers and electronic devices, the increased efficiency of magnets have also made it possible to improve the memory and speed of computers. For example, in 1984 computer disk drives had approximately 10 MB of storage with an access time greater than 60 ms; whereas in modern times, computers have external hard drives with storage space of a few hundred gigabytes, with an access time of 8 to 12 ms.[3] The external hard drives are also smaller which lead to the revolution of small hand held devices such as cellular devices, hand held game consoles, and compact computers.

Permanent magnets in majority of applications are used to generate magnetic flux, but only a few materials have been employed for industrial use. The most prevalent materials for permanent magnets include hexagonal ferrite, AlNiCo, SmCo, and neodymium magnets. Figure 1.1.1 represents the development history where BH_{max} represents the magnetic energy product exerted from these materials. Figure 1.1.1 shows the rare-earth permanent magnets

which began in the 1960s with the discovery of samarium-cobalt to dominate in strength in comparison to the non-rare earth materials.[3] Due to the high efficiency of these rare-earth materials the use of these materials have liberated the industry. The inset of Figure 1.1.1 shows the percentage of sales of each magnet where the neodymium magnets contain the majority of the percentage.

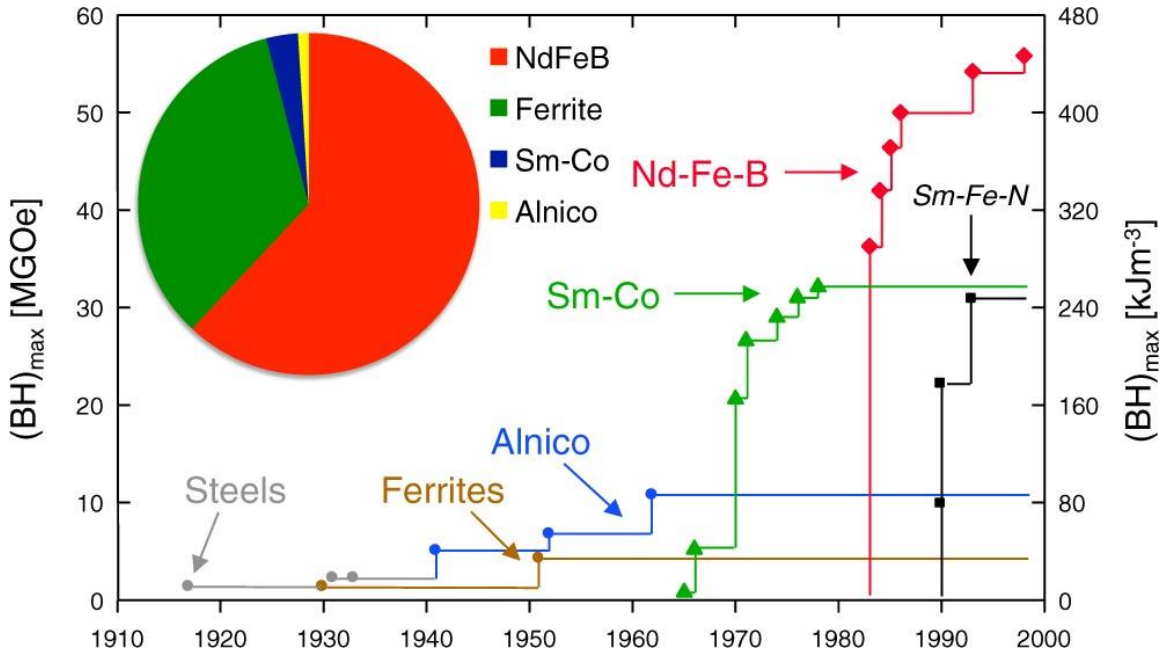

Figure 1.1.1 History of steel, ferrites, AlNiCo, Sm-Co, and neodymium magnets with development of energy product $(BH)_{max}$. Inset pie chart shows the estimated world market percentage for each of the materials.[3]

Unfortunately some rare-earth materials such as samarium make SmCo magnets less attractive for custom use. Moreover, in addition to rising costs from imposed exportation restriction, neodymium magnets have low stability and are normally doped with expensive rare-earth metals such as dysprosium and terbium. .

With the increase price of rare-earth magnets alternative non-rare earth magnets have been a new topic of interest. Nanomaterials, such as textured nanocomposites, have the potential to be the future of permanent magnets. The enhancement of nanomaterials includes controlling

particle size, shape, as well as controlled doping and development of bimetallic materials to enhance properties needed to create inexpensive permanent magnets.

1.2 Forms of Magnetism

Magnetic moment is the force exerted from a material equivalent to the net direction of unpaired electrons. For a certain material the net magnetic moment is proportional to its mass defined as magnetic moment density or magnetization (M unit's emu g^{-1}). An example of a hysteresis loop is shown in Figure 1.2.1a which represents a basic way to determine intrinsic properties of a material by studying changes in magnetization under an external field (H units Oersted). There are three main periods analyzed when interpreting a hysteresis loop which include magnetic saturation (M_s), magnetic remanence (M_r), and coercivity (H_c). When an external field is applied great enough to align the free spins in one direction its saturation (M_s) has been reached. Once saturation has been reached a field in the opposite direction or demagnetization field is exerted on the sample. Reducing the field strength to H = 0, any magnetization left is defined as remanence (M_r). Coercivity (H_c) is the amount of reverse field needed to demagnetize a magnet therefore its net magnetization is equal to zero. At this point the process is repeated reaching a negative saturation value and applying a field in the opposite direction forming a full hysteresis. As observed in Figure 1.2.1b, some types of magnetism don't form a hysteresis loop, therefore the shape of the hysteresis loop, saturation, remanence, and coercivity values, can be used to subdivide magnetism into different areas.[4]

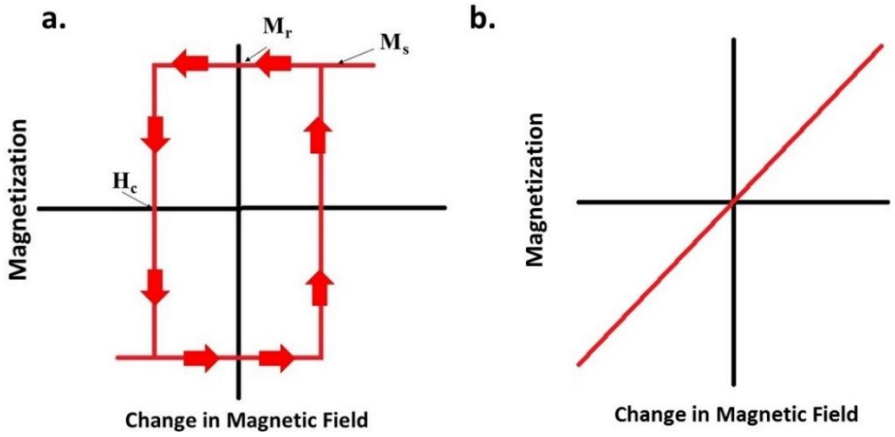

Figure 1.2.1 Generic hysteresis loop for (a) a ferromagnetic and (b) antiferromagnetic material.

Magnetism can be broken up into many sub groups. Diamagnetism is the most universal kind of magnetism, in which the material opposes a magnetic field. In most materials this form of magnetism has a very small contribution from repulsion from core electrons within an atom. Paramagnetism on the other hand, has at least one free electron which is oriented in the direction of an applied magnetic field, but loses its orientation once the field is removed therefore it doesn't retain magnetization without an external field.

1.2.1 Ferromagnetism

While diamagnetic and paramagnetic depend on characteristics of individual atoms or complexes, ferromagnetism and antiferromagnetism depend on the electronic spins and cooperative behavior of many unit cells. In ferromagnetism the free spins are oriented parallel to one another without the need of an external magnetic field, therefore they have a net magnetic moment at H = 0. Ferromagnetism relies on Hund's rule which states that due to repulsion forces of neighboring electrons, interatomic electrons prefer to orient themselves parallel to one another to decrease

Coulombic repulsion. Exchange interaction governs the interatomic ordering of spins of electrons. Figure 1.2.1.1 shows the relation between Coulomb energy and exchange interaction.[1]

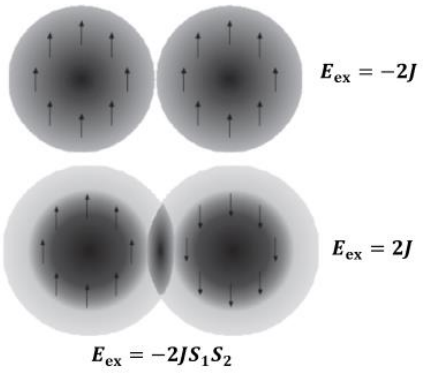

Figure 1.2.1.1 A schematic of exchange interaction. Due to Hund's rule spins prefer to orient themselves in a parallel fashion lowering their Coulomb energy (Modified from Ref 1).[1]

Exchange and Coloumb energy have a relation of $E_{ex} = -2JS_1S_2$ where E_{ex} is the Coloumb energy, J is the exchange constant and S_1 and S_2 are spins of neighboring atoms. When the exchange constant is positive parallel spins are favored leading to ferromagnetism, while a positive J favors antiparallel orientation of spins and higher Coloumb energy (aniferromagnetism).[1, 4] Each ferromagnetic material has a Curie temperature which is defined as the transition from ferromagnetism to paramagnetism.

1.2.2 Magnetocrystalline Anisotropy

Ferromagnetism is not only governed by interatomic interactions but interactions of the lattice structure as a whole, known as magnetocrystalline anisotropy. This phenomenon occurs due to the preference for the net magnetization of a structure to align upon a certain axis of a crystal structure within an external field. The crystallographic axis which saturation is reached within the

lowest applied external field is known as the easy axis. Therefore uniaxial crystal structures such as hexagonal, tetragonal, as well as asymmetric crystal structures (orthorhombic) tend to have higher magnetocrystalline anisotropy in comparison to symmetric structures such as cubic lattice structures. Figure 1.2.2.1 shows an example of M-H curves of a single crystal of iron magnetically aligned upon its easy, medium and hard axis. The easy axis of [100] saturates at a much lower field in comparison to the curves aligned with the [110] and [111] plane. Materials which are said to have high magnetocrystalline anisotropy are normally labeled as hard magnets, displaying large coercivity (>1000 Oe) values due to difficulty to flip spins from this axis. Materials having low magnetocrystalline anisotropy normally have a low coercivity (<125 Oe) and are consider soft magnets.[1, 4]

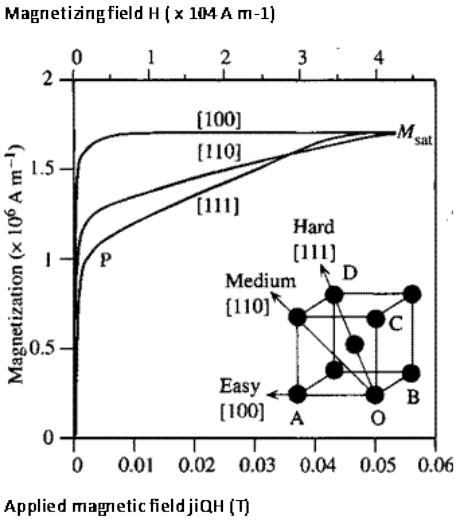

Figure 1.2.2.1 M-H curves of single crystalline iron aligned upon different crystallographic planes (Modified from Ref 5).[5]

1.2.3 Antiferromagnetism

Antiferromagnetism is an ordered magnetism where the free spins of a structure orient themselves antiparallel to one another leading to a net zero moment with zero magnetic field applied. From Figure 2, when the exchange constant is negative this leads to a positive Coulomb energy and antiferromagnetic ordering. Antiparallel spins are preferred with dipolar interaction which is long range ordering upon atoms. The most popular form of antiferromagnetism occurs due to an intervening ligand between metal centers by a mechanism called superexchange. Superexchange occurs when the metal center of one metal induces polarization on an occupied orbital of a ligand which leads to antiparallel spins on the adjacent metal bound to that ligand.[6] This mechanism occurs in many transition metal oxides such as MnO, FeO, CoO, and NiO. In order to get antiferromagnetism the material must be below its Néel temperature, or the transition temperature from antiferromagnetic to paramagnetic upon heating. Hysteresis curves below the Néel temperature usually have a linear relationship between magnetization and the applied fields due to spin canting under applied fields.

1.2.4 Nanomagnetism

There are three types of energies which play a vital role in a materials magnetic configuration, exchange energy, magnetocrystalline anisotropy, and magnetic dipole energy. For bulk materials exchange and dipolar interaction have contradicting forces, one wanting to align spins parallel and the other in an antiparallel fashion. In order to lower the magnetostatic energy of the material there is a compromise in the forms spontaneous magnetization regions called domains separated by

domain walls illustrated in Figure 1.2.1.4. A domain wall is a gradual reorientation of the spins by 180 ° therefore the adjacent domain is oriented in the opposite direction.[1]

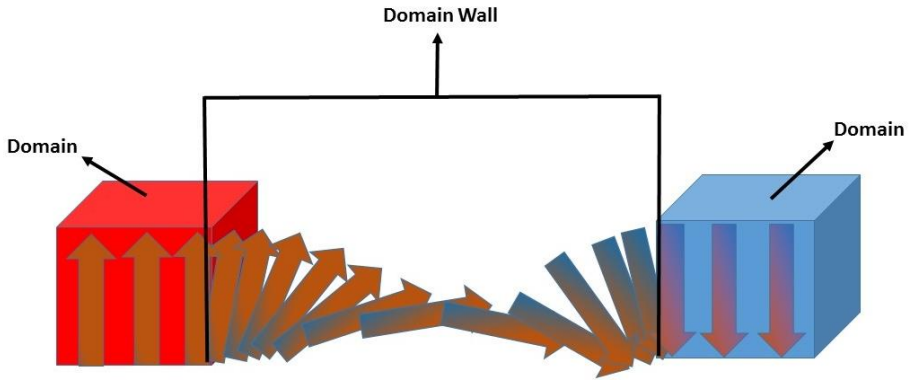

Figure 1.2.4.1 Schematic of two adjacent domains with a domain wall which slowly orientates its spins 180° in the opposite direction.

The amount of domains and domain walls increase with particle size thus decreasing the coercivity due to antiparallel spins with a net M = 0 without an external field. As particle size decreases, the formation of domains decrease until it is energetically favored to have a single domain with a maximum magnetic field illustrated in Figure 1.2.4.2a. Further decrease in particle size leads to superparamagnetism, where thermal fluctuations are enough to flip spins. These magnetics respond to an external field with a coercivity close to zero. Figure 1.2.4.2b shows an example of how size effects the coercivity of the material with an increase in H_c with an increase in Sm_2O_{17} particle size from 6 nm to 23 nm.

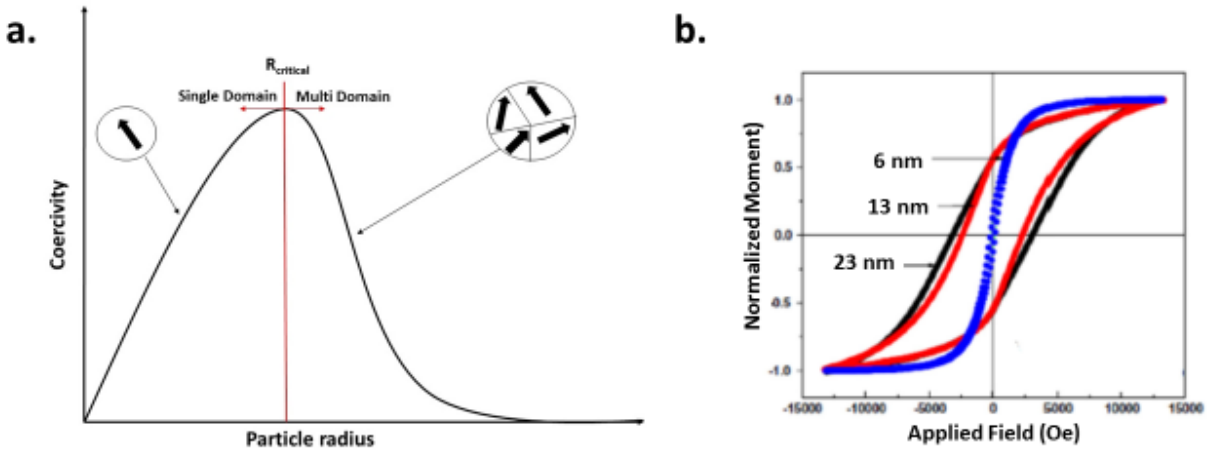

Figure 1.2.4.2 (a) The schematic represents the change in particle radius and domains influences coercivity. (b) 6 nm, 13 nm, and 23 nm Sm_2Co_{17} (Modified from Ref).[7]

1.2.5 Shape Anisotropy

Shape anisotropy takes into account the change in magnetic properties upon magnetization through the shortest and longest dimensions of a ferromagnetic body. In a perfectly spherical nanoparticle its magnetostatic energy is evenly distributed throughout its surface due to the even distribution of charged magnetic poles. Elongating nanostructures such as ellipsoids and wires have their oppositely charged magnetic poles spread across its long axis therefore decreasing its magnetostatic energy (lower demagnetization field) while the magnetostatic energy among the short axis is much higher (higher demagnetization field). This phenomenon can only occur in low or single domain materials due to the fact each domain has its own magnetostatic energy therefore polar interactions occur across individual domains within the material. This decrease in contribution from the demagnetization field results in an increase coercivity therefore wire, elliptical shaped particles have shown promise in the field of permanent magnets.

1.2.6 Exchange Anisotropy

Exchange bias anisotropy occurs from exchange interaction between the interface of a ferromagnetic and antiferromagnetic layer which results in an increase coercive field along the magnetic field axis direction. A schematic of this phenomenon is shown in Figure 1.2.6.1, with illustrations of exchange interactions within the bilayer. In (1) An external field is applied to the sample to saturate the spins of the ferromagnetic material. (2) Cooling below the Néel temperature, the spins of the antiferromagnetic material align with the ferromagnetic at the interface due to exchange interaction. (3) When a reverse field is applied on the material extra torque is applied on the interfacial spins, therefore a larger field is needed to flip the spin causing an increase in coercivity. (4) Due to the formation of a domain it is much easier to realign the spins upon another field reversal, resulting in a shift in the hysteresis loop. Work in this field has shown switch from bulk to nanomaterials has varying effects on exchange bias. General trends have shown only above a critical thickness layer of antiferromagnetic material will exchange bias occur, and a decrease in exchange bias may occur with increase ferromagnetic layer thickness. This interaction is normally used for spin valves used for magnetic memory.[1, 4]

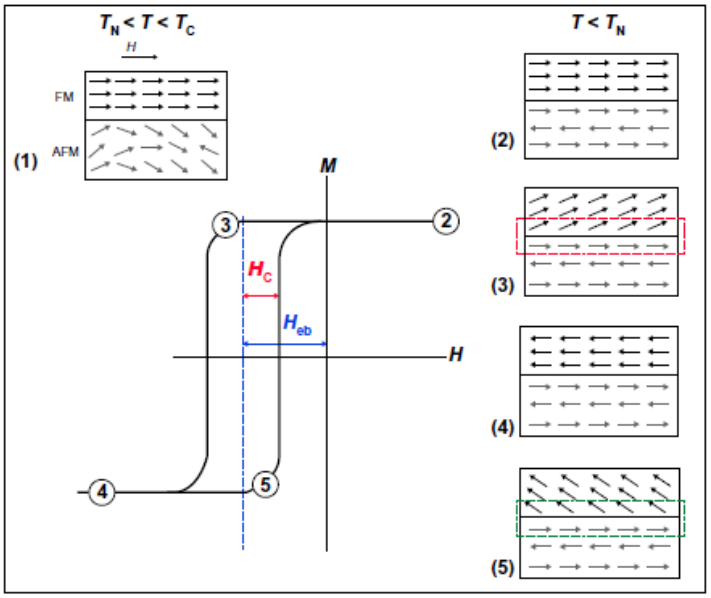

Figure 1.2.6.1 Hysteresis curve with exchange bias. (1) Is the material above the Néel temperature an applied field H. (2) Material below the Néel temperature. (3) Material with an applied reverse field. (4) Material with a applied field back to original state.[1]

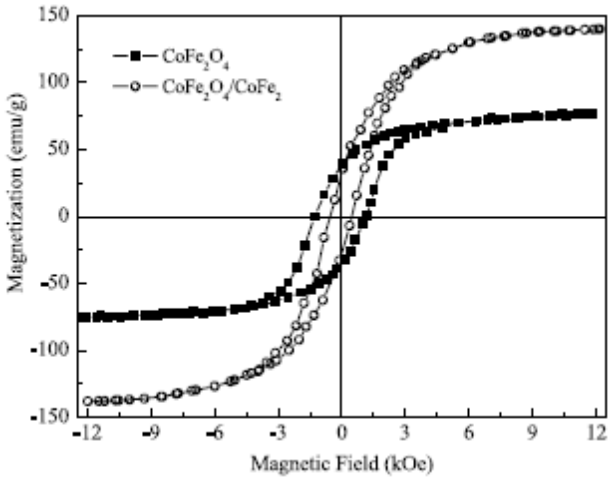

Figure 1.2.6.2 Example of spring exchange magnet with M-H curves of cobalt ferrite and cobalt ferrite/FeCo couple magnets.[8]

Similar to exchange bias exchange spring magnets which rely on exchange interactions between the boundaries of a two-phase system for its intrinsic properties. Spring magnets are used to enhance the energy product needed for hard magnetic materials. Energy product is based off the area under the hysteresis curve therefore a high H_c and M_s value is needed. A hard material with

a low saturation value is normally paired with a soft material to improve its energy product. Inexpensive hard materials such as hexagonal ferrites or cobalt ferrites which have relative low magnetic saturation values (approximately 50 emu g^{-1}) have been paired with soft materials to compete with rare-earth magnets which have much larger energy products. An example is an exchange spring magnet is observed in Figure 1.2.6.2 where the addition of the high susceptibility FeCo is exchange coupled to cobalt ferrite which increased the area under the hysteresis curve.[8] Synthesis methods for forming spring magnets include co-precipitation, thermal decomposition, metal reduction, and microwave assisted methods.[9]

1.3 Classic Permanent Magnets

In the past century development of 4 main permanent magnets have been established which include, AlNiCo, hexagonal ferrites, SmCo, and neodymium magnets. Figure 1.3.1 represents a M-H curve of the different type of magnets for comparison while Table 1.3.1 includes general information on their magnetic properties which include crystal structure, Curie temperature, magnetization, and magnetocrystalline anisotropy constant values for comparison. As cost plays an important role for selectivity of permanent magnets Figure 1.3.2 shows the periodic table with the price range of each element. Within this section the properties and developments of each of the classic permanent magnets will be discussed.

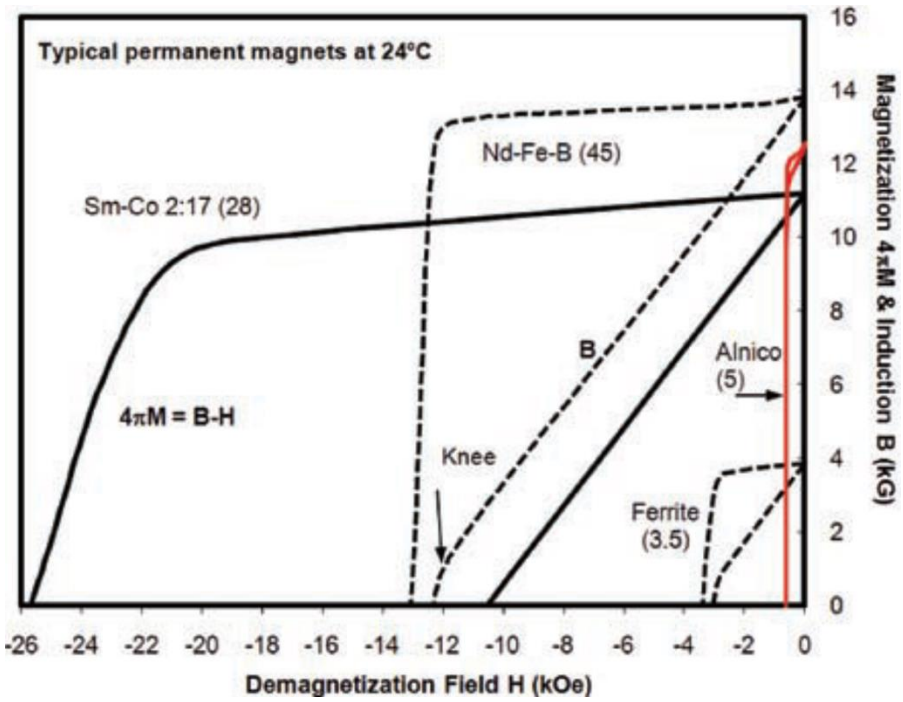

Figure 1.3.1 M-H curves of typical permanent magnets including Sm-Co, Nd-Fe-B, AlNiCo, and ferrites.[3]

Table 1.3.1 Structure type, and magnetic properties which include M_s, H_c, K_1, T_c for standard permanent magnets.[9,10,11]

	Structure Type[a]	**Curie Temperature[10] (K)**	**Magnetic Saturation[9] (emu g^{-1})**	**Magnetocrystalline Anisotropy Constant[9] (MJ m^{-3})**
$Nd_2Fe_{14}B$	**Tetragonal**	**585**	**171**	**4.9**
$SmCo_5$	**Hexagonal**	**993**	**110**	**17.2**
AlNiCo 5	**Cubic**	**1210**	**153**	**0.68**
$SrFe_{12}O_{19}$	**Hexagonal**	**740**	**71**	**0.35**

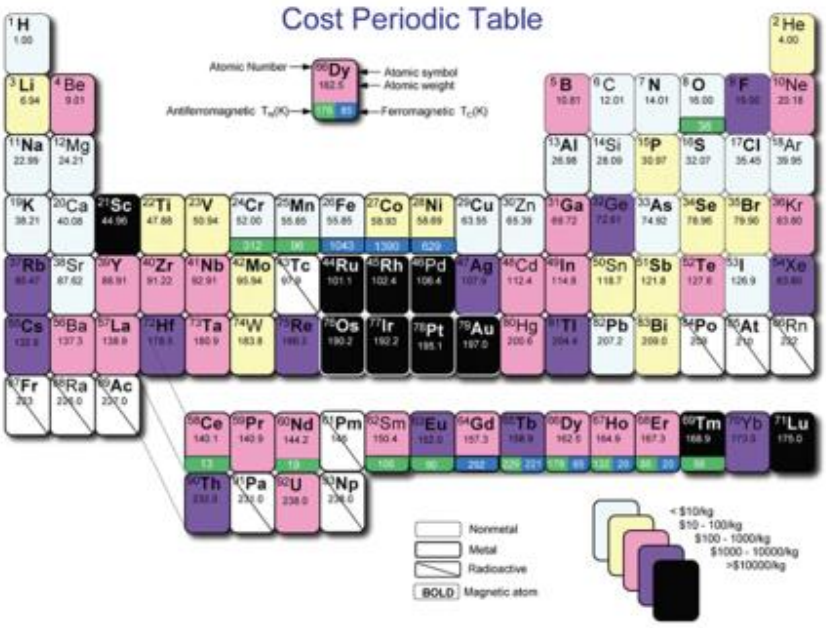

Figure 1.3.2. Periodic table color coated for prices of elements from very cheap, cheap, moderately inexpensive, expensive, and very expensive. The magnetic elements are illustrated in bold.[10]

1.3.1 AlNiCo

AlNiCo magnets were first discovered by Oliver and Shedden in 1938.[12] Unlike other permanent magnets developed later on AlNiCo magnets are made of a binary phase of Fe/FeCo rich phase within a Ni-Al matrix. Normal synthesis methods include slow cooling from a single bcc phase formed at 1250 °C to form two bcc phases of Fe/FeCo and Ni-Al ferromagnetic phase upon cooling. The material is tempered at 650 °C for 4 hr to form elongated FeCo/Fe where the high coercivity is attributed to shape anisotropy of interconnected single domain particles. Isotropic magnets are normally formed with Co percentages of 0-20% wt and are known as AlNiCo 1-4. While anisotropic AlNiCo magnets are formed with Co and Ti additive percentages of 22-40% wt and 5-8.5% wt (known as AlNiCo 5), and are normally formed within an external field. Despite interest early on, these

magnets, due to the low magnetocrystalline anisotropy energy observed in Table 1.3.1 from its biaxial bcc structure AlNiCo magnets, have been replaced by other permanent magnets, however the use of shape anisotropy to increase the energy product of materials is a practice used in developing new hard magnetic materials in the present day.[13]

1.3.2 Hexaferrites

Barium and strontium ferrite were discovered in 1951 and 1963 by Went et al. and Cochardt et al. Like most permanent magnets hexagonal ferrites have a uniaxial hexagonal structure, with an easy axis parallel to the hexagonal c-axis.[14,15] However it is a ferrimagnetic material with two sublattices oriented in opposite directions which hinders its M_s and M_r. The classic route for synthesizing hexagonal ferrite includes mixing fine powders of $BaCO_3$ or $SrCO_3$ and α-Fe_2O_3, followed by annealing at temperatures ranging from 700 °C -1200 °C in an oxidizing atmosphere. There have been new developments in the synthesis of hexagonal ferrites where the material can be formed from hydrothermal synthesis at temperatures ranging from 180 °C to 250 °C.[16] Single crystalline plate structures with its easy axis perpendicular to the longitudinal axis have magnetocrystalline anisotropy which makes it easy to saturate the magnetization when aligned upon the easy axis. However, the hard axis perpendicular to the easy axis is also favorable due to shape anisotropy which assists in field reversal. The structure tends to lead to an inverse relationship with coercivity and magnetic remanence dependent on the long and short axis of the plate structures. Despite the drawbacks for hexagonal ferrites there low cost and easy synthesis methods make it attractive for industrial uses in loudspeakers, blower motors, and windscreen wiper motors.[17]

1.3.3 Samarium Cobalt

Samarium cobalt was first recognized by Hubbard et al. in 1960 and further developed by Hoffer and Strnat in 1966.[18,19] It has the highest magnetocrystalline anisotropy out of all the general permanent magnets due to its uniaxial hexagonal crystal structure which results in a high coercivity as well as a high magnetic saturation due to the ferromagnetic alignment of cobalt ions. During sintering to form $SmCo_5$ a samarium rich phase (Sm_2Co_7) is the starting material followed by compacting within a magnetic field and sintering at elevated temperatures (approximately 1150 °C) in helium, argon, or hydrogen. Sm-Co complexes can be described as non-equilibrium multiphase metallurgical system, therefore a phase diagram is useful in order to avoid eutectoid decomposition into Sm_2Co_7 or Sm_2Co_{17} which would lead to easier field reversal. Unfortunately this method normally results in low coercivity due to large grain size, (15% of theoretical max), therefore ball milling has been used to decrease particle size thus increasing coercivity.[17] Despite its great magnetic properties and stability at high temperatures, due to the price of samarium and cobalt, the hexagonal ferrites and neodymium magnets are normally used minus applications which need high coercivities at temperatures greater than 200 °C.[3]

1.3.4 Neodymium Magnets

Nd-Fe-B magnets are the most recent major development in permanent magnets discovered in 1984 by Sagawa and Croat et al. by sintering magnets followed by quenching.[20,21] The search for these magnets began due to the high price of the samarium cobalt magnets which attracted attention to iron rich permanent magnets. Nd-Fe-B magnets have a uniaxial tetragonal crystal structure with a high magnetocrystalline anisotropy constant observed in

Table 1.3.1, which resulted in extremely high energy product values (4.9 MJ m^{-3}).[9] Its light weight allows for more compact electronic devices which revolutionized the car industry with hybrid cars as well as the increase in processing speeds in hand held devices. Unfortunately, neodymium magnets have a low Curie temperature and thermal stability (175 °C), therefore they are doped with dysprosium which is ten times more expensive than neodymium. Doping also causes a decrease in magnetization values due to antiparallel coupling with iron. Developments have been made to further enhance the properties of Nd-Fe-B, such as decreasing size of grains, decoupling of grain boundaries with Nd-Cu, and decreasing size of nonmagnetic phase.[22,23]

1.4 Alternative Permanent Magnets

1.4.1 Mn-Al

Mn-Al were one of the permanent magnets discovered early on with potential properties to compete with the classic permanent magnets. Kamino et al. determined $Mn_{55}Al_{45}$ should have a theoretical max magnetocrystalline anisotropy of 10^5 J m^{-3} with a H_c 31 kOe even though experimental values of $1/5^{th}$ the coercivity have been developed.[24] They have a face centered tetragonal crystal structure which is formed by cooling from a disordered hcp phase which goes through an orthorhombic intermediate phase. It was found that an addition of 1% wt C is enough to enhance its thermal stability as well as increase its coercivity and magnetic remanence. The atomic composition of Mn-Al-C magnets are less expensive then AlNiCo magnets with comparable properties minus lower thermal stability and a Curie temperature of 575 K. However, unlike other materials they can be easily mass produced, and they are highly corrosive resistance.[17] Moreover, Mn_2Ga has also been explored where reports show this alloy to have a superior magnetocrystalline anisotropy constant of 2.35 MJ m^{-3}, however

the price of gallium is much greater than aluminum. Both alloys suffer from low M_s values due to antiferromagnetic coupling of manganese.[10]

1.4.2 Mn-Bi

MnBi has a uniaxial NiAs hcp structure with a large positive temperature coefficient from 150-500 K which makes it a great candidate for high temperature applications with a magnetocrystalline anisotropy constant of 10^6 J m^{-3}. Its magnetic properties in bulk material and films have been drastically studied but due to manganese segregation which takes place it's hard to synthesize this material in bulk. Different synthesis methods have been developed in forming MnBi over the past decade which include arc melting, rapid solidification, mechanical alloying, and sintering.[2] Yang recently reported synthesizing a 90% wt MnBi ribbons by sintering which resulted in a $(BH)_{max}$ of 56 and 32 kJ m^{-3} at room temperature and 400 K with H_c up to 11 kOe by mechanical milling over 7 hrs.[25] Figure 1.4.2.1 shows room temperature and 400 K hysteresis loops with an increase in coercivity due to the positive temperature coefficient for MnBi. With this materials large positive temperature coefficient and high coercivity values in comparison to the hexagonal ferrites it can definitely compete with hexagonal ferrites if better bulk synthesis methods can be established.

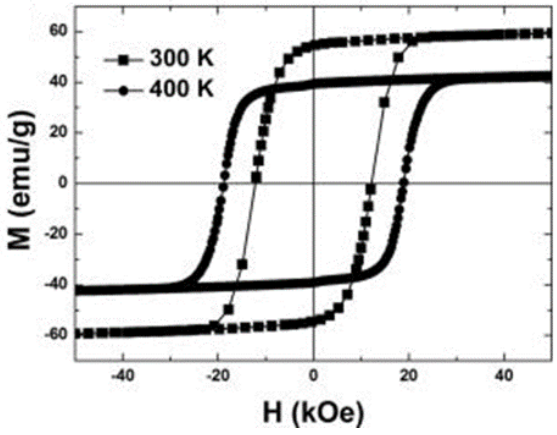

Figure 1.4.2.1 M-H curves of MnBi alloy showing an enhanced Hc due to the positive temperature coefficient from 300 K to 400 K.[25]

1.4.3 Cobalt Carbide

Cobalt carbide previously has been studied for its physical and catalytic properties. Within the last decade this material has been getting attention for its hard magnetic properties. Cobalt carbide has an orthorhombic crystal structure with two known phases of Co_3C and Co_2C. The observation of high Hc values in cobalt carbide were first observed by Chinnasamy et al. within a polyol synthesis with the goal of forming SmCo. Since that time authors of this publication have determined the crystal phase to be majority cobalt carbide.[26] Harris et. al reported enhanced magnetic properties by tuning the ratio between the Co_2C and Co_3C phases which are believed to have spring exchange interaction (Figure 1.4.3.1a).[27,28]. The report also indicated cobalt carbide to have comparable room temperature magnetic properties with hexagonal ferrites a max energy product of 20 kJ m^{-3} with H_c of 3.4 kOe (Figure 1.4.3.1b).[27] With the positive developments in cobalt carbide come drawbacks with low Curie temperature of 510 K, an irreversible transformation to fcc Co as temperatures approach 700 K, as well low M_s values due to nonmagnetic carbon within the lattice structure.[27] Also bulk production of cobalt carbide with better control over the carbides size, shape and phase need to be developed.

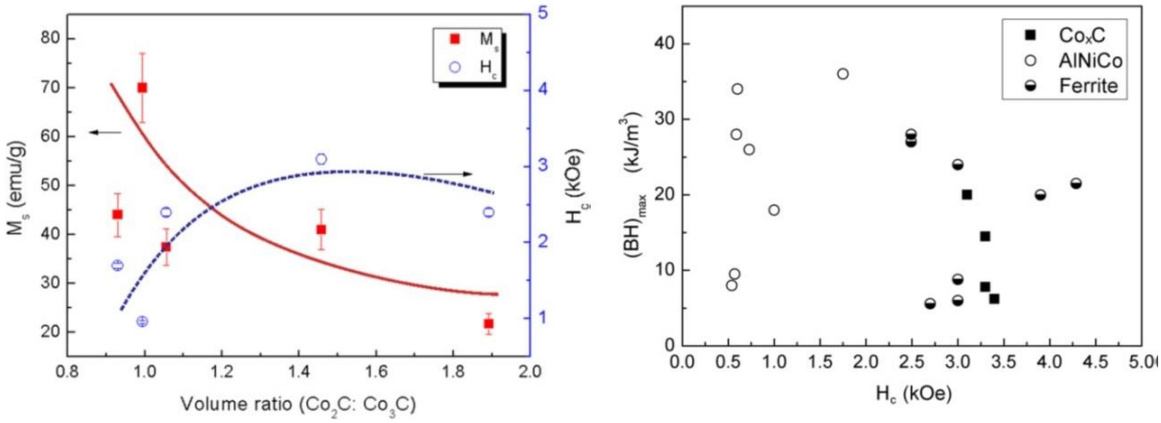

Figure 1.4.3.1 (a) Ms and H_c with change in Co_2C:Co_3C volume ratio. (b) $(BH)_{max}$ versus coercivity for AlNiCo, strontium ferrite, and cobalt carbide. [27]

1.4.4 α-$Fe_{16}N_2$

Iron nitride has many different phases including Fe_3N, Fe_4N, and a recently reported Fe_7N_3 phase, however none have had as much potential as the α-$Fe_{16}N_2$ phase.[29] The base centered tetragonal structure of the α-$Fe_{16}N_2$ was discovered in 1951 by Jack but its magnetic properties did not get much attention until Kim and Takahashi's work in 1972 obtained by evaporation of Fe on glass with low-pressure nitrogen.[30,31] Most reports on synthesis methods consist of hydrogen reduction and nitrogenation of iron or iron oxide. Previous studies have reported H_c values of 3.3 kOe with Ms values of 108 emu g^{-1} with a magnetocrystalline anisotropy constant of 4.4 x 10^5 J m^{-3}.[32] Recent reports on $Fe_{16}N_2$ nanoparticles by Derba et al. have H_c values of 2.2kOe and an extraordinarily high M_s value of 215 emu g^{-1} with a far superior magnetic saturation value to any rare-earth magnet due to the high percentage of Fe within the lattice structure.[33] The main concern with $Fe_{16}N_2$ is its instability at low temperatures where it has decomposed into α-Fe and γ Fe_4N.[34] Therefore, if its thermal stability could be improved as well as improved bulk single phase synthesis methods, iron nitride may be able to compete with some of today's popular permanent magnets.

1.4.5 Co-Pt

Cobalt platinum was discovered by Jellinghaus in 1936 and further investigated in 1950 by Newkirk et al.[35] The material has a disordered fcc structure which is converted to ordered uniaxial face centered tetragonal (fct) phase at elevated temperatures. Coercivity up to 6.6 kOe and energy products up to 100 kJ m^{-3} have been reported.[36] Due to their resistance to

corrosion they may be used in applications such as hearing aids, motors for watches, and metering devices where the magnet may be in direct contact with the corrosive liquid. Despite the advantageous qualities, the high cost of platinum does not make this alloy an attractive magnet for multiple applications.[17]

1.4.6 Fe-Pt

Likewise FePt has been researched extensively in the past decade. It is one of the few materials that has been published with tunable shape and size of nanomaterials for permanent magnet applications. Similar to Co-Pt, it needs to go through a disordered hexagonal (fcc) to ordered face-centered tetragonal (fct) transition to get magnetically hard material. The transition takes place at temperatures greater than 600 °C which normally leads to sintering of nanoparticles which will affect its magnetic properties.[2] Fe-Pt nanoparticles annealed in a salt matrix to prevent aggregation resulted in uniform 8 nm nanoparticles with an H_c of 30 kOe.[37] If the cost of Pt was drastically less expensive the FePt alloy could potentially dominate the market for permanent magnets.

1.4.7 Iron Carbide

Iron carbide is a ferromagnetic material with multiple phases including hexagonal Fe_2C, Fe_7C_3, monoclinic Fe_5C_2, and orthorhombic Fe_3C.[38,39] They have been mostly analyzed for their catalytic properties for Fischer Tropsch, however several studies exist for magnetic applications such as, T-2 contrast agents, and magnetic memory.[40,41,42] Unlike cobalt carbide it has a significantly high magnetic saturation value of 140 emu g^{-1} for bulk material. However, its theoretical max for coercivity is only 1150 Oe and the highest reported H_c is

only 700 Oe at room temperature.[10,43] Also, due to the metastable formation of certain structures such as the hexagonal Fe_2C, and Fe_7C_3 it is difficult get an understanding on how crystal structure may affect magnetic properties.[41] Despite these drawbacks, if iron carbide could be further investigated for its hard magnetic properties it would have advantages of high stability, high remanence, as well as very low cost.

1.5 Nucleation and Growth

Nanomaterials contain magnetic, catalytic, and optical properties which diverge from their corresponding bulk material. The first schematic of nanoparticle formation was made from Victor Kuhn LaMer in 1950.[44] He believed in order to get monodispersed size distribution in a sample, separate states of nucleation and growth must exist. LaMer's model represented in Figure 1.5.1 shows that particle growth is broken into three steps.

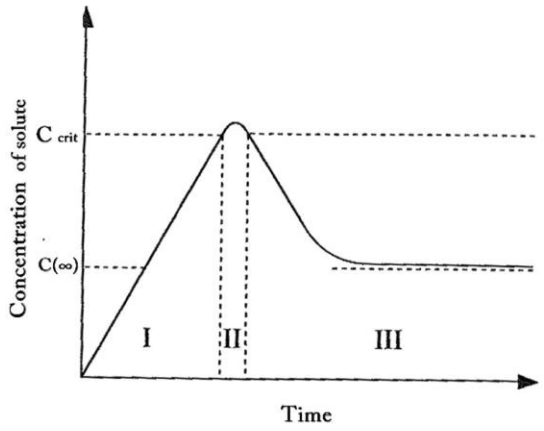

Figure 1.5.1 LaMer diagram schematic.[45]

In the initial step, free monomers are formed in solution. During the second step the monomers reach a critical concentration where burst nucleation of monomer species form. Following the nucleation process, growth occurs where the monomers diffuse through solution to form clusters and nanoparticles while monomer concentration decreases. During the growth

process small crystals with higher surface energy are consumed by larger crystals, a process known as Ostwald ripening.[45-46]

Along with LaMer's schematic for nucleation and growth, Friedrich Wilhelm Ostwald in 1897 published his work which led to the Ostwald rule of stages.[47] This study took into account that within a synthesis intermediates are formed before forming the final product. The intermediates are not the most thermodynamically stable, however they tend to have a structure and Gibbs free energy closer to the original state, therefore the metastable state nucleates more readily.

Ostwald's rule of stages has brought up many speculations. Previous reports have suggested the free energy and enthalpy of formation values are close for certain polymorphs and small changes in thermodynamics such as surface area may invert the order of thermodynamic stability.[48] Therefore, decrease metastability with increase in surface energy may be a common occurrence in nanomaterials. Ostwald's step rule also shows it is favorable for intermediate phases to form due to smaller free energy transitions to reach the final phase.

Another exception to the rule is the observation that nucleation and growth do not only occur through atoms and molecules but nanometric building blocks, therefore more than one growth step may occur in a series.[49]

1.6 Synthesis Methods

1.6.1 Thermal Decomposition of Precursor

There have been massive developments in wet chemical synthesis methods within the past century. There bottom-up synthesis approach allows for greater control of particle size, and shape, without the use of expensive equipment in comparison to physical synthesis methods. Methods for wet synthesis include co-precipitation, microemulsion, solvothermal, polyol, and thermal

decomposition. Co-precipitation and microemulsions take advantage of inexpensive synthesis near ambient temperatures however, they normally form nanoparticles with a broad size distribution due to collective nucleation and growth steps with low crystallinity. Solvothermal synthesis are done under pressure in a sealed container which is one of the most successful synthesis methods for forming a wide range of materials, but due to the use of volatile solvents at high pressures size control is difficult to achieve.[50] Thermal decomposition method is a simple and quick method for synthesizing nanoparticles which utilizes thermal decomposition of a metal precursor with a surfactant as a capping agent. This method utilizing long chained organic molecules which include but not limited to fatty acids, aliphatic amines, a long chained carboxylic acids. This method was first used for synthesis of ferrite nanoparticles by Alivisatos and coworkers which used a non-hydrolytic system with iron Cupferron complexes to synthesize 4-10 nm γ-Fe_2O_3 with non-hydroxylated surfaces.[51] Since then thermal decomposition has become the most reliable system for making monodispersed particles with nanoparticle size ranging from 2-30 nm. The increase in temperatures needed to for thermal decomposition in comparison to co-precipitation and microemulsions allows for separation of nucleation and growth steps for monodispersed nanoparticles as well as greater crystallinity needed for most applications.[44, 52]

1.6.2 Magnetic nanoparticles synthesis with thermal decomposition

As discussed previously in section 1.2 magnetic properties are greatly affected by particle size, consequently by controlling a particles dimensions the same material can be fine-tuned for a wide range of applications. Iron oxide has been studied extensively for potential applications in magnetic recording media, ferrofluids, and contrast agents.[53] Park used various solvents with different boiling points to tailor particle size.[54] Increasing the boiling point of the solvent from

lowest (hexadecane b.p 274 °C) to highest boiling point (trioctylamine b.p 365 °C) showed an increase in particle size ranging from 5-22 nm with a <4.1% size variation. Figure 1.6.2.1a shows TEM of the different nanoparticles while Figure 1.6.2.1b shows how an increase in particle size increases the blocking temperature from the zero field cooled curves. Time has also shown to increase particle size while decreasing size distribution which agrees with digestive ripening where smaller nuclei dissolve to form larger particles. [55] Other sources have manipulated particle size by controlling rate of nucleation and growth through oleic acid concentration where higher concentrations slows down the nucleation process leading to more nuclei and larger particles. Using oleic acid and a seed mediated growth synthesis control of particle growth with 1 nm intervals was possible ranging from 6-13 nm.[56] Mixtures of 1:1, 1:2, and 1:3 ratios of $Fe(CO)_5$ and oleic acid were used to make 4, 8, and 11 nm nanoparticles, and for the seed mediated growth to form larger particles.

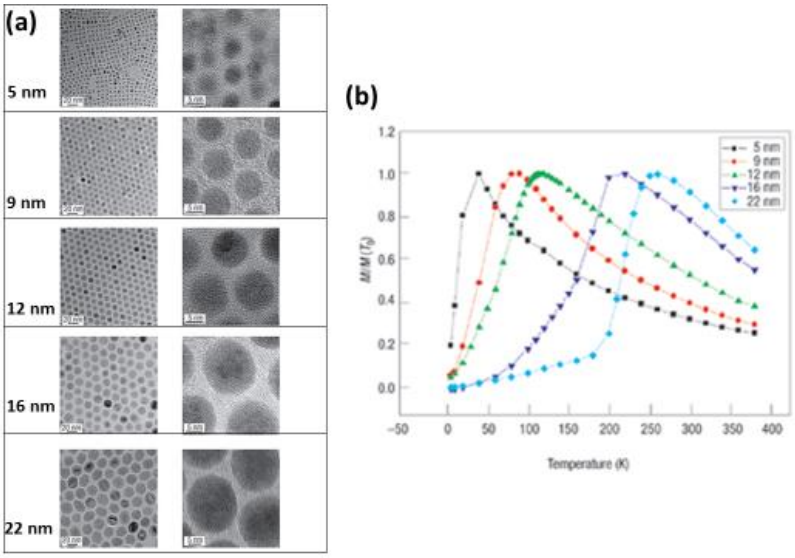

Figure 1.6.2.1 (a) Park et al's synthesis of iron oxide utilizing different bp solvents to get nanoparticles with 5 nm, 9 nm, 12 nm, 16nm, and 22 nm. (b) Zero field cool curve for 5 nm, 9 nm, 12 nm, 16 nm, and 22 nm nanoparticles within a 100 Oe field.[54]

Shape control of ferrite nanoparticles has attracted much attention do to applications in magnetic sensing and catalyst.[57] The shape changes exposed crystal facets and atomic arrangement of nanoparticles thus affecting its properties.[58] Change in shape also changes the surface anisotropy term K_{eff} which can cause shifts in blocking temperature (T_B).[59] Various ways can be utilized to control particle shape but surfactants are the most common method.

Bao and coworkers have used trioctylphosphine oxide to control growth of iron oxide nanoworms.[60] The iron oxide nanoworms were synthesized from thermal decomposition of iron oleate in 13 mL 1-octadecene and 1 mL oleic acid, followed by hot addition of TOPO at 290 °C. [61] A time study showed the nanoparticles went from 12 nm spherical particles to growing in length, longer than 200 nm overtime. The proposed mechanism is that the weakly bound surfactant TOPO concentration mediates aggregation of nanoparticles. M-H curves observed in Figure 1.6.2.2 show superparamagnetic and ferromagnetic curves for the particle and nanoworm morphology.

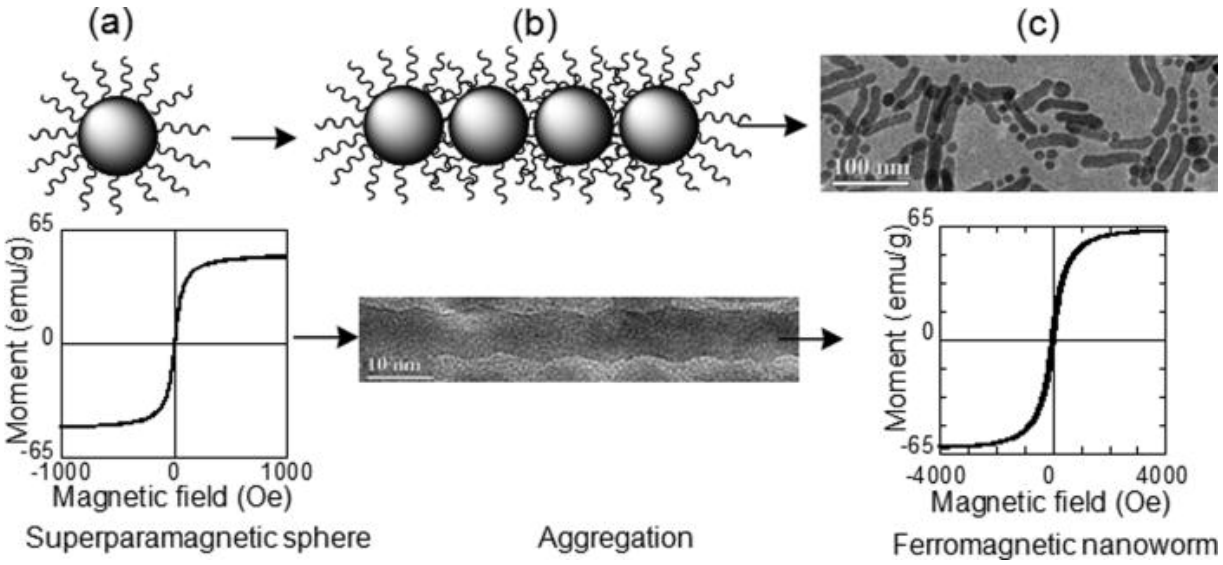

Figure 1.6.2.2 (a) Illustration and M-H curve of superparamagnetic iron oxide. (b) Illustration and TEM image of aggregation of nanoparticles. (c) TEM image and M-H curve of ferromagnetic nanoworms.[61]

Wanyin Ge did an in-depth study on how cationic surfactant cetylpyridinium chloride (CPC) with $Fe(acac)_3$ as the precursor in benzyl ether affected the shape of the material.[62] Similar to previous work faceted Fe_3O_4 were formed. However with change in CPC concentration from 0.028 mmol to 2 mmol five different shapes consisting of cubic, truncated cubic, cuboctahedral, truncated, octahedral, and octahedral nanostructures were formed (Figure 1.6.2.3). Comparing CPC to other quaternary cationic amines from cetylpyridinium bromide (CPB), cetylammonium chloride (CTAC), cetylammonium bromide (CTAB), NH_4Cl, and pyridinium chloride (PC), the author came to three factors for which CPC assists in tuning particle shape. These three factors include the selective adsorption of Cl^- on (111) planes, the synergistic effect of pyridinium, as well as dense packing of long carbon chains for on the (111) planes. Figure 1.6.2.3 on the right represents the change in magnetic properties with different polyhedral morphologies of Fe_3O_4.

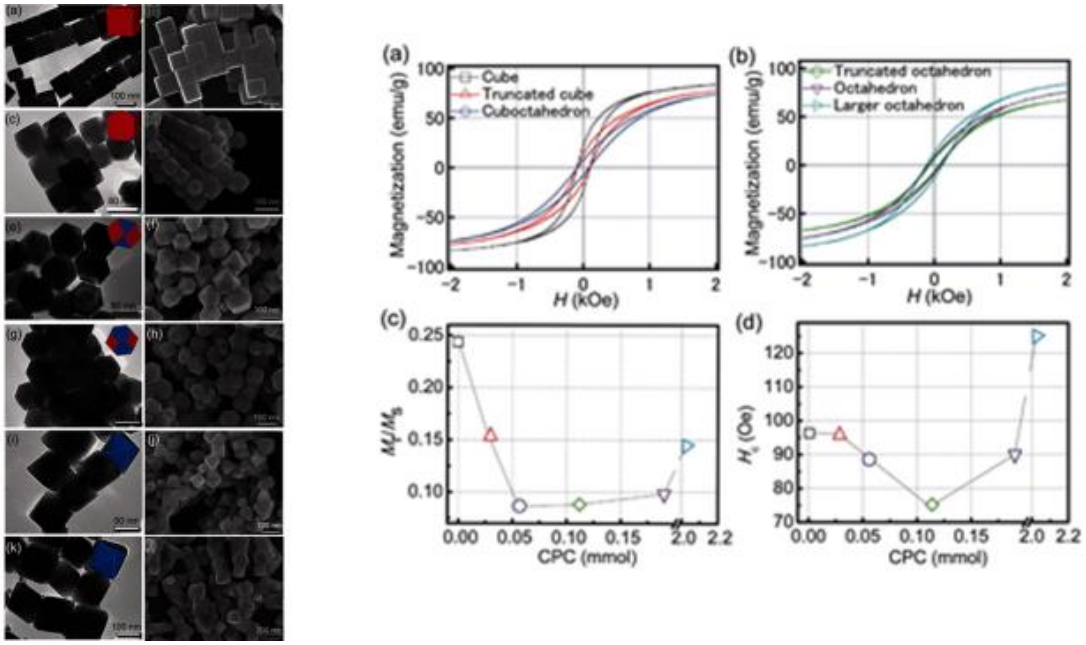

Figure 1.6.2.3 (left) (a,b) cubic, (c,d) truncated cubic, (e,f) cuboctahedral, (g,h) truncated, octahedral, and (i,j) octahedral transmission electron microscopy micrographs. (right) (a) M-H curves for cubic, truncated cubic, cuboctahedral structures. (b) M-H curves for cuboctahedral, truncated, octahedral, and octahedral structures. [62]

1.6.3 Amine Reduction of Nanoparticles

In addition to using oleylamine and other aliphatic amines as a medium for thermal decomposition of a metal salt, reduction of the metal precursor to zero valent nanoparticles may occur. There have been many studies of reduction of noble and 3d metal nanoparticles such as silver, gold, platinum, nickel, iron, and 3d metal-platinum nanoparticles with an even size distribution throughout the sample.[63,64,65,66,67,68] However the specific mechanism for reduction is still in question. Silver nanoparticles reduced by oleylamine used FT-IR to detected the presence of C≡N at 2175 and 2149 cm^{-1} while =N-H, C=N stretching bands, and =N-H deformation bands were present at 3330, 1660, and 1580 cm^{-1} on the surface of the nanoparticles.[63] A proposed mechanism is shown in Figure 1.6.3.1 where the amine forms a complex with the salt followed by electron transfer to silver (I) species to form amino radicals. With continued time the radicals turn into imines or imines to nitriles which stabilize the silver (0) surface. In another report iron (II) species

were reduced to iron (0) nanoparticles at 150 °C with the assistance of acidic hexadecylammonium chloride.[69] FT-IR showed formation of imine species without the presence of nitriles which shows the reaction occurs rapidly without time to further oxidize the nitrile. Even though there have been studies on reduction of nanoparticles with aliphatic amines more complicated mechanisms such as wet synthesis formation of carbides, nitrides, and sulfides, are still under investigation.

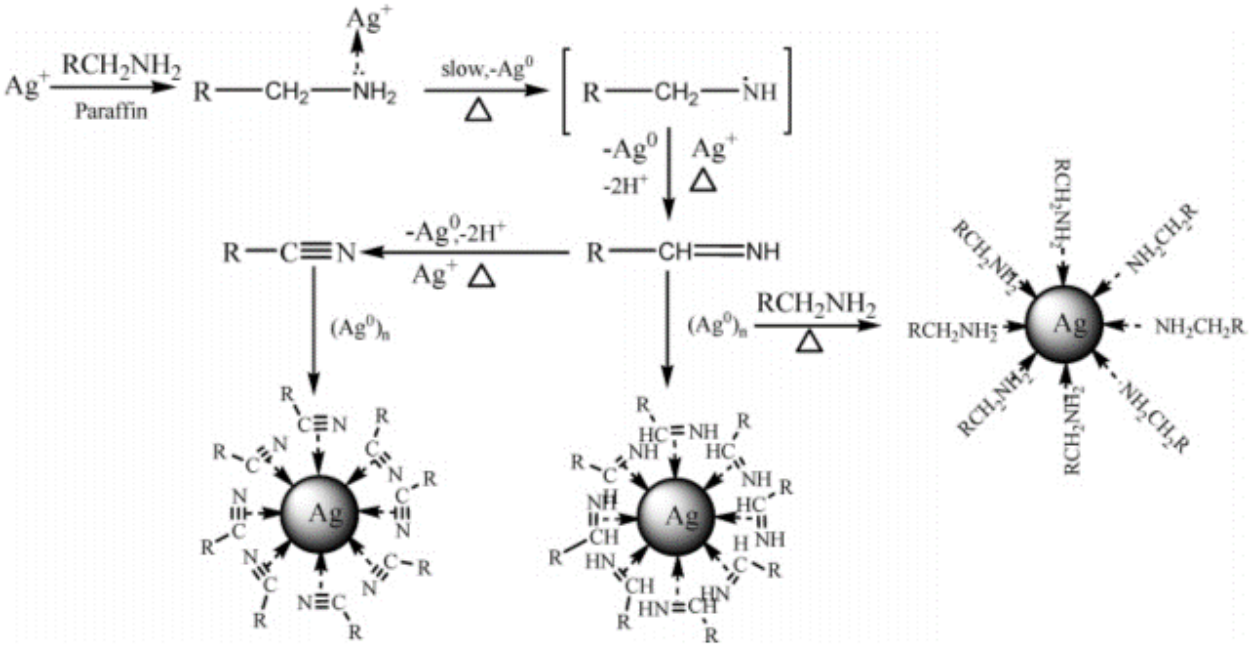

Figure 1.6.3.1 Mechanism of silver reduction/oleylamine dehydrogenation which results in silver (0) nanoparticles stabilized by amine, imine, or cyano group.[63]

1.7 Summary of Objectives

The goal of this work is the enhancement of the hard magnetic properties of iron carbide for potential applications as a permanent magnet. Previous developments have enhanced the properties of cobalt carbide through tuning size, shape, and crystal phase while there has been limited work on the iron carbide system. Iron carbide is also composed primarily of iron, the most abundant and inexpensive 3d metal, therefore a permanent magnet made from iron and carbon

could drastically improve the cost of permanent magnet materials. Objectives for this work include:

- Development of a wet synthesis method for synthesizing pure phase iron carbide (FexC).
- Tailor magnetic properties through control of particle size, shape, and crystal phase.
- Further investigation of magnetically soft Fe_7C_3 hexagonal plates with, shape induced magnetic properties.
- Utilize exchange bias interaction to enhance the Hc of the semi-hard Fe_3C synthesis developed previously, as well as investigate the bias in the ferro-aniferromagnetic coupled system.
- Utilize the ferromagnetically soft Fe_7C_3 synthesis to synthesize a $Fe_7C_3/SrFe_{12}O_{19}$ exchange spring magnet through partial reduction of strontium ferrite.

Chapter 2. Instrumentation

2.0 Introduction

Chapter 2 will cover the instrumentation needed to characterize the specimens made within this work. Composition of the nanomaterials was done with x-ray diffraction which can detect the different crystal structures of iron carbide as well as metal oxides. Scanning electron microscope and transmission electron microscope were used to observe the physical dimensions of the synthesized material. Energy dispersive spectroscopy was used to get elemental information of the materials while, x-ray photoelectron spectroscopy, and Raman spectroscopy gave surface composition information. The vibrating sample magnetometer was utilized to determine the magnetic properties of each material while thermal gravimetric analysis was used to determine thermal stability. Fourier transform infrared spectroscopy was used for the soul purpose of determining composition of the solvent throughout the reaction.

2.1 X-ray Diffraction

X-ray diffraction (XRD) is a tool that utilizes an x-ray source to detect the 3-D crystal pattern by measuring a crystalline specimen at different angles. Max von Laue founded XRD in 1912, which lead to his Nobel Prize win in physics in 1914. This technique is useful for identification of an unknown compound based on its diffraction pattern. An x-ray source is used in this instance instead of visible light because it is on the same magnitude as the distance between two crystal planes. The x-rays are formed from high-speed electron bombardment of a metal target between a hot cathode, and an anode composed of either copper, aluminum, molybdenum, or magnesium. The x-ray beam of a known wavelength interacts with a sample at different angles and scatters

elastically in different directions. The scattered waves mostly cancel each other out from destructive interference. In order for a plane to be detected, Bragg's law must be fulfilled where constructive interference is said to be at its strongest. Equation 1 displays Bragg's equation where *d* is the interplanar distance, λ is the wavelength of the incident x-ray, *n* is an integer, and Θ is the incident angle.

$$n\lambda = 2d \sin\theta \tag{1}$$

The equation expresses when an x-ray is scattered constructively they remain in phase since the difference in path lengths (right side of equation) is equivalent to a multiple of the wavelength (left side of equation). The constructive interference is intensified on the diffraction pattern due to consecutive constructive interference from a repeating crystal plane within the lattice structure represented in Figure 2.1.1 As well as composition this technique can be used to determine the orientation of a single crystal, calculate bond lengths, and measure size, shape, and internal stress of a crystal structure.

Crystallite size can be determined from the area under a peak in a diffraction pattern using the Scherrer equation shown in eq 1. Where τ is the crystallite size, *K* is the shape factor, β is the full with half max (FWHM), and Θ is the Bragg angle. As the equation entails with increase peak broadening the crystallite size decreases. This is due to an increase ratio of destructive interference to constructive interference from less consecutive repeating crystal planes in smaller particles. Scherrer values give an equal or lower estimate on particle size. Due to the presence of lattice strain and defects the crystallite size determined by x-ray diffraction may not be accurate, however it can be used as a screening technique to compare samples and equated with dimensions observed from electron microscopy techniques.[70]

$$\tau = \frac{K\lambda}{\beta \cos\theta} \tag{2}$$

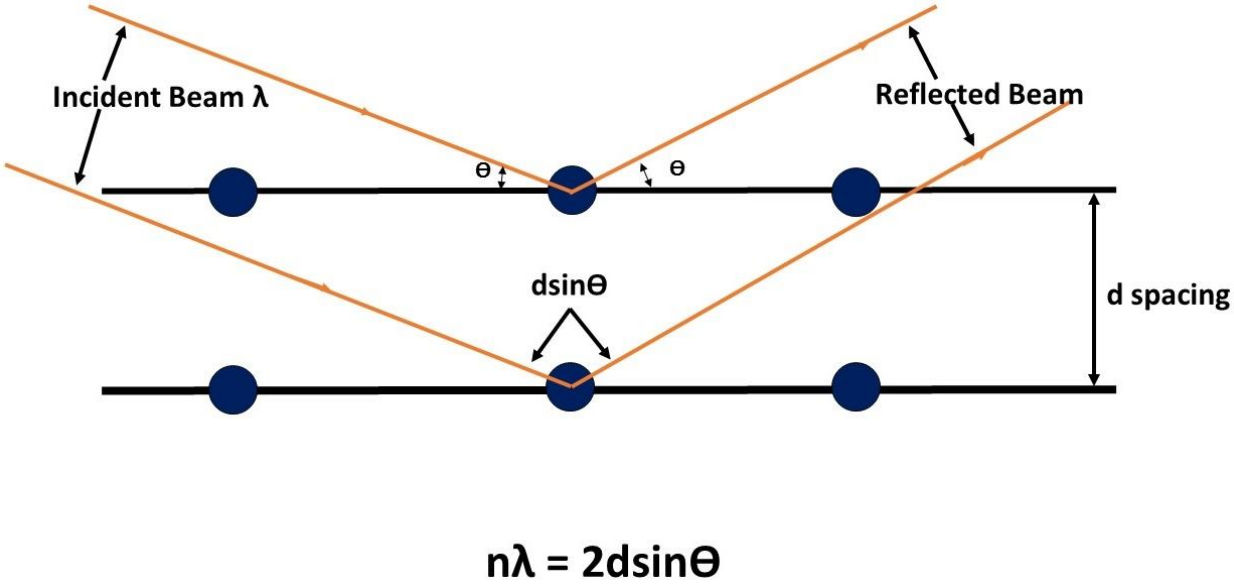

Figure 2.1.1 Schematic of Bragg's law where an incident x-ray is diffracted at angle Θ with a wavelength equivalent to a multiple of the incident wavelength.

2.1.2 Peak Determination

Most x-ray diffraction software comes with a library which can be used to identify an unknown compound. The main issue with a library reference patterns is the inability to take into account shifts in peaks, and differentiate between overlapping peaks in multiphase systems. The main characterization technique for x-ray diffraction used in this work was Rietveld refinement. This technique uses the space group, lattice parameters, and atomic position to simulate a pattern of the crystal structure, followed by use of the least squares method to fit a diffraction pattern. Reitveld refinement works well in comparison to other XRD characterization techniques due to the fact the

crystal phase parameters will change to better fit experimental data. It works well in multi-phase systems were there is overlap between peak intensities and can be used to get phase composition and lattice parameters of a sample. In this work the Reitveld refinement capability in X'Pert Highscore Plus was used to simulate a model from crystal parameters and better fit the data through the least squares method.[71]

2.2 Transmission Electron Microscopy

Transmission electron microscopy (TEM) is a form of electron microscopy where an image is formed from transmission of electrons through a specimen. TEM contains a similar conformation to transmission light microscopes which both contain a light source, condenser lens, specimen stage, objective lens, and projector lens. The main difference between the two techniques is that TEM uses electrons in place of visible light which can give resolution as low as 0.1 nm and needs to be under vacuum to prohibit electron collision with particles within the air.

There are 2 types of electron guns used for TEM which include thermionic and field emission guns. The thermionic guns heat the filament comprised of tungsten or lanthanum hexaboride to a temperature high enough for the electrons to overcome the surface energy barrier to eject electrons. The field emission uses a high applied field to overcome this surface potential barrier. Glass lenses cannot be used to focus the electron beam, therefore electromagnetic lenses are used in this instance. There are 3 types of lenses for TEM which include a condenser lens which controls the beam diameter and convergence angle on the specimen. In some cases, there is also an intermediate lens used to switch between regular imaging and diffraction mode. While the objective lens is located below the specimen stage and is used to focus the beam once it transmits through the sample and the projector lens focuses the image onto a phosphorescent screen. The

sample holders are normally made from a 3 mm disk of copper coated with an amorphous carbon mesh to hold the specimen. Figure 2.2.1a shows the basic instrumental components of TEM.

As previously mentioned there is a diffraction mode besides basic imaging on TEM. The theory behind diffraction is similar to x-ray diffraction where Bragg's law must be met. When the electron beam is parallel to the crystallographic axis, diffraction points which represent crystal planes will form a pattern analogous to the crystal structure. Using the d-spacing and the angles between planes it is possible to determine the crystal phase of a material.[72]

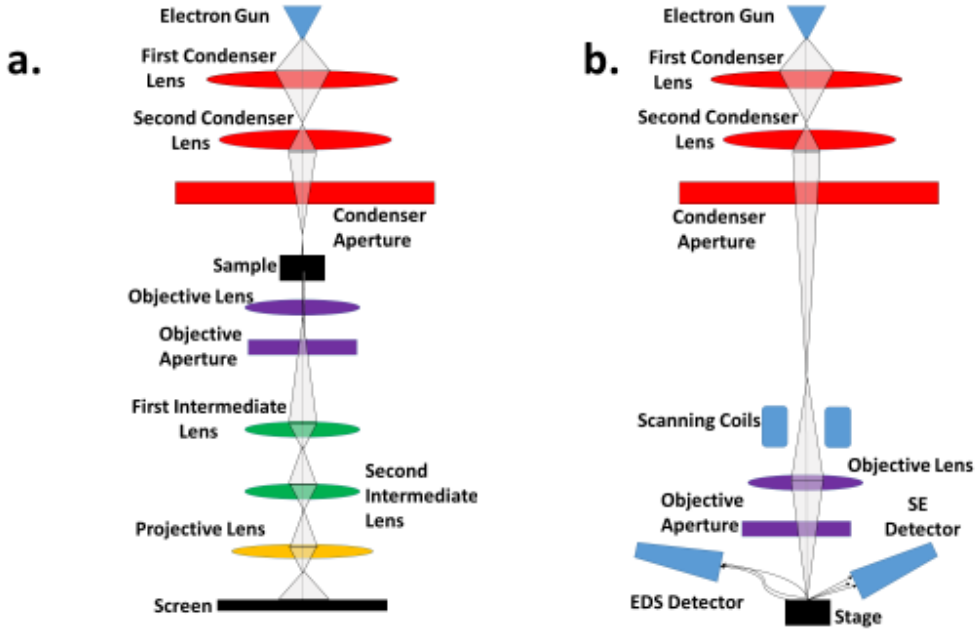

Figure 2.2.1 Basic instrumental components of (a) TEM and (b) SEM.

2.3 Scanning Electron Microscopy

Scanning electron microscopy (SEM) is a form of electron microscopy which is similar to scanning confocal microscopes except it uses a focus electron beam. Unlike transmission electron microscopy (TEM), SEM scans the surface of a sample with a probe while TEM illuminates the sample area. It is best utilized to get images with three dimensional appearance, and it can also obtain chemical information through energy dispersive x-ray spectroscopy (EDS), and back scattering (BS) detection.

The source of the electrons which bombard the sample is an electron gun which is either thermionic or field emission. The electrons go through objective and condenser electromagnetic lenses where the condenser reduces cross section of beam, and objective beam further focuses beam to a diameter on the nanoscale. The probe scans a rectangular area where electrons are captured by Faradays cage, which attracts the secondary electrons from scanning points on the specimen needed to form the reconstructed image presented on a cathode ray tube or crystal display. Figure 2.2.1b shows an example of a basic set up for a SEM.[73]

2.4 Energy Dispersive X-ray Spectroscopy

EDS was first commercialized at the beginning of the 1970's. This technique is utilized to determine the elemental composition of a sample. When a high energy electron beam bombards the sample, an electron is ejected from the inner shell of an atom which forms a hole. The hole is filled by an electron in the outer shell which results in an emission of an x-ray with a particular energy dependent on the atomic number for which the x-ray was derived. Figure 2.4.1a shows a schematic for the emission of an x-ray for EDS. It is a relatively fast characterization technique

since it can collect x-ray energies from a range of elements simultaneously. An energy range from 0.1 to 20 eV with both light and heavy elements can be observed on a spectra. The detector can pick up x-rays coming from multiple shells including K, M, and L. The spectra gives an energy in eV where the energy of the emitted x-ray is dependent on the element, which orbital the hole was formed and the orbital which filled the hole. The detection depth within the sample is dependent on the accelerating voltage of the electrons as well as the specimen density. EDS software tends to have the capability of forming elemental maps, elemental detection at a single point, specified area, or a line scan which detects the change in intensity of elements selected across a line.[72]

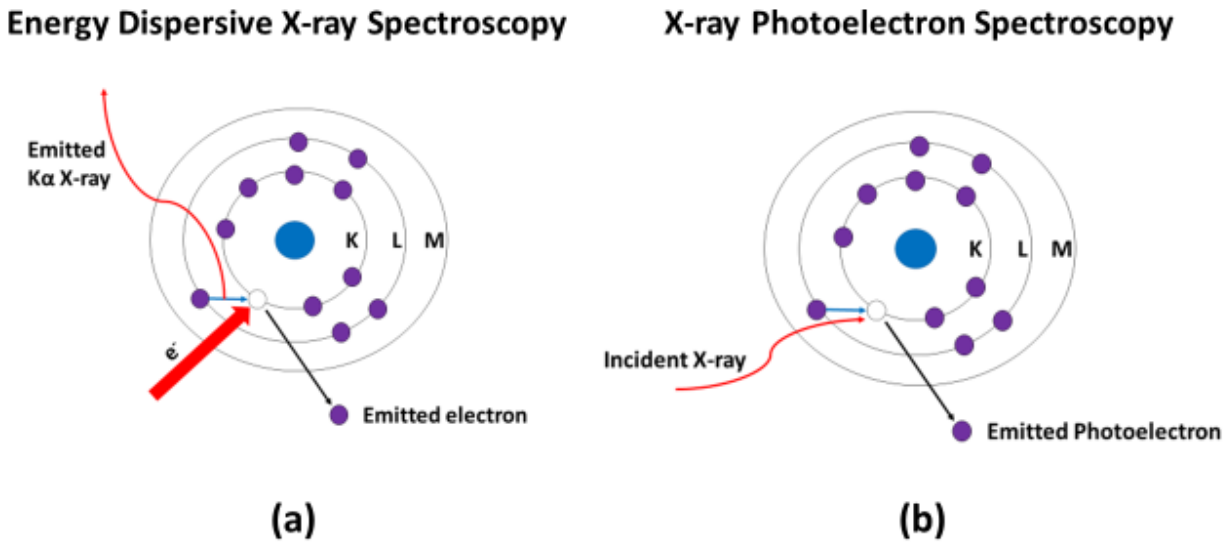

Figure 2.4.1 (a) EDS emission of x-ray from relaxation of electron from outer shell to inner shell. (b) X-ray emission of photoelectron for XPS.

2.5 X-ray Photoelectron spectroscopy

X-ray photoelectron spectroscopy (XPS) uses characteristic electrons emitted from a solid to determine the binding energy of an element within a specimen. It is a technique with similar principle to EDS except it uses x-rays to emit a photoelectron from its inner shell rather than detection of an x-ray from bombarding the sample with electrons as observed in the schematic in Figure 2.4.1b. XPS is a surface characterization technique as the photoelectrons escape approximately 10 nm within the sample in comparison to several micrometers the emitted x-rays travel in EDS. The photoelectron has a kinetic energy term E_K which can be converted to binding energy through the relationship expressed in eq 3

$$E_B = h\nu - E_K - \phi \tag{3}$$

where E_B is the binding energy, h is Planks constant, ν is frequency, and ϕ is the energy required for an electron to escape the materials surface. Likewise the spectra is in terms of intensity as a function of binding energy where the peaks are identified by the element, the shell from which the electron was emitted, and fractions which represent the total angular momentum for individual shell electron.

The chamber for XPS similar to other electron spectroscopy techniques is under ultra-high vacuum (10^{-8}-10^{-10} mbar) to prevent electron scattering from gas molecules. Due to the high sensitivity of XPS the chamber also needs to be baked at elevated temperatures to get rid of adsorbed gas molecules on chamber walls. The x-ray gun works similar to the XRD x-ray tube where high speed electrons strike the anode composed of either aluminum or magnesium. XPS uses aluminum and magnesium instead of copper and molybdenum used in XRD because they have a line width

less than 1 eV that leads to good energy resolution. The chamber will need magnetic shielding to prevent the electrons trajectory to be effected by an external field.

In order to detect the electrons they need to go through a concentric hemispherical analyzer which has 2 hemispheres with radii R_1 and R_2. Two different voltages are applied to each hemisphere to give a median voltage (V_o) between the 2 hemispheres. Before electrons enter the analyzer they go through an electrostatic transfer lens which reduces the speed of the electron to obtain an energy level in which they can be analyzed. The concentric hemispherical analyzer only lets electrons through to the detector with an energy equivalent to the median voltage between the 2 hemispheres called the passing energy. Once electrons pass through the detector they can be expressed as binding energies on an XPS spectra.[72] Figure 2.5.1 shows a schematic of the chamber and concentric hemispherical analyzer of XPS.

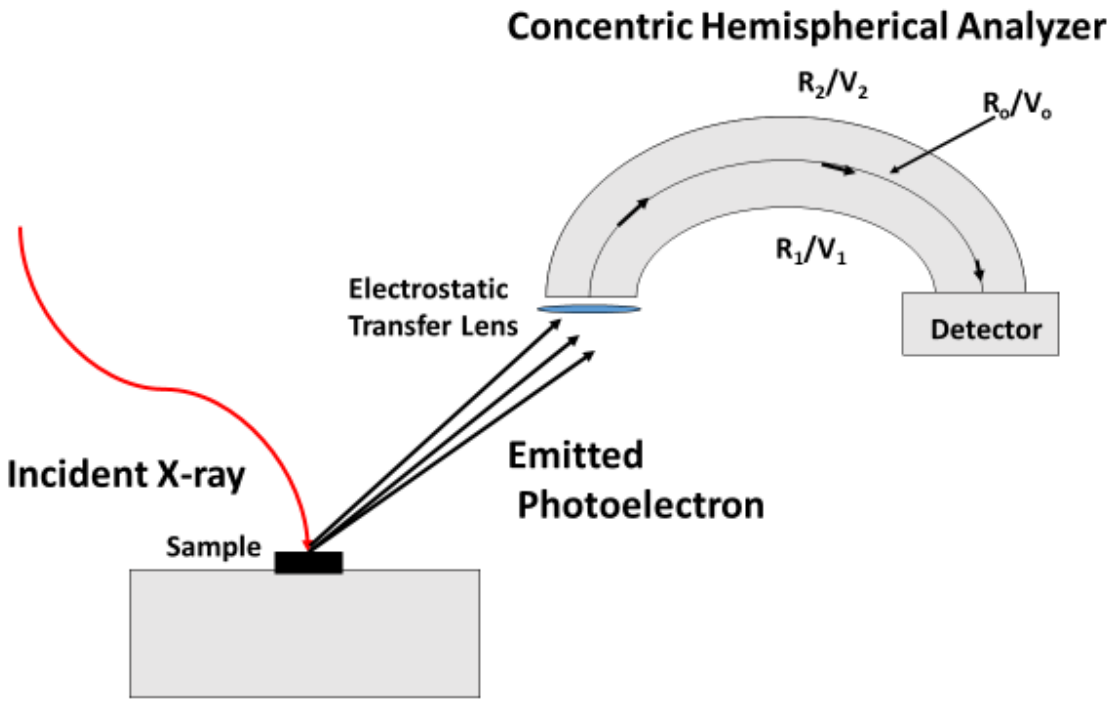

Figure 2.5.1 Instrumental schematic of XPS composed of the sample chamber and the concentric hemispherical analyzer.

2.6 Vibrating Sample Magnetometer

Vibrating sample magnetometer is a technique used to measure the magnetic properties of a material. VSM was founded by Simon Foner at MIT in 1955.[74] Figure 2.6.1 shows the main components of a VSM where a sample is loaded in an evenly distributed electromagnetic field attached to a nonmagnetic piezoelectric material which vibrates perpendicular to the field direction when current is passed through. Pick up coils near the sample capture the electric field formed from the material which is proportional to the samples magnetization.[75]

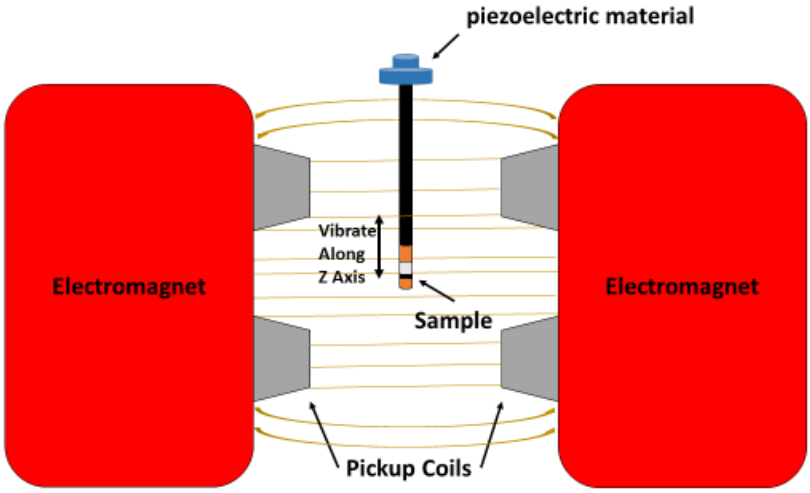

Figure 2.6.1 Main components of a VSM which consist of an electromagnet, pickup coils, piezoelectric material, and a sample holder.

Magnetization can be measured as a function of external field, temperature, or crystal orientation. Hysteresis loops or M-H curves, discussed in Chapter 1 measure the change in magnetization with external field H and is a simple route of determining magnetic properties such as magnetic saturation, magnetic remanence, coercivity, exchange bias properties, domain size, as well as the

form of magnetic material (ferromagnetic, paramagnetic, diamagnetic ex..). H_C can be determined by taking the average of the demagnetization fields when applying the positive field (H_{cright}) and the absolute value of the negative external field (H_{Cleft}) shown in eq 4. Exchange bias is calculated by taking negative absolute value of the sum of H_{Cleft} and H_{Cright} divided by 2 shown in eq 5. An upper limit on the domain size (D_{mag}) from the slope of the line as the M-H curve approaches a $H_C = 0$ can determined from the expression in eq 6.[76] Where k_B is Boltzmann's constant, T is temperature, dM/dH is the change in susceptibility, ρ is the bulk density of the material, and M_s is magnetic saturation.

$$\frac{H_{\text{Cright}} + \left|H_{\text{Cleft}}\right|}{2} = H_{\text{C}} \tag{4}$$

$$-\frac{\left|H_{\text{Cright}} + H_{\text{Cleft}}\right|}{2} = H_{\text{B}} \tag{5}$$

$$D_{\text{mag}} = \left[\frac{18k_{\text{B}}T\dfrac{(\text{d}M)}{\text{d}H}}{\pi\rho M_s^2}\right]^{1/3} \tag{6}$$

Magnetization as a function of temperature or M-T curves are normally called field cooled/zero field cooled curves (FC/ZFC). In order to run FC/ZFC curves first the temperature is raised above that of the phase change of the material (T_C or T_N) to disorient the spins in the sample. Next the sample is cooled through the blocking temperature to the lowest temperature possible where the free spins should be frozen in a certain orientation. Next the sample is heated in an external field where susceptibility is measured as a function of temperature (ZFC). Once the temperature has

reached a certain set point the temperature is cooled once more except within the same external field and FC is recorded by heating the sample in an external field. Kinks within the curves are normally signs of magnetic transitions or a crystal phase transition.[77]

One of the benefits of using VSM is the ability to measure the magnetic properties of a single crystal with ease. Other methods include measure of force in a non-uniform magnetic field. Though, it is difficult to measure materials whose magnetic properties differentiate with orientation as in highly anisotropic materials. Aligning a sample parallel to the easy axis of a single crystalline material may cause increases in saturation, squarness factor, as well as coercivity.

2.7 Thermal Gravimetric Analysis

Thermal gravimetric analysis (TGA) is a technique which measures the mass of a sample as a function of temperature which is dependent on a controlled program. The instrumentation of this system contains a balance, thermocouple, gas flow system, and an oven. It can be used to measure water absorption, lifetime predictions, and thermal stability which is important for a range of applications. It has been used extensively to obtain information on decomposition mechanism for various materials. Moreover, quantitative analysis can be improved if TGA is paired with gas chromatography, FTIR, or mass spectrometry. TGA finds usefulness in areas such as kinetics, and thermodynamics.

2.8 Raman Spectroscopy & Fourier Transform Infrared Spectroscopy

Raman and infrared spectroscopy are complimentary techniques which measure the vibrational modes of a molecule. While Raman and infrared contain many similarities, they differ in their mechanism for detection of various vibration modes. Consequently some bands are not active in both techniques.[78]

Raman was founded by Sir Chandrasekha Venkata Raman in 1928 which used inelastic scattering of photons called Raman scattering to detect the vibrational modes of a molecule. Within Raman scattering a monochromatic light source excites an electron to a virtually excited state. The electron is relaxed to a ground state higher than its initial state (Stokes scattering) or lower than its initial state (Anti-stokes scattering) due to loss or gain of energy from the stretching and bending of the bonds of a molecule. The shifts are proportional to different stretching and bending modes of a molecule which are detected in Raman spectroscopy

While Raman relies on a monochromatic excitation IR active structures absorb infrared radiation which causes stretching and bending of a molecule. FT-IR is a form of infrared spectroscopy which is generally used in the present day. The main components needed for FT-IR are observed in Figure 2.8.1 which includes an infrared source, a moving and fixed mirror, beam splitter, sample cell, and IR sensor. It uses a beam splitter to reflect 50% of the infrared radiation to a stationary and mobile mirror before the two reflected light sources are recombined. The moving mirror causes continuous change in pathlength and forms an interferogram which passes through the sample. There are generally two types of detectors which include a DTGS, a detector which detects heat and MCT detector which detects photons. The detected data is then converted into a spectrum using Fourier transformation.

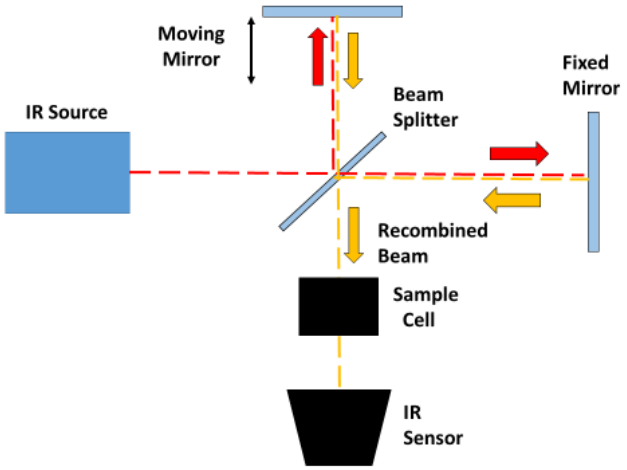

Figure 2.8.1 Instrumentation for Fourier transformation infrared spectroscopy which includes an IR source, a moving and fixed mirror, beam splitter, sample cell, and IR sensor.

Raman as discussed before uses monochromatic light as the incident photon source. Once the photons are scattered by the specimen, light goes through a filter to rid of Raleigh scattering and anti-stokes. Hence, stokes scattering solely gets detected. Both forms of spectroscopy result in similar data, but differ in the fact that Raman depends on change in polarizability while IR is measuring the change in dipole moment. Resulting in some molecules being only Raman or IR active. A rule of thumb is that structures that have strong IR intensities are more ionic, while structures with a strong Raman band are more covalent. For instance, IR cannot detect diatomic molecules (N_2) and symmetric vibrations such as C=C, C≡C, P=S, C-S are weak in IR while molecules with a high dipole moment such as O-H, and N-H have strong IR bands.[78] Due to the strong detection of sp^2 hybridized C=C bonds, Raman can detect lattice structures of graphene called the G band, as well as other sp^2 hybridized materials such as amorphous carbon, carbon nanotubes and graphite. Raman can also pick up on symmetry breaking of these carbon based structures called the defect band or D band.[79]

Chapter 3. Synthesis of Fe_7C_3 and Fe_3C Nanostructures with Phase and Morphology Control

3.1 Overview/Motivation

The main goal of this chapter was to develop a wet synthesis method for pure phased iron carbide. Within literature, there is a lack of simplistic methods for synthesizing iron carbide materials. Once a method for synthesizing pure iron carbide along with necessary analysis on the composition was established, routes to controlling particle size, shape, and crystal phase were determined. Vibrating sample magnetometer was utilized determined how manipulating the physical dimensions of the carbide as well as crystal phase controls the magnetic properties.

3.2 Introduction

Recently, promising work has taken place in the development of nanostructures of iron carbide systems. Their notable ferromagnetic behavior has potential for many applications such as contrast agent for MRI, drug delivery, hyperthermia, data storage, electromagnetic protection, and magnetic sensors.[40,80,81,82] Iron carbide (Fe_xC) systems possess higher magnetization compared to different types of pure metals, oxides and alloys such as Ni, Fe_3O_4, NiRu, and Co_3C.[83,84,85,86,87] Metallic iron may contain a greater magnetization than iron carbide. However, iron is prone to oxidation in air unlike iron carbide, which is stable in the presence of oxygen.[80,82]

Based on the phase diagram of Fe-C system, there are various crystal phases of Fe_xC with different stoichiometric ratios such as cementite Fe_3C (orthorhombic), Hagg carbide Fe_5C_2 (monoclinic), and Eckstrom-Adcock Fe_7C_3 (hexagonal). Many studies have been conducted on Fe_3C and Fe_5C_2 phases while very little work has been noted for Fe_7C_3 due to its metastable nature, or preferable formation of other phases at similar conditions.[41] Prior work has shown further development in synthesizing Fe_7C_3 as a catalyst for Fischer-Tropsch to form various carbon chains as well as carbon filaments, but in the presence of other carbides or metallic iron.[88,89] A magnetic study showed the superiority of the Fe_7C_3 phase in comparison to Fe_5C_2 based on an observed increase in coercivity and magnetic remanence with increased Fe_7C_3 crystal phase.[90]

Eckstrom and Adcock were the first to synthesize hexagonal Fe_7C_3 using their fluidized-bed hydrocarbon synthesis plant in 1950.[91,92] In earlier work, only a few methods have been developed to synthesize Fe_7C_3 utilizing such methods as physical pyrolysis, high temperature high pressure (HTHP) and Fischer-Tropsch reactors, but lack control of size and morphology.[90,93,94] Recently further work has shown improvement in controlling these properties, such as development of a solvothermal method to synthesize Fe_7C_3 nanowires with a thickness below 100 nm.[95] Furthermore, ball milling of metallic iron in toluene was used to form Fe_7C_3. HTHP method was used recently to synthesize carbon coated Fe_7C_3 nanoparticles using ferrocene.[81, 96] Each of the previous syntheses were successful in synthesizing Fe_7C_3 with the sole drawback stemming from the use of costly machinery. The lack in preparation methods in synthesizing this metastable carbide makes it difficult for further development, as a result, limited characterization of the Fe_7C_3 carbide phase exist.

In previous work from the Carpenter group a simplistic thermal decomposition route with iron fumarate was used to synthesize orthorhombic Fe_3C.[97] Though the route is simple, the high

temperature needed to decompose the fumarate as well as the lack of a template would make it difficult to control the physical dimensions of the material. In order to further explore the properties of iron carbide a wet synthesis method with an iron carboxylate group that decomposes at a relatively low temperature was developed for a simple route for synthesizing iron carbide. Cationic surfactants such as CTAB are normally used as a template for controlling particle morphology.[98] However, these surfactants have been utilized before for controlling crystal phase, such as Co and Co-Ni alloy from face centered cubic (fcc) to hexagonal close packing (hcp) crystal structures by changing the concentration of surfactant.[99,100] This mechanism is used here to develop a novel wet synthesis method for synthesizing Fe_7C_3 and Fe_3C magnetic nanoparticles using hexadecyltrimethylammonium chloride and bromide (CTAC and CTAB) which has been shown to control crystal phase, size, and morphology. In addition, this simple route can be used to manipulate the physical properties of Fe_xC, making this synthesis a potential route for further development of catalytic and magnetic applications.

3.3 Experimental

3.3.1 Preparation of Iron Carbonate

Approximately 2.0 g of sodium carbonate anhydrous (Mallinckrodt) was added to 15 mL of deionized water. The solution was magnetically stirred at 80 °C. Once the carbonate dissolved, 4.0 g of iron (II) chloride tetrahydrate (Sigma Aldrich) was added to solution upon which a color change to green was noted followed by 30 minutes of stirring. The color changed from green to a brown/orange before being placed under vacuum-filtration.

3.3.2 Cl^- Induced Synthesis of Iron Carbide

Into a three neck round bottom flask containing 0.152 g of iron carbonate and 15 mL oleylamine (TCI), CTAC or CTAB (Sigma Aldrich) was added to maintain concentrations at either 18.3, 9.14, 4.58, or 2.29 mM. The reaction was purged with nitrogen before the mixture was heated to 335 °C with a ramp rate of 20 °C min^{-1}. An increase in CTAC concentration resulted in an increased ramp rate to 365 °C ranging from 1°C min^{-1} to 6 °C min^{-1} from 2.29 mM to 18.3 mM CTAC. The total reaction time from reaction initiation to dwell time at reflux was at 45 minutes after which the reaction vessel was cooled to room temperature. The particles were washed 3 times in hexane and methanol following sonication for 2 minutes and subsequent magnetic separation. All products were dried under vacuum for 24 hours.

3.3.3 Br^- Induced Synthesis of Iron Carbide

Into a three neck round bottom flask containing 0.152 g of iron carbonate and 15 mL oleylamine. CTAB (Sigma Aldrich) was added to maintain concentrations at either 18.3, 9.14, or 4.58 mM. The reaction was purged with nitrogen before the mixture was heated to 335 °C with a ramp rate of 20 °C min^{-1} followed by a 6 °C min^{-1} ramp rate to reflux. The total reaction time from reaction initiation to dwell time at reflux was at 45 minutes after which the reaction vessel was cooled to room temperature. The particles were washed 3 times in hexane and methanol following sonication for 2 minutes and subsequent magnetic separation. All products were dried under vacuum for 24 hours.

3.3.4 Characterization

Crystal structure and phase analysis were done using a Panalytical X'Pert Pro MPD diffractometer under Cu Kα ($\lambda = 1.5418$ Å). Analysis of all XRD data was performed using X'Pert HighScore Plus software, which was used to determine percent phase composition and Scherrer analysis. Rietveld analysis was used in Highscore, using lattice parameters from Pearsons

Handbook of Lattice Spacings and Structures of Metals.[101] SEM imaging of all products was carried out using a Hitachi SU-70 SEM. Energy dispersive x-ray spectroscopy (EDS) was conducted in order to gain the elemental composition of the material under study. Magnetic characterization was performed using a Quantum Design Versalab Vibrating Sample Magnetometer (VSM).

3. 4 Iron Carbide Synthesis in Oleylamine

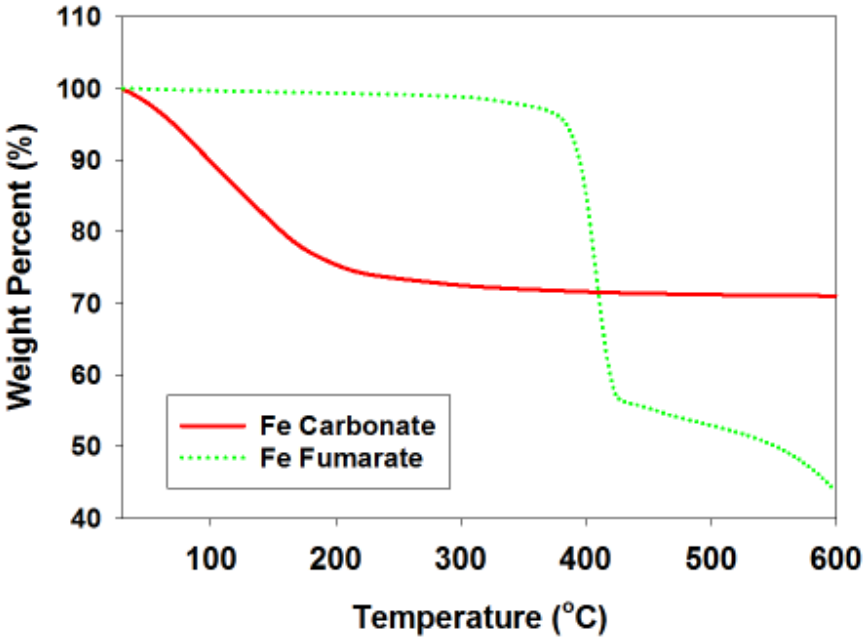

Figure 3.4.1. Thermal gravimetric analysis of iron carbonate (dotted line) and iron fumarate (solid line).

Figure 3.4.1 shows a thermal gravimetric analysis (TGA) of iron fumarate used previously in comparison to iron carbonate. The results show iron carbonate dissociates gradually until 230 °C while the fumarate starts to decompose at 400 °C, which makes iron carbonate a reasonable

candidate to attempt to reduce in a high boiling point solvent such as oleylamine. Figure 1a. shows the XRD diffraction pattern of the synthesis with only the precursor and oleylamine. The diffraction pattern shows presence of mainly orthorhombic Fe_3C with some Fe_3O_4 with broad peaks and a notable low signal to noise which shows the sample is within the nano realm in size with low crystallinity. The reaction itself took a total of 1 ½ hrs which included approximately 15 minutes to reach 335 °C with a final temperature reading between 340 °C - 365 °C. The slow ramp rate lead to the slow decomposition of oleylamine/reduction source and impurities within the system which was reflected in its magnetic data with low magnetization saturation values ranging from 60 emu g^{-1} to 70 emu g^{-1}. Going forward the variation in reaction conditions, impurities within the system, and low crystalline material had to be addressed. Previous reports have shown halogen-ions to assist in the formation of crystalline material such as work by Zhang et al. who said the addition of Br^- and Cl^- halogens favor thermodynamic growth of crystalline iron nanoparticles (Example shown in Figure 3.4.2 below).[102] Previous reports on use of halogen induced synthesis of nanoparticles lead to further investigation with surfactants CTAB and CTAC.

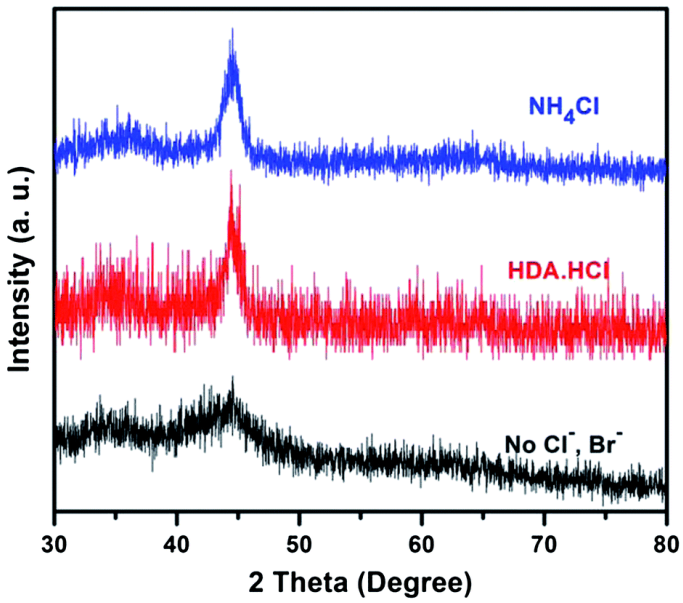

Figure 3.4.2. Zhang et al. report of increase crystallinity in nanoparticle synthesis with addition of halogen species.[102]

3.5 Fe_3C and Fe_7C_3 Characterization

Results shown in Figure 3.5.1(b,c) represent diffraction patterns using different concentrations of CTAB and CTAC which resulted in predictable reaction conditions, with high purity and crystalline iron carbide, mainly due to the increase ramp time to reflux which lead to full reduction of the material. Recent reports have found decomposition of aliphatic amines to be the carbon source in carbides through formation of methane gas.[103] Therefore, the slow decomposition of oleylamine without an inducing agent may lead to oxide impurities observed in Figure 3.5.1a from low percentages of carbon source within the mixture. The addition of

cationic surfactants also showed the capability of controlling crystal phase, as well as size and shape within this system discussed below.

The crystal phase of the synthesized Fe_xC nanoparticles at different CTAC concentrations was investigated using the XRD diffraction as shown in Figure 1 Rietveld analysis was used to determine the percent phase composition of each sample. The patterns show the formation of Fe_7C_3 and Fe_3C phase structures with different percentages based on the concentration of CTAC. The Fe_7C_3 and Fe_3C percentages and crystallite size of both phases were determined from the XRD patterns as presented in Table I.

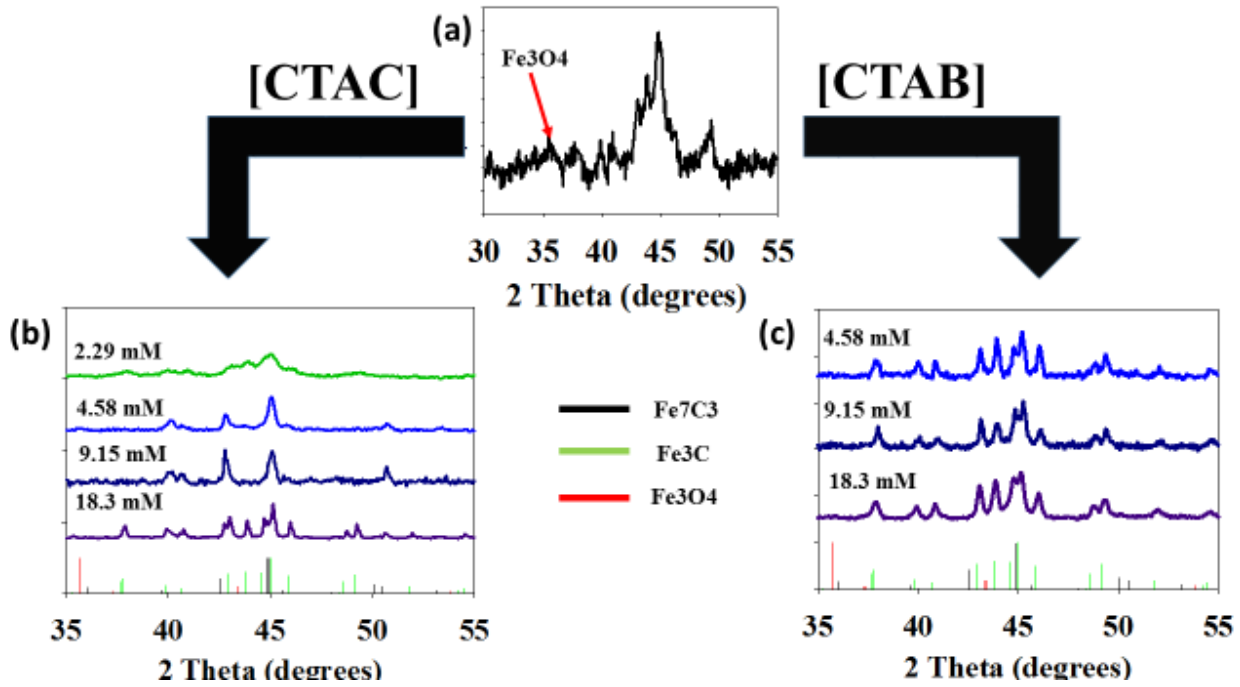

Figure 3.5.1. X-ray diffraction patterns for the Fe_xC nanoparticles made (a) without a surfactant, (b) CTAC, and (c) CTAB. References for Fe_3C (PDF 01-089-2722), Fe_7C_3 (PDF 01-089-7273), and Fe_3O_4 (PDF 01-075-0449) are shown for comparison.

As shown in Table I, addition of CTAC affects the Fe_xC crystal phase as well as the crystallite size. A phase change from 73.2 % Fe_3C with 26.8 % Fe_7C_3 to pure phase Fe_7C_3 occurred from decreasing the CTAC from 18.3 to 9.15 mM. A further decrease in CTAC concentration to 2.29

mM resulted in a gradual change to pure Fe_3C. The estimated Scherrer crystallite size for Fe_3C and Fe_7C_3 shows a gradual decrease with lower CTAC concentrations demonstrating control of both crystallite size and carbide phase. Previous work has demonstrated that varying CTAC or CTAB concentration can mediate crystal phase transitions, such as that observed in cadmium sulfide systems.[104]

Similar to CTAC, the addition of CTAB resulted in an increase in crystallinity. However, the bromine-induced synthesis did not show any crystal phase transition with change in concentration as all the samples resulted in orthorhombic Fe_3C. Moreover the sharp peaks witnessed in all the crystal patterns with Scherrer values around 75 nm for all samples shows concentration has less of an effect on the size of the material as well. The difference in bromine and chlorine may be due to the size and electronegativity of the halogens. Chlorine is more electronegative and would have a better orbital overlap with iron due to its size, therefore chloride ions would have a greater affinity to bind to iron than bromide.

Table 3.5.1. Fe_7C_3 and Fe_3C phase % and crystallite size (nm) for each [CTAC] mM**.**

CTAC (mM)	**Fe_7C_3 %**	**d_{XRD} (nm) Fe_7C_3**	**Fe_3C %**	**d_{XRD} (nm) Fe_3C**
18.3	26.8	71.6	73.2	102.0
9.15	100	42.7	0	-
4.58	68.3	31.1	31.7	24.2
2.29	0	-	100	18.3

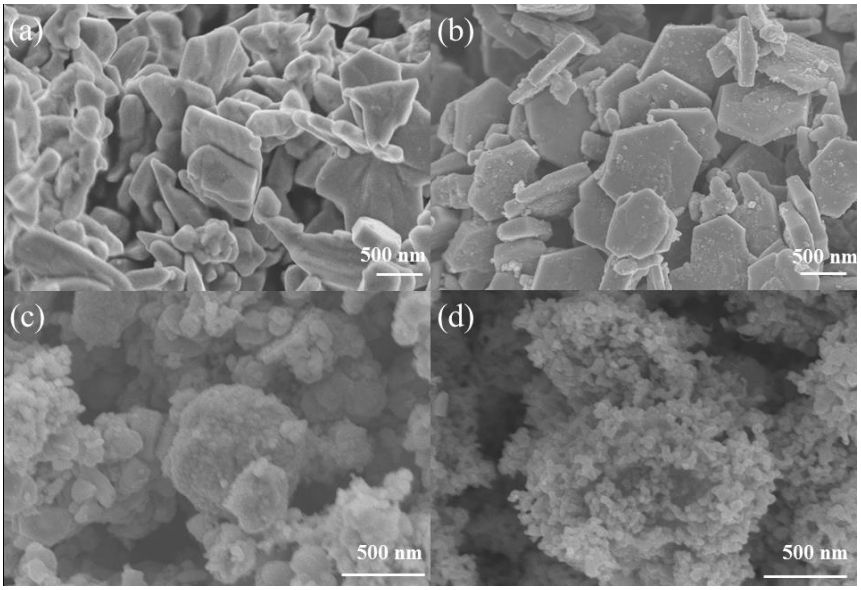

Figure 3.5.2. SEM images of various phases of Fe_xC samples synthesized using (a) 18.3, (b) 9.15, (c) 4.58, and (d) 2.29 mM CTAC.

The morphology of the iron carbide nanoparticles was investigated using SEM as seen in Figure 3.5.2(a-d). Upon initial inspection in Figure 3.5.2a, (18.3 mM CTAC) a mixture of morphologies is present, however upon close inspection, hexagonal structures are observed throughout the sample. Lowering the concentration of CTAC to 9.15 mM, the sample exhibits formation of hexagonal prisms with average diameter and thickness of 1 μm and 150 nm respectively in Figure 3.5.2b. A noticeable decrease in size was observed when CTAC concentration was decreased to 4.58 and 2.29 mM in Figure 3.5.2(c, d). Figure 3.5.2c shows cauliflower-like particles for the sample synthesized at 4.58 mM CTAC with diameters ranging from 50-200 nm. Further lowering of the concentration of CTAC to 2.29 mM resulted in a decrease in particle size to approximately 50 nm. The pure phase Fe_7C_3 and Fe_3C were synthesized multiple times to ensure reproducibility

of phase and morphology. This reduction in size correlates with the decrease in crystallite size calculated using Scherrer analysis shown in Table 3.5.1. The observed increase in particle size with a quaternary amine has also been witnessed in a previous synthesis of iron nanoparticles with hexadecylammonium chloride.[69] Figure 3.5.3 shows an example of a micrograph of the iron carbide synthesis with CTAB. The large crystallite sizes (approximately 75 nm for each sample) determined from Figure 3.5.1 were in agreement with the large particles with dimensions around 500 nm in length and 300 nm in width. It must be noted there is a lot of uncertainty with determination of crystallite size with XRD, however it may be used for relative change in different parameters.[105] Most of the sample resembles an orthorhombic pyramid shape, which is analogous to its orthorhombic crystal structure.

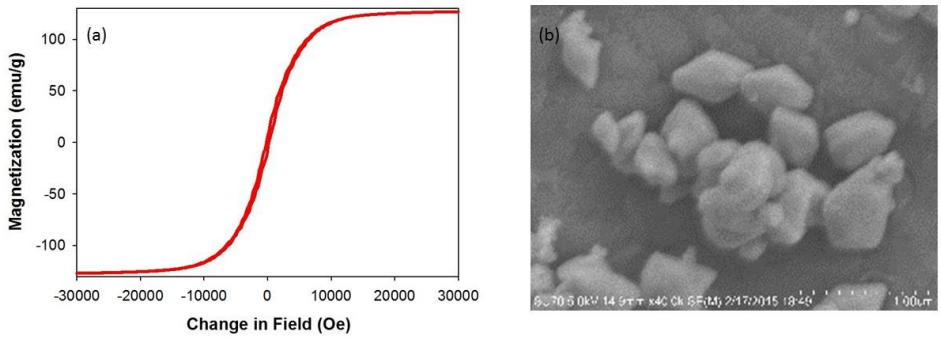

Figure 3.5.3. (a) Hysteresis of Fe_3C synthesized with CTAB. (b) Scanning electron micrograph of Fe_3C synthesized with CTAB.

3.6 Magnetic Analysis

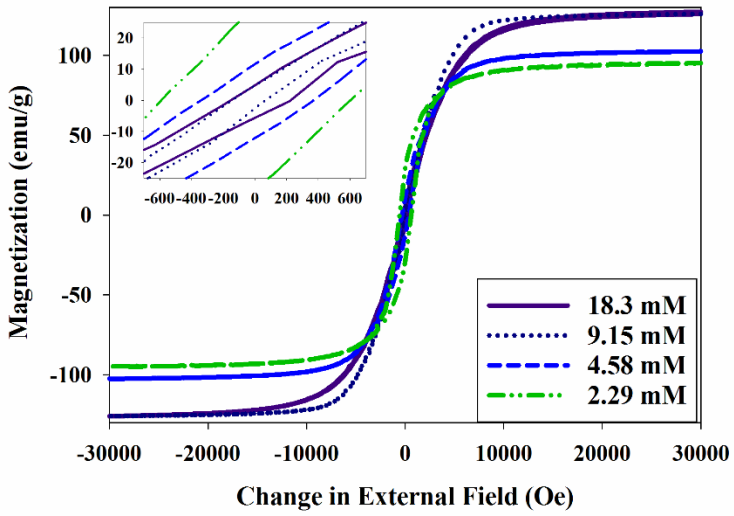

Figure 3.6.1. M-H curves at 300 K for the samples synthesized at CTAC concentration ranging from 18.3 mM (solid), 9.15 mM (dotted), 4.58 mM (dashed), and 2.29 mM (dashed and dotted).

In order to investigate the magnetic properties of the Fe_xC nanoparticles, the field dependent magnetization was measured as shown in Figure 3.6.1. The hysteresis curves of the carbide samples reveal ferromagnetic behavior for all the samples. The results were listed in Table 3.6.1 for all the samples synthesized at different CTAC concentrations. As seen from Fig. 3 and Table II, higher concentrations of CTAC led to an increased saturation magnetization (M_s), and decreased coercivity (H_c). The decrease in magnetization with decreased particle size has been observed in previous work and is attributed to the decrease in surface to volume ratio as well as the dilution of saturation magnetization due to surface oxidation.[106] The increase in the H_C observed in Figure 3.6.1 and Table 3.6.1 at a lower concentration of CTAC is due to a transition from a multi-domain system closer to a single domain system. Consequently increasing the

external field needed to demagnetize the material. This gradual change from semi-hard to soft material for iron carbide shows this materials potential for a wide range of magnetic applications by fine-tuning its physical dimensions.

To confirm the change in magnetic properties was due to particle size, rather than crystal phase, pure Fe_3C with similar dimensions was synthesized to show the resemblance of the magnetic properties with pure Fe_7C_3 (Figure 3.5.3). The sample had an M_s of 127 emu/g and coercivity of 175 Oe comparable to the magnetics of pure Fe_7C_3. Previous magnetic studies on micron sized Fe_3C and Fe_7C_3 systems show that the two phases have analogous magnetic values of 125 emu/g and 120 emu/g for Fe_3C and Fe_7C_3.[94]

Further information is obtained from Figure 3.6.1 such as the magnetic domain size and the type of magnetic anisotropy. The biggest magnetic domain size can be implied from the magnetization studies by evaluating the initial slopes near the zero field of the M-H curves.[86] The major contribution to the initial slope arises from the largest particles. Their larger magnetization vectors are more easily oriented by a magnetic field and thus an upper boundary for the magnetic size d_{mag} can be estimated for hysteresis at 300 K to be from 4.2 to 6.4 nm based on the CTAC concentration (Table 3.6.1).[86] The nature of the magnetization axis (uniaxial or cubic anisotropy) can be determined by the remanence to saturation ratio (Mr/Ms). From Table 3.6.1, the Mr/Ms values reveal 0.04–0.3. The results showed that our particles are in the uniaxial anisotropy range rather than the cubic anisotropy range which demands Mr/Ms to equal 0.87.[107]

Table 3.6.1. Magnetic saturation, coercivity, Mr/Ms, and domain size obtained from the M-H curves based on the CTAC concentrations.

CTAC **mM**	M_S emu/g	H_C Oe	Mr/Ms	d_{mag} nm
2.29	95	590	0.3	6.4
4.58	103	340	0.1	5.2
9.15	126	170	0.04	4.4
18.3	127	154	0.04	4.5

Work from Shin Tajima and Shin-Ichi Hiran show similar magnetic properties between Fe_3C, Fe_5C_2, and Fe_7C_3.[90]

For more details on the magnetic properties of the majority Fe_7C_3 phases (9.15 mM and 4.58 mM), zero field cooled (ZFC) and field cooled (FC) with 500 Oe applied field, as well as hysteresis at temperatures ranging from 50 K to 300 K were measured (Figure 3.6.2 and Figure 3.6.3). Figure 3.6.2 shows the magnetic study for the Fe_7C_3 cauliflower shaped material. The ZFC in Figure 3.6.2a has steps at 56, 100, and 160 K, which correspond to blocking temperatures (T_B) for a wide size distribution of Fe_3O_4. Previously reports have shown different size superparamagnetic iron oxide to have T_B ranging from 30 K to 170 K with particle sizes ranging from 5-11 nm.[108] Therefore, the ZFC must be detecting super paramagnetic Fe_3O_4 impurities within the sample. The hysteresis at different temperature ranges showed no observable trend coercivity due to the presence of superparamagnetic iron oxide and slight increase in the M_S.

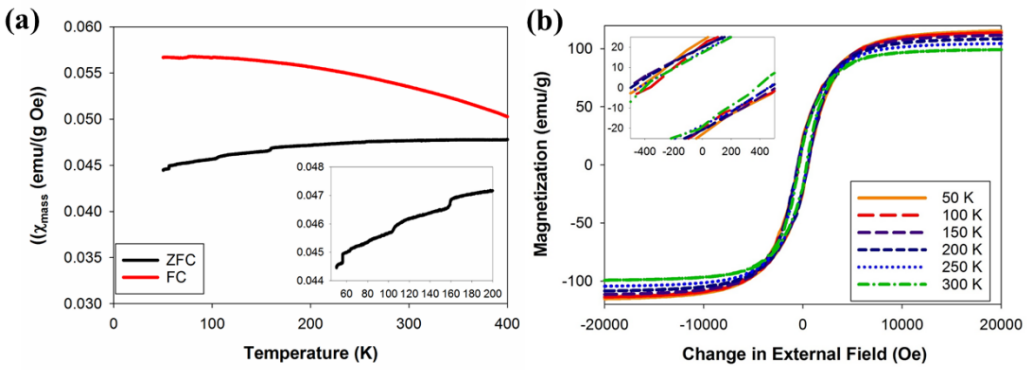

Figure 3.6.2. Extended magnetics study on iron carbide sample synthesized with 4.58 mM CTAC. (a) FC with 500 Oe field, and ZFC study with a 5 K/min sweep rate. (b) Hysteresis at temperatures ranging from 50-300 K.

Similar to the cauliflower morphology, FC and ZFC curves and the hysteresis loops at temperatures ranging from 50 K to 300 K were measured for the pure Fe_7C_3 hexagonal prisms (Figure 3.6.3). The ZFC shows one step at 100 K (Figure 3.6.3a). The fact that the ZFC only has one step shows there is less iron oxide impurity within the system and as well as a more even size distribution in comparison to the cauliflower sample. The hysteresis at different temperature ranges showed a slight increase in coercivity and slight increase in the M_S values, which is observed in soft ferromagnets due to low magnetocrystalline anisotropy energy witnessed in multi-domain systems (Figure 3.6.3b).

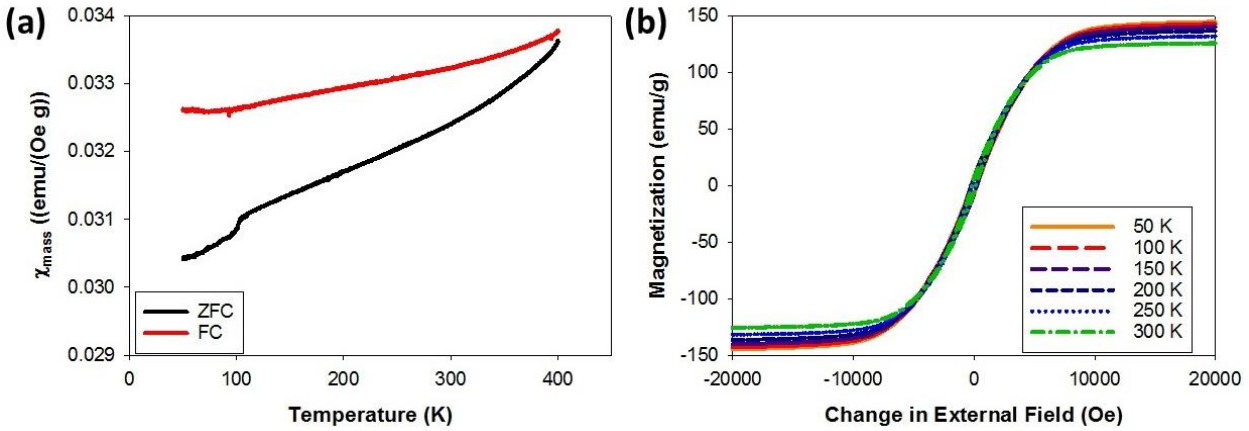

Figure 3.6.3. Extended magnetic study of the Fe_7C_3 hexagonal prisms. (a) FC with 500 Oe field, and ZFC with a 5 K/min sweep rate (b) Hysteresis at different temperatures ranging from 50 K – 300 K.

3.7 Conclusions

This work introduces a new wet chemical synthesis method for controlling phase, and morphology of Fe_xC nanostructures. CTAC has been shown to work to kinetically control growth rate, crystal phase from Fe_3C to Fe_7C_3, and morphology from nanoscale particles to nanoscale hexagonal prisms. M-H curves showed a gradual transition from semi-hard to soft material through controlling particle size. Moreover, The FC/ZFC for the Fe_7C_3 showed presence of small amount of iron oxide impurity, as well as M-H curves analogous to materials with high permeability. The diversity in magnetic properties shows potential for these nanomaterials for a broad range of magnetic or electronic applications.

Chapter 4. Mechanistic Study of Textured Fe_7C_3 Hexagonal Prisms

4.1 Overview/Motivation

In Chapter 3 a wet synthesis method for synthesizing iron carbide materials was established with the capability of controlling the crystal phase and size of the material, thus manipulating the magnetic properties from semi-hard to soft. From the array of materials, pure hcp Fe_7C_3 was the sole material successfully synthesized with shape control. Chapter 4 therefore, will focus on determining the role of solvent and Cl^- inducing agent as well as aiming to further control the physical dimensions of the material. Magnetic studies were also accomplished to explore how the shape of the structure may affect its magnetic properties. Lastly thermal stability on the hexagonal prisms were executed to further confirm the phase and to determine if the structure and synthesis method in oleylamine have an effect on its stability.

4.2 Introduction

Cationic surfactants have been used immensely for nanoparticle research in controlling the shape, size, and crystallinity of the material. Alkyl ammonium surfactants have been used extensively in synthesis of polyhedral shaped noble metals, such as silver, gold, platinum and palladium with high energy facets used to enhance their catalytic activity.[109,110,111] Unlike noble metals cationic surfactants do not lead to unique structured nanoparticles in 3d zero valent metals, however they have been used to increase the crystallinity, to enhance magnetic and catalytic properties. [102,112]

In Chapter 3 pure phase hcp Fe_7C_3 hexagonal prisms were successfully synthesized with hexadecyltrimethylammonium chloride (CTAC), with a unique diffraction pattern that shows some anisotropic crystal growth is occurring. In this chapter, the role of the CTAC and oleylamine will be explored through use of other alkyl ammonium chloride groups and aliphatic amines. A mechanistic study was completed with the assistance of XRD, SEM, and IR in order to get an understanding of the progression of crystal phase, and structure with the change in solvent composition. With the interesting anisotropic growth of these hexagonal prism structures, M-H curves were acquired at different orientations to determine if any shape or magnetocrystalline anisotropy is present. Lastly, TGA and high temperature XRD were utilized to get information of the stability of these hexagonal prism structures.

4.3 Experimental

4.3.1 Synthesis with different alkyl ammonium chlorides

Into a three neck round bottom flask containing 0.152 g of iron acetate and 15 mL oleylamine (TCI), 6.25 mM of either CTAC, cetyl pyridium chloride (CPC), or distearyldimonium chloride (DSC) were included. The reaction was purged with nitrogen before the mixture was heated to 335 °C with a ramp rate of 20 °C min^{-1} followed by a 6 °C min^{-1} ramp rate to reflux. The reaction was kept at reflux for approximately 30 minutes after which the reaction vessel was cooled to room temperature. The particles were washed 3 times in hexane and methanol following sonication for 2 minutes and subsequent magnetic separation. All products were dried under vacuum for 24 hours.

4.3.2 CTAC induced synthesis with different aliphatic amines

Into a three neck round bottom flask containing 0.152 g of iron acetate and 6.25 mM CTAC, the mass equivalent of 15 mL of various aliphatic amines which include octadecylamine (bp 350 °C), hexadecylamine (bp 330 °C), tetradecylamine (bp 290 °C), and dodecylamine (bp 250 °C) were added to the flask. The reaction was purged under nitrogen before the mixtures were heated to reflux and keeping each solution at its corresponding reflux temperature for 30 minutes before the reaction vessel was cooled to room temperature. The particles were washed 3 times in hexane and methanol following sonication for 2 minutes and subsequent magnetic separation. All products were dried under vacuum for 24 hours.

4.3.3 Characterization

Crystal structure and phase analysis were done using a Panalytical X'Pert Pro MPD diffractometer under Cu Kα (λ = 1.5418 Å). Additionally, an Anton Paar HTK-1200N heating stage with an Anton Paar TCU1000 heating control unit was utilized for the study of the Fe_7C_3 crystal structure at elevated temperatures. Analysis of all XRD data was performed using X'Pert HighScore Plus software, which was used to determine percent phase composition and Scherrer analysis. SEM imaging was carried out using a Hitachi SU-70 SEM while energy dispersive x-ray spectroscopy (EDS) was conducted in order to gain the elemental composition of the material under study. Zeiss Libra 120 was utilized to get crystallographic data through diffraction. TGA-IR studies using Thermal Analysis Q5000 model TGA were carried out to determine the composition of material loss at elevated temperatures. Magnetic characterization was performed using a Quantum Design Versalab Vibrating Sample Magnetometer (VSM).

4.4 Mechanistic Study of Fe_7C_3

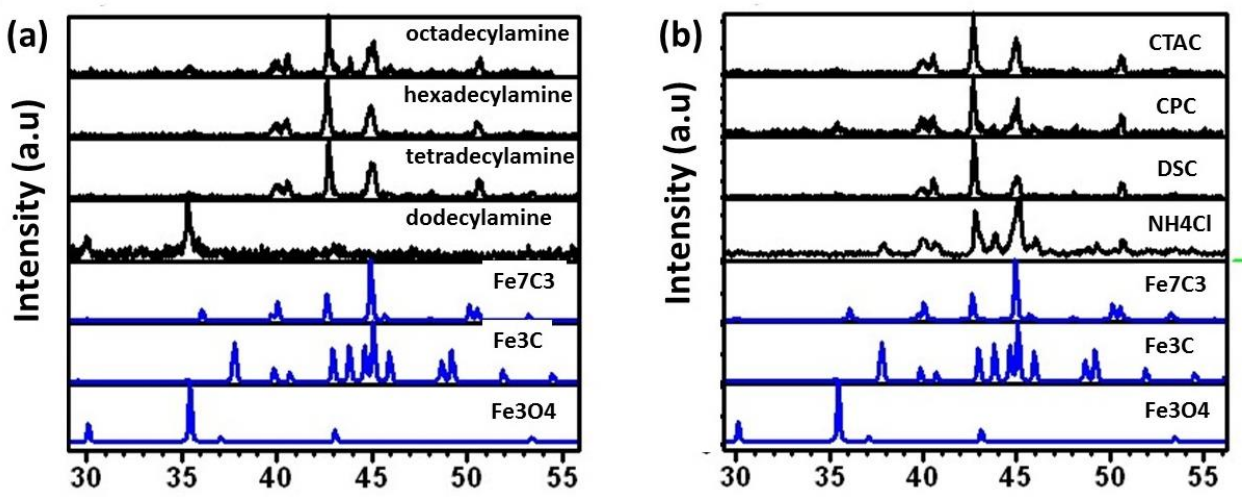

Figure 4.4.1. (a) X-ray diffraction samples synthesized different solutions: octadecylamine, hexadecylamine, tetradecylamine, and dodecylamine with 6.25 mM CTAC with 0.152 g iron acetate. (b) X-ray diffraction of samples synthesized with different ammonium Cl^- salts including CTAC, cetyl pyridium chloride (CPC), distearyldimonium chloride (DSC), and ammonium chloride. Reference patterns for hcp Fe_7C_3, orthorhombic Fe_3C, and fcc Fe_3O_4 are presented below the patterns in both figures.

X-ray diffraction patterns were utilized to determine the change in crystal phase from using different aliphatic amines and Cl^- salts in Figure 4.4.1a and b. From the solvent study, each pattern contains the hexagonal Fe_7C_3 phase with dissipation of orthorhombic Fe_3C from octadecylamine to the lower bp solvent tetradecylamine. Presence of Fe_3C in the high boiling point solvent may be due to the increase rate of carbide formation also witnessed with increase CTAC concentrations. The peak corresponding to the (102) plane at an angle of 43° shows an intensity greater than the 100% peak at angle 45° for the octadecylamine, hexadecylamine, and tetradecylamine diffraction

patterns which occurred in the hexagonal prism structures in Chapter 3. Decreasing the bp of the solvent to dodecylamine only Fe_3O_4 pattern is observed, which again can be accounted for slower reduction/thermal decomposition in lower boiling point solvents.[54]

Figure 4.4.1b diffraction patterns of CTAC, CPC, and DSC all contain the hexagonal iron carbide phase with an intense (102) plane of diffraction which shows the chloride anion as well as the long chain alkyl ammonium groups play an important role in forming textured Fe_7C_3. Reports have shown polyhedral shaped Fe_3O_4 to form from the strong bonding of alkyl ammonium chlorides to iron rich planes of the crystal structure. Therefore the alkyl ammonium chlorides may have a strong preference for the (102) plane of the iron carbide which assists in controlling the crystal structure formation of the carbide. The pattern for CPC unlike the diffraction patterns for CTAC and DSC also contain some Fe_3C impurity. Comparing the organic structures the pyridium group on CPC is bulkier and can only have one symmetric arrangement unlike the multiple aliphatic carbon chains on DSC which may lead to less packing on the (102) plane, and less control over crystal growth. The diffraction pattern for the reaction with ammonium chloride shows presence of both Fe_7C_3 and Fe_3C phases without any signs of texture in the material from its generally normal peak intensities. The changes in the diffraction pattern from changes made in the ammonium cation is a sign that the alkyl ammonium groups structure does in fact play a crucial role in iron carbide crystal growth.

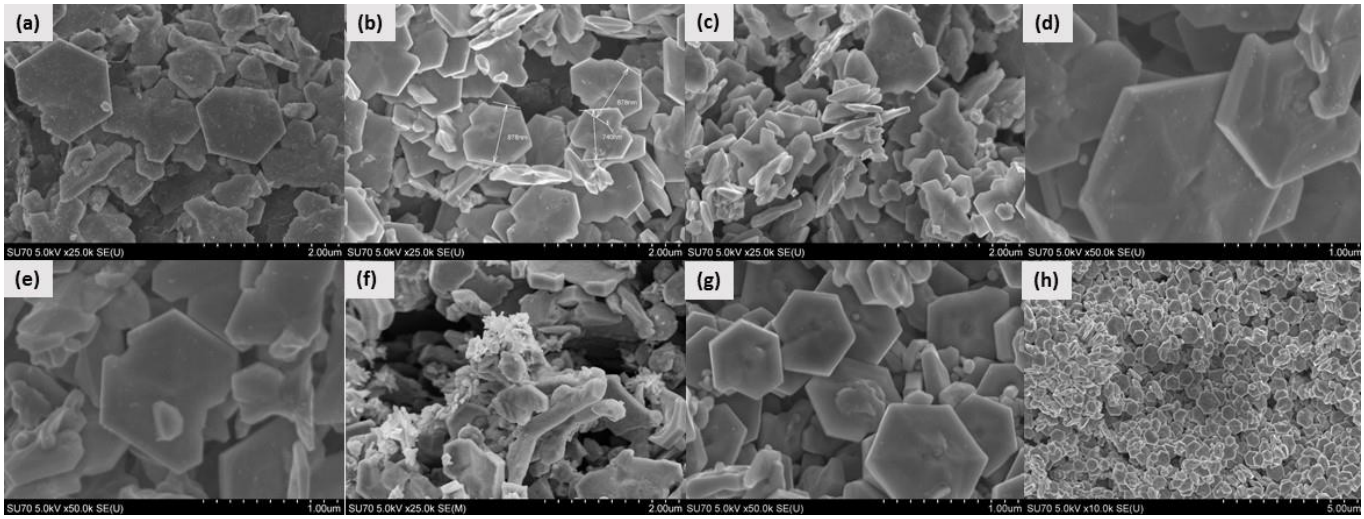

Figure 4.4.2. SEM micrographs of iron carbide synthesized in various aliphatic amines which include (a) octadecylamine, (b) hexadecylamine, (c) tetradecylamine. Figure (d)-(h) represent synthesis of carbide using different Cl^- salts: (d) DSC, (e) CPC, (f) ammonium chloride, (g) and (h) CTAC.

SEM micrographs were taken of the solvent and Cl^- trials to get insight on how different ammonium groups or aliphatic amines effect the carbides morphology. Figure 4.4.2 (a-c) represent iron carbide synthesized in different boiling point aliphatic amines were all the samples show similar hexagonal prism structures to the synthesis in oleylamine ((Figure 4.4.2 (g,h)). The iron carbide synthesized in tetradecylamine almost has no uniform shape, however the dimensions of the width of the structures decreased to as low as 75 nm. The presence of less uniform structures at lower formation temperatures can be attributed to the use of lower boiling point solvents, which leads to a slower growth step and less uniformity in particle size and shape. Despite this issue, the synthesis in lower boiling point amines shows iron carbide can be synthesized successfully at temperatures as low as 290 °C.

The samples synthesized with DSC show very similar hexagonal prism structures to the Fe_7C_3 synthesized in Figure 4.4.2 (g-h) with CTAC which shows a slight different in chain length and

structure of the ammonium complex doesn't change the overall physical dimensions of the hexagonal prisms. The SEM micrograph with CPC on the other hand shows the bulky pyridium group definitely leads to less uniform prism structures possibly due to the formation of orthorhombic Fe_3C crystal structures within the array of hcp Fe_7C_3. A synthesis with ammonium chloride was done in order to determine if a long chained alkyl ammonium group is necessary to control the dimensions of the material. Results show a polydispersed sample with some hexagonal prism material that matches the diffraction pattern of a mix phase of Fe_3C and Fe_7C_3. In conclusion, Cl^- anion plays an obvious role in forming Fe_7C_3 while long chain aliphatic ammonium groups are a necessity to form uniform hexagonal prism structures.

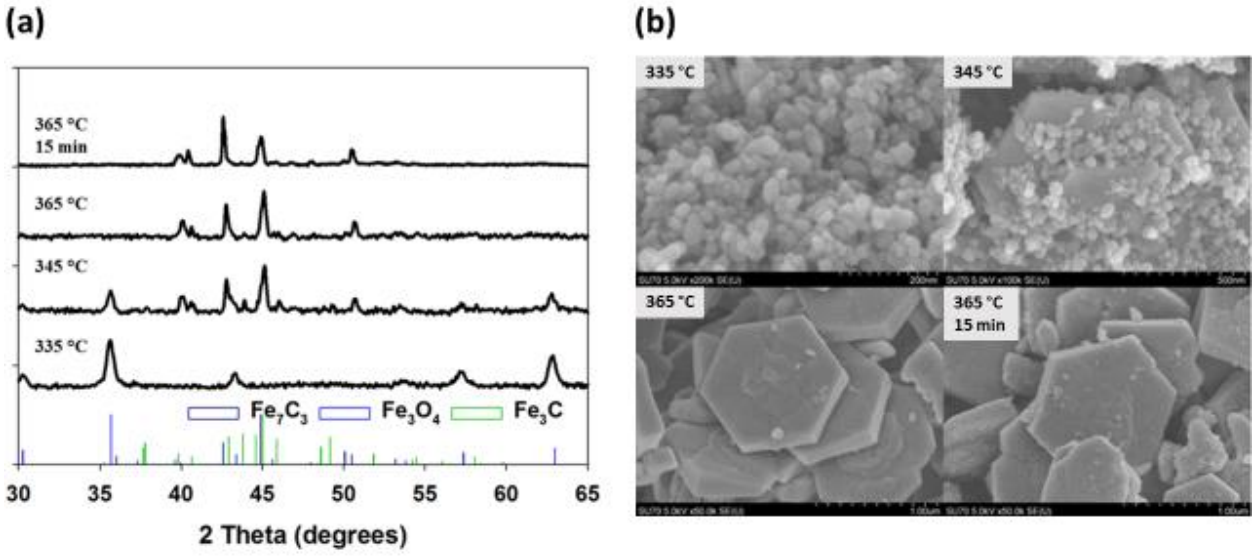

Figure 4.4.3. (a) XRD thermal study of the Fe_7C_3 system from 335 °C to reflux at 365 °C for 15 minutes. References for Fe_3C (PDF 01-089-2722), Fe_7C_3 (PDF 01-089-7273), and Fe_3O_4 (PDF 01-075-0449) are shown for comparison. SEM thermal study of formation of Fe_7C_3 prisms from 335 °C to reflux at 365 °C.

To understand the growth mechanism of the hexagonal prisms of Fe_7C_3 nanoparticles, a time study was conducted. The study was performed by taking aliquots at various time intervals followed by a XRD and SEM measurements shown in Figure 4.4.3a and b respectively. The XRD pattern for the sample prepared at 15 minutes' reaction time and 335 °C exhibits formation of Fe_3O_4 in Figure 4.4.3a and the corresponding image displays polydispersed elliptical nanoparticles in Figure 4.4.3b. Formation of intermediates shows this system follows Ostwald's step rule witnessed in many nanoparticle syntheses.[48,113] When the reaction was left for 21 minutes at 345 °C, the nucleation of the carbide begins and the formation of Fe_7C_3 with a small amount of Fe_3C was observed with dissipation of the oxide phase in Figure 4.4.3. The corresponding microstructure image shown in Figure 4.4.3b depicts the presence of hexagonal prisms with smaller particles aggregated on the surface. This intermediate phase resembles coalescence of nanoparticle clusters seen in previous work.[49]

For longer reaction times at 30 and 45 minutes and at a reaction temperature of 365 °C, the hexagonal prisms were homogeneously formed (Figure 4.4.3b) with phase structure of pure Fe_7C_3 (Figure 4.4.3a). For the sample prepared for 45 minutes reaction, there was curvature of the surface region in the center of each of these prisms due to the reduced strain on the structure (Figure 4.4.3a). Growth of the (102) plane at angle 43° can be seen with increase reaction time. It can be inferred these prism structures are grown parallel to the [102] direction.

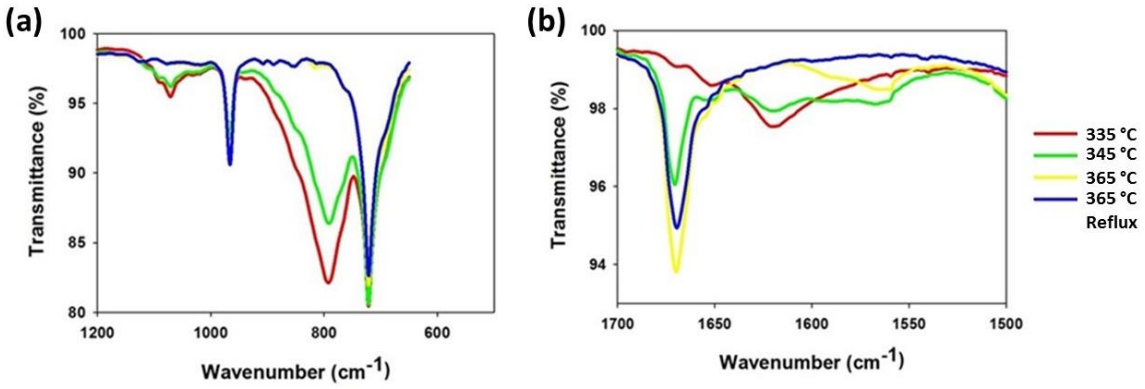

Figure 4.4.4. Solvent FTIR study taken at temperatures 335 °C, 345 °C, 365 °C, and at reflux for 5 minutes. Figure on the left showing the range from 500 to 1200 cm^{-1}. The right figure shows the range from 1500 to 1700 cm^{-1}.

A FTIR study on the solution gathered from the aliquots taken were analyzed in Figure 4.4.4a and b to gain more insight on the role of the aliphatic amine in the formation of the Fe_7C_3 crystal phase. As time progresses the N-H stretch at 790 cm^{-1} and the NH_2 scissoring absorption at 1620 cm^{-1} decrease as the C=N stretch at 1670 cm^{-1} forms. Recent reports with silver and iron nanoparticles have shown aliphatic amines can be used as a reducing source as witnessed from the reduction of the precursor with the progressive dehydrogenation of the solvent.[69,63] Therefore, the amine goes through a dehydrogenation reaction to reduce the mixed iron (II)/(III) valence state to iron (0), and is a practical way of tracing the progress of the reaction.

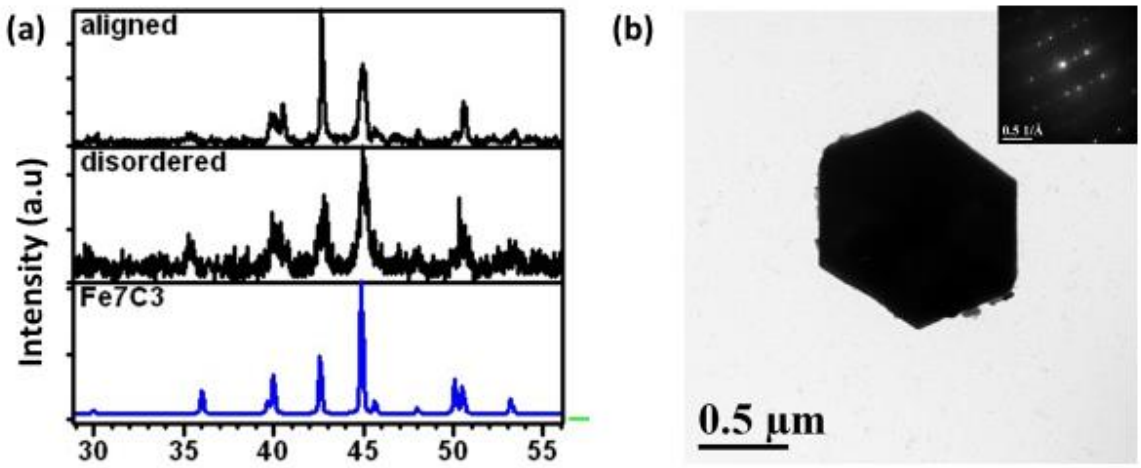

Figure 4.4.5. (a) X-ray diffraction pattern (aligned) prepared by aligning the sample with a neodymium magnetic with the face of the plate's oriented perpendicular to the sample holder. (disoriented) Diffraction pattern with no sample preparation. (b) Transmission electron micrograph of a single Fe_7C_3 hexagonal plate with an inset of the EELS diffraction pattern of the single crystalline structure.

In order to further investigate how orientation of the hcp iron carbide affects the diffraction pattern XRD was utilized again in Figure 4.4.5a. The disordered diffraction pattern results in a similar pattern to the simulated scan of the Fe_7C_3 standard. When the sample was aligned with the face of the hexagonal plate structures perpendicular to the sample holder the diffraction peak for the (102) increased to approximately double the normal 100 % peak for hcp Fe_7C_3. Therefore, it can be concluded the material under study has shape-induced texture. To get more insight on the crystallography of the hexagonal prism structures transmission electron microscopy with EELS diffraction was obtained shown in Figure 4.4.5b. The EELS diffraction shows a single crystal diffraction pattern, with d-spacing of 2.12 Å which is analogous to the (102) plane confirming the

intense diffraction plane on XRD is located on the face of the hcp crystal structure. Hexagonal crystal structures are uniaxial with its easy axis perpendicular to the face of the crystal structure therefore it can be inferred the <102> axis is the easy axis.

M-H curves with the samples easy axis aligned parallel and perpendicular to the external field are shown Figure 4.4.6. The single crystalline plates show obvious signs of magnetocrystalline anisotropy with a lower saturation field for the sample aligned parallel to the easy axis <102> as well as an increase in the Mr/Ms factor of 0.068 in comparison to 0.039. The sample aligned upon the easy axis also has a notable lower coercivity, which is observed in ferromagnetic plate structures were the longitudinal axis is perpendicular to the easy axis resulting in competition between shape and magnetocrystalline anisotropy.[114,115,116,117]

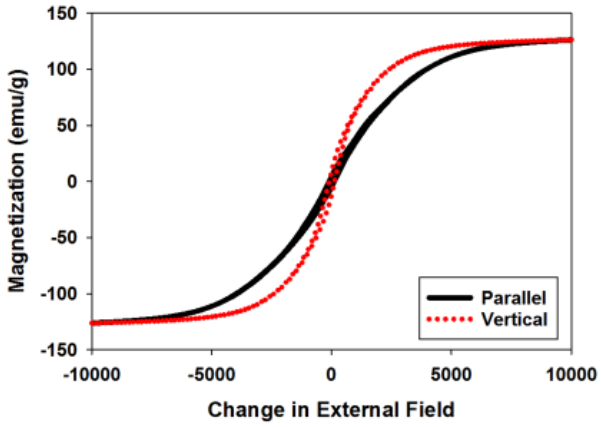

Figure 4.4.6. M-H curves for the samples long axis aligned parallel and vertical to the external field.

4.5 Thermal Stability of Fe_7C_3

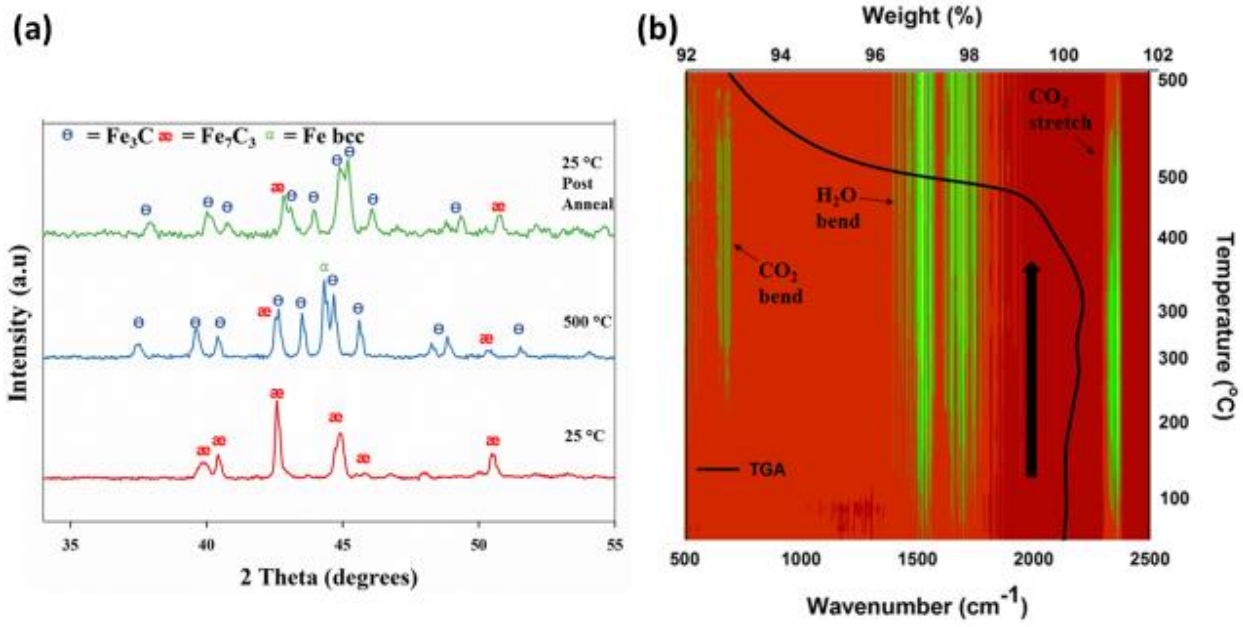

Figure 4.5.1. High temperature x-ray diffraction study of decomposition of Fe_7C_3 starting with 25 °C, 500 °C, and post-anneal (top of figure). (b) TGA-IR of Fe_7C_3 under 100 ml/min N_2 set to 500 °C.

The thermal stability of the Fe_7C_3 phase was measured under nitrogen gas via HT-XRD (Figure 4.5.1a). In this study the temperature was increased from room temperature to 500 °C at a ramp rate of 16 °C/min, followed by a 20 minute XRD scan, and lastly 31.7 °C/min cooling to room temperature. The results shown in Figure 4.5.1a illustrate that at 500 °C there was a mixture of Fe bcc, Fe_3C, and Fe_7C_3. According to the previous work of Fe_7C_3, the decomposition of Fe_7C_3 to Fe_3C occurred between 500 °C and 600 °C.[93,94] A TGA-IR (Figure 4.5.1b) plot of the decomposition of the Fe_7C_3 prisms showed weight loss at 500 °C which aligns with the HT-XRD phase change at 500 °C. A weight loss of 7.1% was observed which corresponds to the formation of CO_2 on the IR spectra. After cooldown, the Fe bcc peak disappeared, which illustrates the recovery of a mix phase of Fe_3C and Fe_7C_3 shown at 25 °C post annealed sample. Fe bcc has a

low carbon solubility, which upon cooling may reform carbide phase. However in recent works the Fe fcc phase with a higher solubility was needed to recover pure carbide.[97]

To confirm the change in the structure of the carbide upon cooling a second HTXRD study was performed (Figure 4.5.2). The XRD stage was heated to 500 °C at 16 °C/min followed by a 20 minute scan. A scan was completed upon cooling at 400, 300, 200 °C with a 50 °C/min cooling rate. Cooling to room temperature took approximately 10 °C/min followed by the last scan at room temperature. The results shown in Figure 4.5.2 reveal that at 500 °C, using Rietveld, there was 61.1% Fe_3C and 38.9 % Fe_7C_3. Upon cooling to 400 °C, 22.9 % of Fe bcc was formed which indicated that iron carbide decomposition occurred within the range from 500 to 400 °C. At 300 and 200 °C, magnetite was formed with a decrease in the metallic iron phase. At room temperature most of the Fe_7C_3 phase was recovered with a notable disappearance in oxide with 19.8 % Fe_3C and 80.4 % Fe_7C_3. An intermediate oxide phase upon reformation of carbide is unseen in literature. There have been past reports on Fe-C diagrams with compositions of Fe_3C and Fe_7C_3, however most are under non-ambient pressures.[94, 118] There is also a lack of Fe-C-O studies within the literature to fully comprehend this oxide transition.[119] However, recent studies on iron carbide systems have shown a Fe_3O_4 shell on bcc Fe is essential for iron carbide formation.[103]

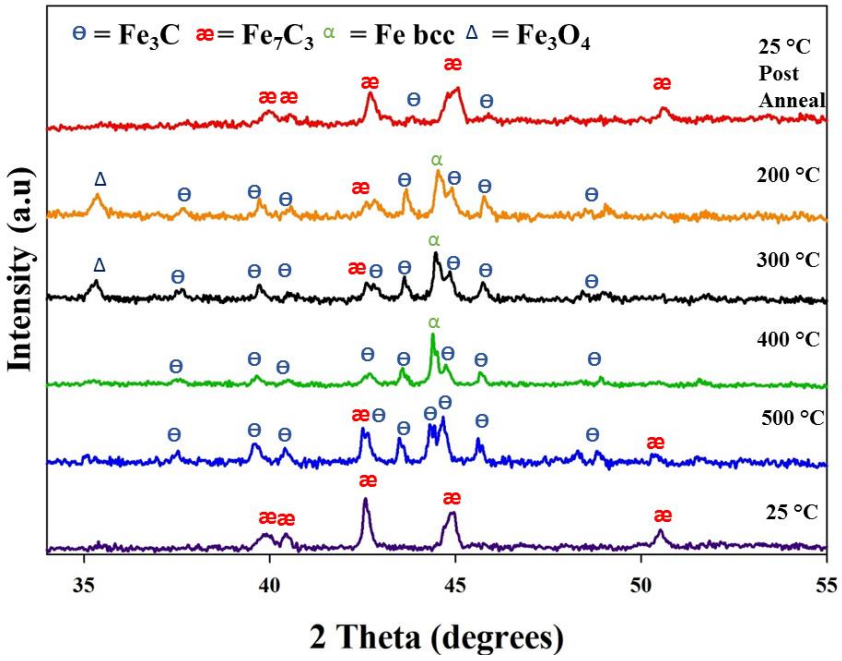

Figure 4.5.2. High temperature x-ray diffraction study of decomposition of Fe_7C_3 with 25 °C followed by 500 °C, 400 °C, 300 °C, 200 °C, and post-anneal.

Table 4.5.1. Energy dispersive x-ray spectroscopy of Fe_7C_3 before and after high temperature x-ray diffraction study.

EDX Quality	Fe_7C_3 Sample 1	HTK Study 1 Plate	HTK Study 1 Agg.	Fe_7C_3 Sample 2	HTK Study 2 Plate
Atomic C %	35.7	38.7	8.49	41.8	34.9
Atomic Fe %	52.8	50.1	51.1	49.4	55.4
Atomic N %	4.21	5.23	2.78	3.45	3.78
Atomic O %	7.30	5.93	37.6	5.31	5.92

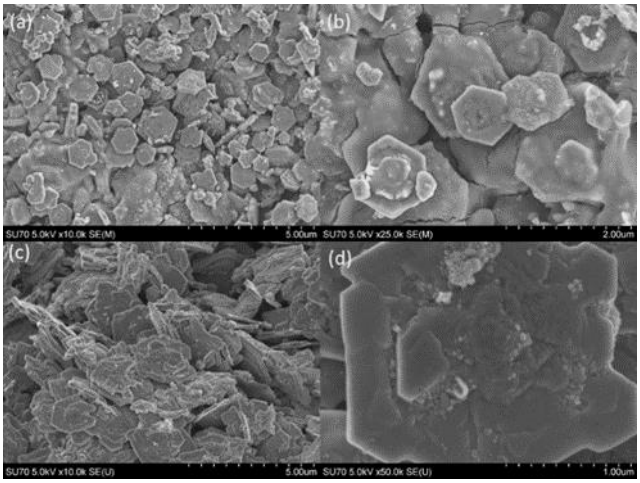

Figure 4.5.3. SEM image of Fe_7C_3 after HTXRD Study (a) and (b) of post-annealed samples with fast cooling represented in Figure 4.5.1 respectively. Image (c) and (d) are from the post-annealed sample but upon slow cooling represented in Figure 4.5.2 respectively.

SEM (Figure 4.5.3) and energy dispersive x-ray spectroscopy (EDS) (Table 4.5.1) analysis were conducted on the post annealed HT-XRD samples for insight on how annealing affected the composition and morphology of Fe_7C_3. Table II shows the atomic elemental percentage of each sample. The Fe_7C_3 hexagonal prisms pre-annealed for both studies show between 5-8% oxygen content, which indicates a minimal surface oxide presence. Figure 4.5.3 (a, b) are images which correspond with the fast quenching study from Figure 4.5.1. The micrographs depict sintered hexagonal prism structures. EDS point analysis was performed on the prisms and sintered material. The data for the quantitative EDS point analysis in Table II showed the prisms have similar elemental percentage to the original pre-annealed sample while the sintered material shows a 30.34 % increase in elemental oxygen. However, from Figure 4.5.1, no crystalline iron oxide is observed which concludes an amorphous iron oxide is present within this sample. The second HT-XRD study with a slow quenching process showed that the prisms retain their shape and elemental composition to the original sample in Figure 4.5.3(c, d). The increase in oxygen composition upon

fast cooling in comparison to slow cooling shows a correlation between losses of iron oxide with reformation of Fe_7C_3.

4.6 Conclusion

This work introduced detail on the role of the alkyl ammonium chloride in the synthesis of hexagonal prism Fe_7C_3 as well as determination of how the anisotropic structure effects its magnetic properties. Results show the structure of the prism and purity of the hcp phase is dependent on the length and structure of the alkyl ammonium group. Utilizing different boiling point solvents introduces a way to decrease the dimensions of the structures as low as 75 nm and it shows the synthesis can be accomplished at temperatures as low as 290 °C. The TEM diffraction pattern confirmed the face of the structure to be perpendicular to the <102> axis therefore enhanced magnetic properties were witnessed when the axis was aligned with the field. Thermal studies of the Fe_7C_3 hexagonal prisms confirmed a phase transition to Fe_3C with further decomposition to bcc Fe with longer annealing times from 400-500 °C. The recovery of Fe_7C_3 phase and morphology upon slow cooling shows the stability and high recovery of the material upon post annealing. Overall the texture shape induced magnetic properties can be utilized for spintronic applications while the high stability of these hexagonal prisms can be used as a radar absorbent materials and also shows the importance of Fe_3O_4 with forming carbide.

Chapter 5. Exchange bias and enhanced anisotropy from exchange coupled Fe_3C/CoO nanoaggregates

5.1 Overview/Motivation

A comparative magnetic study was conducted on Fe_3C and Fe_3C/CoO for potential enhancement in magnetic properties due to exchange interaction in ferro/antiferromagnetic systems. X-ray diffraction confirmed the presence of iron carbide and CoO while XPS determined presence of a $CoFe_2O4$ and a small percent of Fe_xCo_xC at the interface. Transmission electron microscopy showed a polydispersed network of 47 nm of Fe_3C coated with 17 nm CoO nanoparticles. Due to the intrinsic nature of the interface an enhanced coercivity above the blocking temperature (600 Oe) was observed in comparison to the bare Fe_3C nanoparticles (450 Oe). Upon cooling below the Néel temperature and Verwey temperature for CoO and $CoFe_2O4$ a maximum exchange bias of 150 Oe occurred at 50 K. Results have shown a plausible way to enhance the anisotropy of the iron carbide while broadening its potential applications for spin valve systems.

5.2 Introduction

In recent years extensive research has been conducted on enhancement of inexpensive, and abundant, rare-earth free magnets. Among these materials Co_xC and $CoFe_xC$ carbides have been studied extensively by our group and have shown great potential as a permanent magnet.[120,121,122] Unfortunately the cobalt carbide has a saturation of 50 emu g^{-1} which drastically lowers its BH_{max}. Alternatively iron carbide (Fe_3C) is known to have superior saturation values and has already been studied for applications such as contrast agents, drug delivery and hyperthermia. Unfortunately, iron carbide lacks the demagnetization field to compete with present day hard magnets .[123,80,40]

Bimetallic systems of ferromagnetic and antiferromagnetic materials have shown to enhance the coercive force of the system through unidirectional pinning of the ferromagnetic layer.[124,125,126] As well as enhancing the hardness of a material the pinning between the phase boundaries can cause a horizontal shift in the magnetic hysteresis known as exchange bias. These ferro/antiferromagnetic systems have applications in magnetic memory, magnetic sensing, and spin valve

systems.[127] Many studies have been done on bimetallic d-block systems of ferromagnetic Fe, Co, Fe_3O_4, and Co_2FeO_4 paired with CoO due to cobalt (II) oxides high magnetocrystalline anisotropy constant.[128,129,130] Systems of Fe_3O_4/CoO lead to large shifts in the hysteresis and enhanced hardness due to good interfacial agreement, however diffusion of metal centers occurs at the boundary.[131] Previous work with Fe/CoO systems have shown complete oxidation of metal iron drastically changing its properties over time.[132]

In this work we synthesize core/shell structure of iron carbide (Fe_3C) coated with CoO nanoparticles in order to enhance the unidirectional anisotropy of the Fe_3C material.[133] Unlike previous work iron carbide is much more resistant to oxidation in comparison to metallic iron.[134] Results have shown a potential route to increase the hardness of the iron carbide as well as explore its exchange bias properties at different temperatures.

5.3 Experimental

5.3.1 Synthesis of Fe_3C nanoparticles

Iron carbide was synthesized using a method used in a previous report.[133] 152 mg of iron carbonate, 2.2 mM CTAC, and 15 mL of oleylamine where added to three neck round bottom flask. The reaction was purged with nitrogen before the mixture was heated to 335 °C with a ramp

rate of 20 °C min^{-1}. The reaction was then heated to 365 °C at a rate of 1°C min^{-1}. After 10 minutes of reflux the reaction mixture was cooled. The sample was magnetically separated and washed with hexane and methanol, and placed in a vacuum oven.

5.3.2 Synthesis of Fe_3C/CoO nanoaggregates

15 mg of the iron carbide sample was added to 15 mL of oleylamine and 10 mL of 1-octadecene with 2.0 g of cobalt stearate. The reaction mixture was heated to 320 °C under nitrogen and kept at reflux for 30 minutes before cooling the reaction mixture, followed by washing and magnetic separation with hexane, and methanol.

2.4 Instrumentation

Crystal structure and phase analysis were done using a Panalytical X'Pert Pro MPD diffractometer under Cu Kα (λ = 1.5418 Å). Analysis of all XRD data was performed using X'Pert HighScore Plus software, which was used to determine percent phase composition and Scherrer analysis. Rietveld analysis was used in Highscore, using lattice parameters from Pearsons Handbook of Lattice Spacings and Structures of Metals.[101] Transmission electron microscopy and EELS mapping for all products were carried out using a Zeiss Libra 120. Energy dispersive x-ray spectroscopy (EDS) was conducted on the Hitachi SU-70 in order to gain the elemental composition of the material under study. X-ray photoelectron spectroscopy data was collected in the ThermoFischer EXCAlab to assist in identification of phase composition at the interface. Magnetic characterization was performed using a Quantum Design Versalab Vibrating Sample Magnetometer (VSM).

5.4 Results and discussion

Crystal phase structures were determined using a PANalytical X'Pert Pro MPD diffractometer under Cu Kα (λ = 1.5418 Å) shown in Figure 5.4.1. The presence of pure orthorhombic Fe_3C phase was confirmed in Figure 1b with lattice parameters a = 5.043 Å, b = 6.793 Å, and c = 4.540 Å which were in good agreement with the standard Fe_3C pattern shown in Figure 1c and less than 1% deviation from other Fe_3C lattice constants.[101] The diffraction pattern obtained after the synthesis with cobalt stearate in Figure 1a had a composition indicative of 87.2% Fe_3C and 12.8% cubic CoO.[101] Despite the similarity in the lattice parameter of 4.267 Å of CoO to other sources, the parameters for Fe_3C where shifted in comparison to the original sample (a = 5.004, b = 6.846, c = 4.541). A previous report by Razumovskiy et al. through theoretical calculations demonstrated cobalt doped Fe_3C resulted in a decrease in lattice parameters with increase doping of cobalt.[135] Lattice strain from the large lattice mismatch between iron carbide and cobalt (II) oxide is another potential reason for distortion in the lattice structure.[136] The Scherrer analysis of the broadened diffraction peaks of the Fe_3C and CoO phases confirm the formation of small nanocrystallite sizes of 17.1 nm and 15.4 nm respectively.

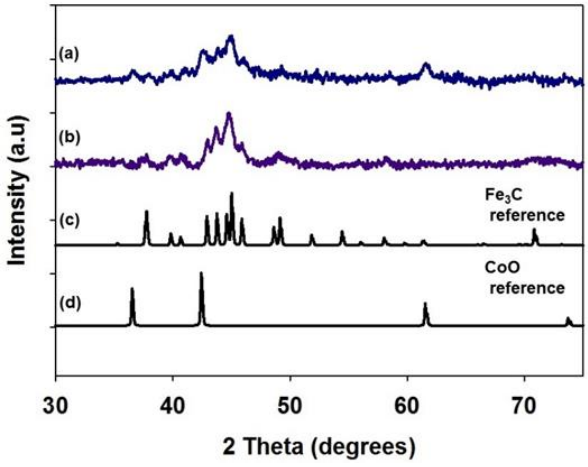

Figure 5.4.1. X-ray diffraction of the (a) Fe_3C/CoO and (b) Fe_3C sample as well as the reference patterns for (c) Fe_3C (PDF 01-089-2722) and (d) CoO (PDF 01-089-7099).

The structure of the sample before and after addition of cobalt oxide was studied using the ZEISS Libra 120 TEM shown in Figure 5.4.2. Figure 5.4.2a shows an agglomeration of Fe_3C nanoparticles with an average size of 47 nm. A thin 5 nm layer is present on the surface which has been confirmed to be amorphous carbon through the use of Raman spectroscopy (Figure 5.4.3) and is commonly found on the surface of carbide nanomaterials.[112,28] After treatment with cobalt stearate, Figure 5.4.2b and c shows the iron carbide coated with 17 nm elliptical shaped nanoparticles. EELs mapping in Figure 5.4.2d confirmed the 17 nm particles to be cobalt rich with a nonhomogeneous coating on the iron rich areas of the Fe_3C. Presence of CoO on the surface of the iron carbide would favor anti/ferromagnetic coupling at the interface.

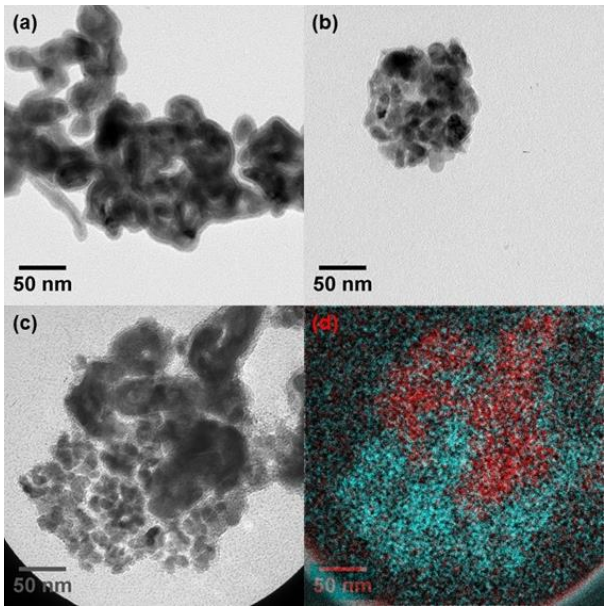

Figure 5.4.2 Transmission electron microscope images of (a) Fe_3C, (b) Fe_3C/CoO. EELs mapping was done on Fe_3C/CoO were (c) shows the sample under regular imaging, (d) shows mapping were the red denotes iron and cyan denotes cobalt.

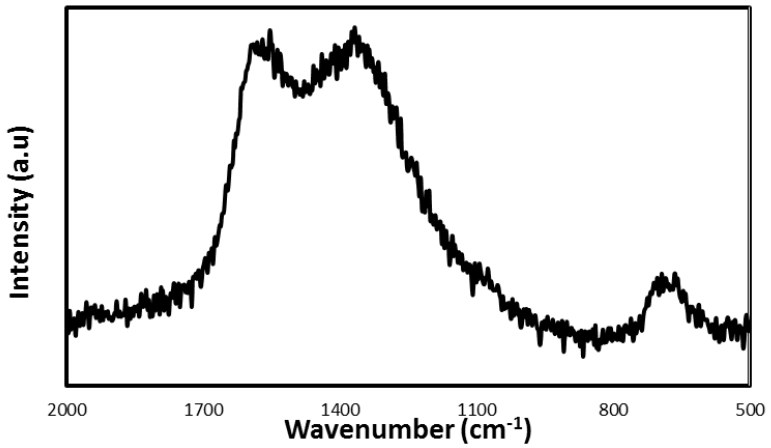

Figure 5.4.3 Raman spectra of Fe_3C sample which shows the graphite band (1580 cm^{-1}) and disorder band (1350 cm^{-1}).

X-ray photoelectron spectroscopy (XPS) was carried out with the Thermofischer ESCAlab for further analysis of the surface composition of the Fe_3C/CoO in Figure 5.4.4 The Co 2p spectra with photoemissions located at 780.83 eV for Co $2p_{3/2}$ and 796.95 eV for Co $2p_{1/2}$, as well as highly intense satellite peaks at 786.29 eV, and 803.25 eV are indicative of the presence of Co^{2+}.[137] A small shoulder is present at 778.3 eV which has previously been reported as cobalt carbide.[138] The Fe 2p spectra shows presence of Fe^{3+} undetected by XRD with binding energies of 712.61 eV for Fe $2p_{3/2}$ and 724.39 eV for Fe $2p_{½}$ as well as peaks at 707.23 eV and 718.54 eV which match previous reports of iron carbide.[139] The Co 2p spectra further confirms the presence of CoO while the Fe 2p spectra shows that oxidation of iron carbide may be taken place at the surface. At particle-particle interfaces it is likely that some diffusion of atoms may occur, therefore it is likely with the presence of Fe^{3+} and Co^{2+} a $CoFe_2O_4$ alloy is forming at the interface.[140,141] Also the small amount of cobalt carbide found within the sample helps validate a small amount of Fe_xCo_xC alloying occurs as at the interface. Fe^{2+} may be present within the material, however it is difficult to confirm with the strong presence of Fe^{3+}.

Table 5.4.1 Energy dispersive spectroscopy elemental analysis of the Fe_3C sample and the Fe_3C/CoO.

	Atomic % in Fe3C	**Atomic % in Fe3C/CoO**
Fe	**39.69**	**25.18**
Co	**---**	**22.61**
C	**47.17**	**38.76**
O	**13.13**	**13.45**

Percent atomic composition was determined from the survey spectrum in Figure 5.4.5 which gives a low atomic percentage of iron of 3.05% in comparison to 25.18% on EDS (Table 5.4.1) which can be contributed to surface coverage of the iron carbide with the CoO structure. Most of the surface composes of oxygen and carbon with the corresponding O 1s and C 1s spectra in Figure 5.4.6 The oxygen spectra shows presence of metal to oxygen bonds as well as a strong peak at 531.6 eV which represents adsorbed oxygen species.[142] The C 1s spectra showed presence of species expected for oleylamine and stearate with aliphatic carbon at 284.8 eV, C-O and C-N, at 286.2 eV, C=N at 287.07 eV, and C=O located at 288.92 eV.[139,143] Imine previously has been said to occur from the reduction of 3d metals with aliphatic amines.[28,63,69]

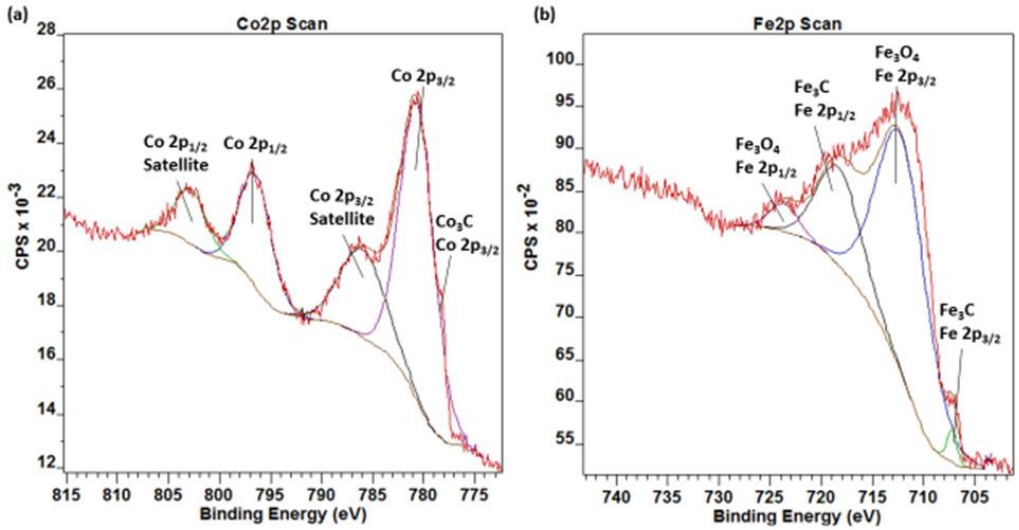

Figure 5.4.4 XPS 2p spectra of (a) cobalt and (b) iron from the Fe_3C/CoO sample.

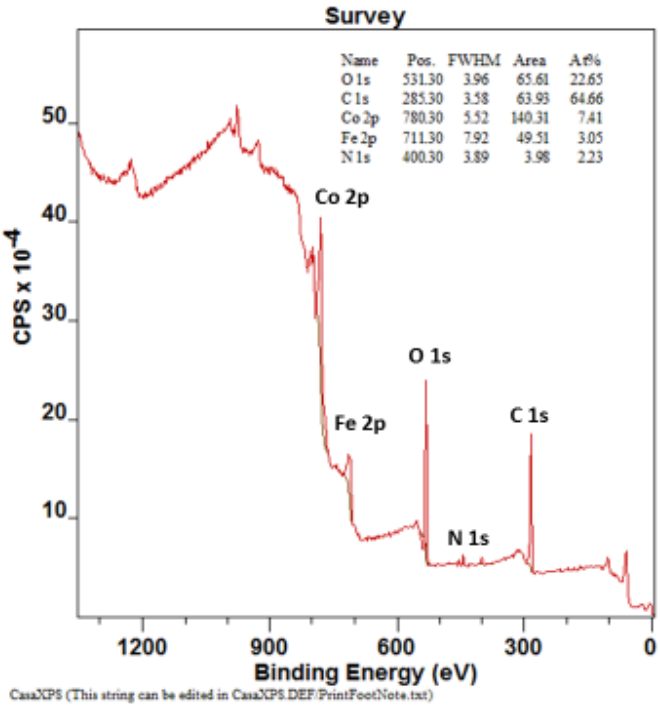

Figure 5.4.5 XPS Survey scan of Fe_3C/CoO material with a table of the atomic percentages.

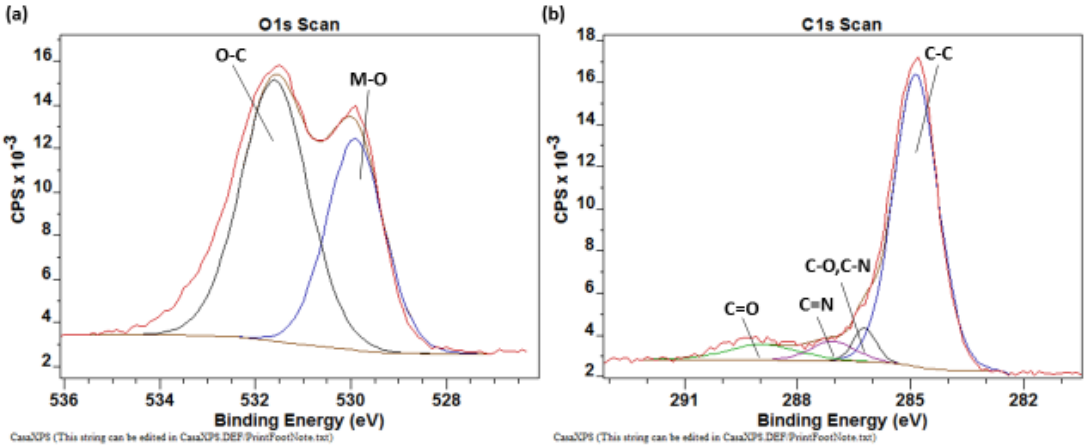

Figure 5.4.6 (a) O1s, and (b) C1s XPS spectra for Fe_3C/CoO sample.

The Quantum Design Versalab Vibrating Sample Magnetometer (VSM) was utilized to obtain room temperature M-H curves for the Fe_3C and the Fe_3C/CoO system illustrated in Figure 5.4.7 Both curves show the nanoparticles are ferromagnetic at room temperature. The saturation values depress slightly from 87 emu/g to 81 emu/g due to the dilution of saturation from the CoO phase. The coercive force is enhanced from 450 to 600 Oe due to exchange interaction between the interface of the iron carbide and cobalt oxide layer which causes an enhanced demagnetization field. This enhancement of coercivity above the Néel temperature has been identified in exchange bias systems. However most ferro/antiferromagnetic systems need to be field cooled initially to enhance the coupling at the interface.[144,145] A previous report has shown the alloy layer formed

between the ferro and antiferromagnetic layer may contribute to the enhancement at room temperature similar to exchange interaction within a spring magnet.[146,147,148] Therefore it can be concluded the enhancement in the Fe_3C/CoO material may be due to the ferrimagnetic $CoFe_2O_4$ layer detected by XPS.

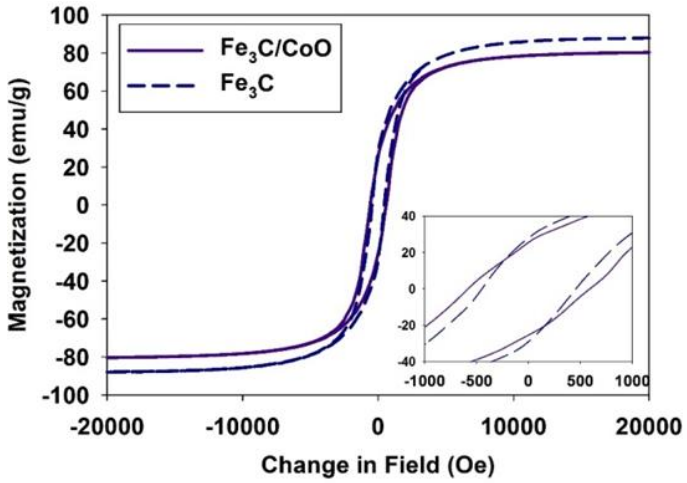

Figure 5.4.7 M-H curves at 300 K for iron carbide before coating (solid line) and after coating (dashed line) with CoO.

To properly analyze how interfacial interactions effect the magnetic properties of the Fe_3C/CoO system, a field cooled (FC) and zero-field cooled (ZFC) curve with a 500 Oe applied field, as well as M-H curves ranging from 50-300 K were obtained, shown in Figure 5.4.8a and b. The ZFC in Figure 5.4.8a shows a broad curve which is attributed to the wide size distribution within the sample. In the inset of Figure 5.4.8a the first derivative of susceptibility was taken which shows a peak at 276 K and 150 K. The peak at 276 K is observed due to the Néel transition (T_N) of CoO within the sample. The peak at 150 K is known as the first order Verwey transition[10] (T_V) which shows the change from an ordered monoclinic to disordered spinel structure of $CoFe_2O_4$.[149,150,151]

The presence of this transition concludes some oxidation occurs at the surface of iron carbide. Previous work has shown cobalt carboxylate groups are known to release the oxidizing agent CO_2 upon decomposition to cobalt oxides.[97] This transition has a clear effect on the magnetics upon cooling as seen from Figure 3.8b with a drop in coercivity and an increase in exchange bias upon cooling below 150 K.

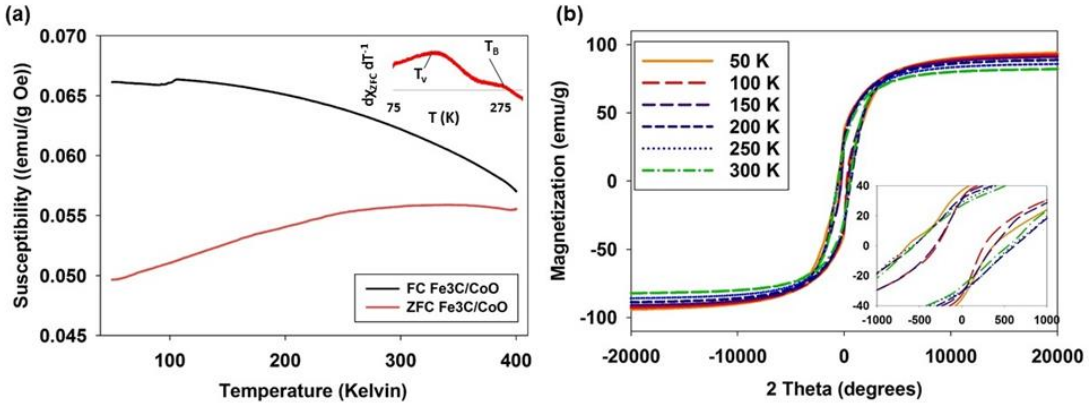

Figure 5.4.8 (a) M-T curves of corresponding Fe_3C/CoO sample with a sweep rate of 5 K min^{-1}. (b) M-H curves taken from 50-300 K for Fe_3C/CoO sample.

Figure 5.4.9a and b shows the corresponding exchange bias and coercivities at different temperatures for Fe_3C and Fe_3C/CoO. The exchange bias for the Fe_3C versus the Fe_3C/CoO shows drastic change. The uncoated sample shows minuet shifts in the hysteresis which is to be expected from absence of an antiferromagnetic phase. The coated sample shows a shift to positive field of 20 Oe going from 300 to 150 K with a sudden change back to negative bias at 100 K. The positive exchange bias has been witnessed in previous work and was said to be contributed from the

blocking temperature of CoO which occurs below 200 K.[152,128b] The increase in negative exchange bias below 150 K is due to the ordering of the $CoFe_2O_4$ lattice structure which allows for exchange coupling through the cobalt ferrite interface. This change in ordering and crystal structure from cubic to monoclinic is said to reduce symmetry of the structure thus increasing magnetocrystalline anisotropy.[149] The strong exchange interaction below T_B and T_V are due to an increase in unidirectional anisotropy.

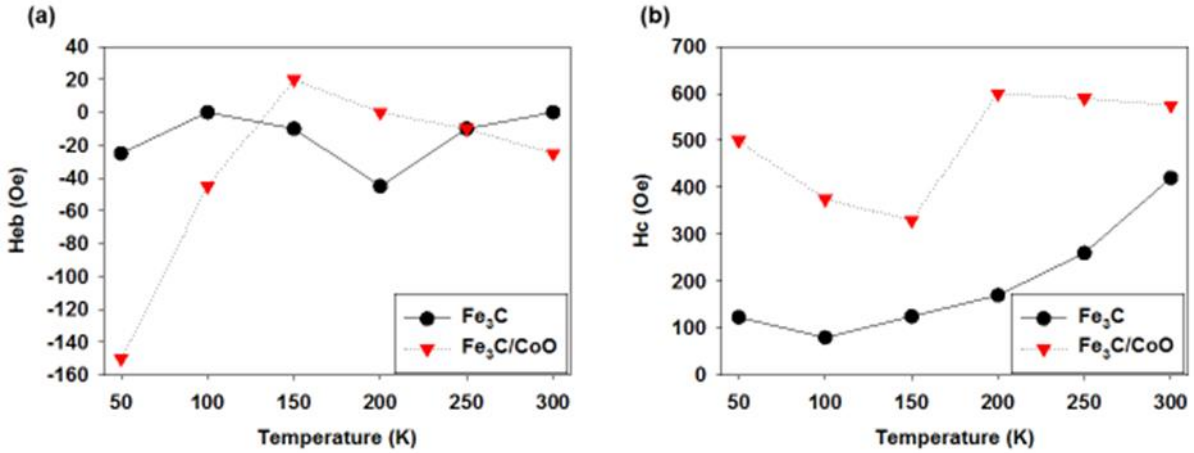

Figure 5.4.9 (a) Exchange bias field and (b) coercive force taken at temperatures ranging from 50-300 K without an external field.

As seen from Figure 5.4.9b. cobalt (II) oxide structure also had a great impact on the coercivity. The bare Fe_3C sample shows a decrease in coercivity with a decrease in temperature. This is most likely due to the fact that there is a soft phase such as some Fe_3O_4 impurity within the sample. EDS analysis from Table 5.4.1 shows the 13% of the atomic percentage is oxygen which may be due to iron oxides. The coated sample as discussed earlier starts off with an enhanced coercive force which doesn't drastically change until the coercivity decreased from 600 to 330 Oe from 200 to 150 K. Similar to the variation in exchange bias this drop is due to the ordering of the CoO layer under T_B. The randomized spins are influenced more from an external field than an ordered

antiferromagnetic system. Below 150 K an increase in coercivity is observed up to 500 Oe at 50 K due to the pinning of the free electrons of the iron carbide with the oxide layer at the interface occurring below T_B and T_V.

5.5 Conclusion

This work introduces a novel synthesis of iron carbide coated with an antiferromagnetic cobalt oxide layer (Fe_3C/CoO). Fe_3C/CoO has shown to be a promising route in enhancing its magnetic properties. The intrinsic interfacial layer consisting of cobalt ferrite and enhanced the room temperature demagnetization field. Upon cooling below T_B and T_V for CoO and $CoFe_2O_4$ negative bias was observed with a maximum of 150 Oe at 50 K. Therefore using CoO seems to be a feasible route to enhance unidirectional anisotropy of Fe_3C and broaden its potential for more applications such as spin valve technology.

Chapter 6. Spring exchange coupled $Fe_7C_3/SrFe_{12}O_{19}$

6.0 Overview/Motivation

Chapter 5 explored the use of exchange bias to enhance the coercivity of iron carbide at room temperature. A successful increase in coercivity was observed, which was believed to be attributed from the spring magnet exchange interaction between iron carbide and cobalt ferrite formed at the interface. Therefore, Chapter 6 will focus on the development of an iron carbide/strontium ferrite spring magnet. A time study was achieved in an attempt to find an optimum phase percentage of carbide to ferrite for maximum enhancement. Optimum magnetic properties were witnessed with 23.9% Fe_7C_3 and 76.1% strontium ferrite with an M_s of 67 emu g^{-1} and H_c of 1040 Oe.

6.1 Introduction

Permanent magnets are classified as hard magnetic materials with the main purpose of generating flux for applications such as electric motors, turbines, and hard drives.[3] The field of permanent magnets have been dominated by NdFeB due to its high magnetocrystalline anisotropy, and low price in comparison to other rare-earth magnets as discussed in Chapter 1.[20] Since the discovery of neodymium magnets in 1984 there has not been a huge discovery of a new material with enhanced permanent magnet properties.[20,21] However, with the revolution in nanomaterials research spring exchange magnets which are composed of exchange coupled hard and soft phases have been employed in an attempt to increase the magnetic properties of present day magnetic materials including neodymium, and samarium cobalt materials.[2] Despite the benefits of further developing rare-earth magnets it would be beneficial to replace rare-earth materials with less expensive nanocomposites.

There have been developments in research over 3d metal/metal oxide exchange spring magnets to replace rare-earth materials.[8,153,154,155] Barium and strontium ferrites are extremely attractive materials, due to their inexpensive elemental composition, with decent magnetic properties.

Besides neodymium magnets strontium ferrite constitutes a good percentage of the permanent magnet industry with applications in loudspeakers, blower motors, and windscreen wiper motors.[17] Despite the relevance of this material in industry it is limited due to its ferromagnetic crystal structure with two sublattices oriented in opposite directions which hinders its M_s and M_r. Recently magnetite with a bulk magnetic saturation of 95 emu g^{-1} was used to enhance the properties of $SrFe_{12}O_{19}$ with a 42%, 29%, and 27% increase in M_s, M_r, and H_c respectively.[156,157] Iron carbide is known to have greater saturation values than iron oxide (140 emu g^{-1} bulk)[11] which may be beneficial for further enhancing the magnetic properties of the hexagonal ferrites. Moreover, the Fe_3C/CoO nanoaggregates in the previous chapter found enhanced H_c at room temperature, which is believed to be attributed to a cobalt ferrite phase formed at the interface. Iron carbide and strontium ferrite nanocomposites may benefit from the high saturation of the carbide with the large demagnetization field of the ferrite, to produce a relative inexpensive permanent magnet.

Within this chapter a strontium ferrite will be partially reduced to hexagonal Fe_7C_3 using the synthesis methods observed in Chapter 4. Since iron oxide was found to be an intermediate phase upon synthesis of Fe_7C_3 starting with strontium ferrite was determined to be sufficient for a starting material for carbide formation. The reaction will take place in oleylamine which will act as a reduction and carbon source.[112] Phase percentage as a function of reaction time was observed to optimize the percentage of carbide needed to enhance the saturation and remanence with minimum depletion of coercivity. A schematic of the reaction in oleylamine is shown in Figure 6.1.1.

Figure 6.1.1 Diagram depicting the effect of time on dominant species after reduction.

6.2 Experimental

6.2.1 Sonochemical synthesis of $SrFe_{12}O_{19}$ particles

$SrFe_{12}O_{19}$ particles were synthesized as previously done by Nabiyouni et al.[93] Strontium carbonate (1 mmol), iron nitrate (12 mmol), and CTAB (1.37 mmol) were dissolved in deionized water (100 mL). Sodium hydroxide (50 mL, 1 M) was added dropwise over 30 minutes, during which the solution was continually sonicated (80 W). The resulting red-brown precipitate was separated by vacuum filtration and left to dry on the apparatus for approximately 2 hrs. Following the drying process, the solid was then annealed for 4 hours at 1000 °C in air, with a ramp rate of 70 °C·min^{-1}. The final product was cooled to room temperature and washed 3 consecutive times with methanol before drying in a vacuum oven for 24 hrs.

6.2.2 Partial reduction of $SrFe_{12}O_{19}$ particles

The $SrFe_{12}O_{19}/Fe_7C_3$ system was produced by iron carbide synthesis methods for hexagonal Fe_7C_3 used in Chapter 1&2.[133] The $SrFe_{12}O_{19}$ particles (0.025 g) were submerged in a solvent system composed of oleylamine (15 mL) and CTAC (mM). The system was magnetically stirred under inert gas (N_2) for 5 minutes before heating to reflux at 360 ^oC for 10 minutes. The resulting product was washed first with hexane and magnetically separated using a neodymium magnet; the product was then washed with methanol before final magnetic separation. The product was left to dry in a vacuum oven for 30 minutes.

6.2.3 Instrumentation

Crystal structure and phase analysis were done using a Panalytical X'Pert Pro MPD diffractometer under Cu Kα (λ = 1.5418 Å). Analysis of all XRD data was performed using X'Pert HighScore Plus software, which was used to determine percent phase composition and Scherrer analysis. Scanning electron microscopy was performed on the Hitachi SU-70. Magnetic characterization was performed using a Quantum Design Versalab Vibrating Sample Magnetometer (VSM).

6.3 Results and Discussion

6.3.1 Partial Reduction of $SrFe_{12}O_{19}$

X-ray diffraction was utilized to determine the composition of the products following reduction of strontium ferrite in oleylamine observed in Figure 6.3.1.1. The strontium ferrite used for the synthesis of the nanocomposites in Figure 6.3.1.1c coincides with the reference strontium ferrite pattern in Figure 6.3.1.1d with a crystallite size of 72.25 nm determined by Scherrer analysis. Upon reduction of strontium ferrite, the majority phase of hexagonal Fe_7C_3 with a 23.85 nm

crystallite size was present, with a minor phase of strontium ferrite. Further increasing the reflux time to 20 minutes results in further conversion to iron carbide with a crystallite size of 26.5 nm with strontium ferrite scarcely present within the noise of the diffraction pattern. Results show the crystallite size for iron carbide increased with longer annealing due to Ostwald ripening. The Scherrer analysis for strontium ferrite was inconclusive for the strontium ferrite present post reduction at 20 minutes at reflux due to low crystalline peaks observed within the diffraction pattern.

Rietveld analysis was done using the starting lattice parameters from Pattanayak et al. and Fang et al. to determine the crystal phase composition and lattice parameters.[39,158] The strontium ferrite seed was found to have lattice parameters within good agreement with literature values with a = 5.883 Å, and c = 23.07 Å. With increase in synthesis time the iron carbide percentage increased from 76% to 82.2% with a decrease in ferrite composition. While the lattice parameter for strontium ferrite were in good agreement with literature values for both samples, the lattice parameters for hcp iron carbide shifted from a = 6.889 Å, c = 4.536 Å at 10 minutes at reflux to a = 6.84653 and c = 4.5006 Å at 20 minutes. Doping of Sr^{3+} cations into the lattice structure of iron carbide should result in an increase in lattice parameters which is not the case.[159] Therefore, it can be concluded the decrease in lattice parameters is due to mechanical stress from the mismatched lattices of strontium ferrite and hcp iron carbide.

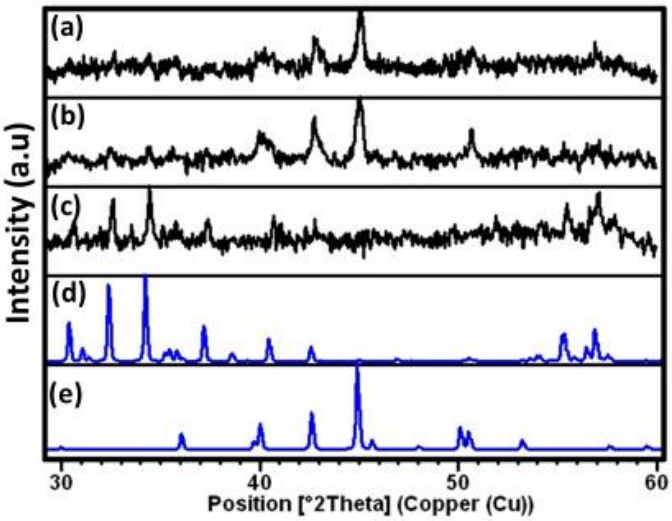

Figure 6.3.1.1 X-ray diffraction of $SrFe_{12}O_{19}/Fe_7C_3$ nanocomposites. (a) $SrFe_{12}O_{19}/Fe_7C_3$ at reflux for 10 minutes. (b) $SrFe_{12}O_{19}/Fe_7C_3$ reaction at reflux for 20 minutes. (c) Strontium ferrite seeds synthesized at 1000 C in air. (d) Strontium ferrite and (e) Fe_7C_3 reference patterns.

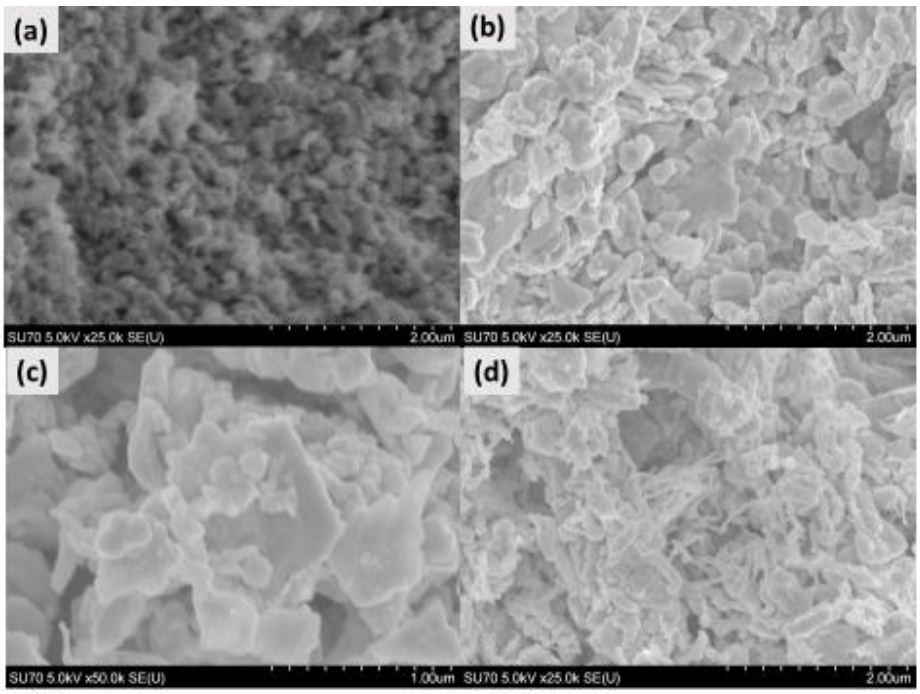

Figure 6.3.1.2 Scanning electron micrographs of (a) strontium ferrite post annealing, (b) $SrFe_{12}O_{19}/Fe_7C_3$ 10 minutes at reflux, and (c) $SrFe_{12}O_{19}/Fe_7C_3$ 20 minutes at reflux.

To determine the effect of oleylamine reduction on the physical dimensions of the composites, scanning electron microscopy was completed (Figure 6.3.1.2). Before reduction the polydispersed strontium ferrite grains are roughly larger than 100 nm which is similar to the lower size approximation for crystallite size given by XRD. Upon reduction in oleylamine the composite structures dimensions increased ranging from 100 nm to 400 nm at both 10 and 20 minutes at reflux ((Figure 6.3.1.2(b-d))) , which shows reduction at 360 °C some coalescence occurs at reflux. Some grains of the $Fe_7C_3/SrFe_{12}O_{19}$ material contain a hexagonal structure which is analogous to its crystal structure observed in Figure 6.3.1.2c.

M-H curves were utilized to analyze the room temperature magnetic properties of the composites in Figure 6.3.1.3 while Table 6.3.1.1 displays the magnetic values for the samples. The strontium ferrite had a saturation of 53.62 emu g^{-1}, a magnetic remanence of 20.8 emu g^{-1}, and a coercivity of 1625 Oe. Higher coercivity values can be achieved in anisotropic aligned grain structures.[160] By reducing the strontium ferrite to majority hexagonal Fe_7C_3 phase the saturation increased up to 86.99 emu g^{-1} with a small decrease in remanence, but a drastic decrease in coercivity. This is not surprising sense the submicron hexagonal prism Fe_7C_3 prepared in Chapter 3 and 4 is considered magnetically soft. However, the presence of a small percentage of strontium ferrite was capable increasing the coercivity to 660 Oe at 10 minutes at reflux, greater than the Fe_3C/CoO nanoaggregates. By fine tuning the percentage of ferrite to carbide there may be a chance to further enhance the composites magnetic properties.

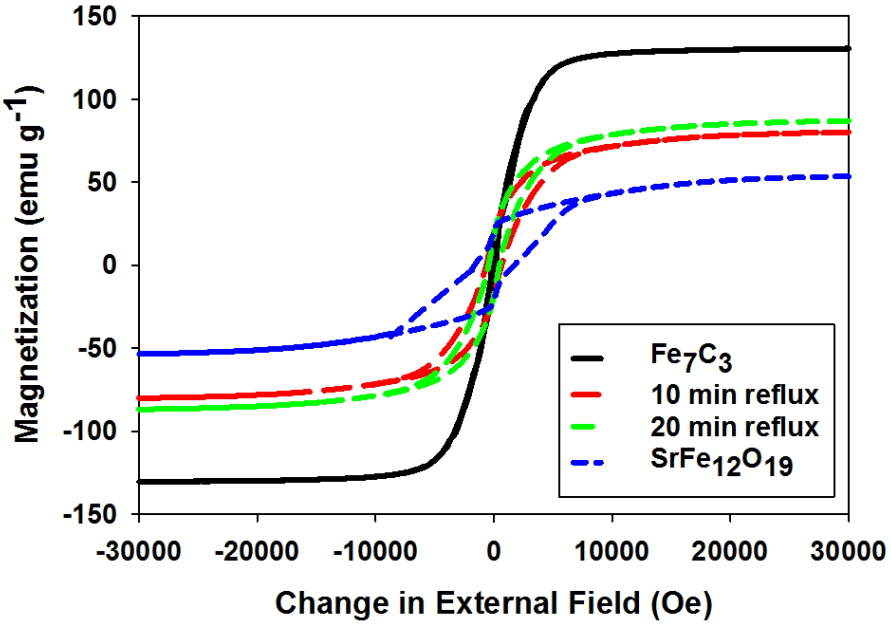

Figure 6.3.1.3 Room temperature M-H curves for strontium ferrite synthesized at 1000 °C, strontium ferrite/iron carbide composites synthesized at 10 and 20 minutes at reflux, and Fe_7C_3 reference.

Table 6.3.1.1 Magnetic values from M-H curve observed in Figure 6.3.1.3.

	Phase Composition Fe_7C_3 (%)	M_s (emu g^{-1})	M_r (emu g^{-1})	H_c (Oe)
$SrFe_{12}O_{19}$	---	53.62	20.8	1625
$SrFe_{12}O_{19}/Fe_7C_3$ 10 min reflux	76	80.20	19.00	660
$SrFe_{12}O_{19}/Fe_7C_3$ 20 min reflux	82.2	86.99	17.8	475
Fe_7C3	100	130.49	6.4	125

6.3.2 Time Study

In order to receive the optimum magnet properties between the hard/semi-soft systems a time study was done under the same reaction conditions, with the exception that mechanical stirring was used for simpler extraction of the product from solution. Aliquots were taken from 345 °C to reflux at 360 °C followed by extractions at 30 and 60 minutes at reflux. The diffraction pattern observed in Figure 6.3.2.1 was applied to determine the percent composition of strontium ferrite and iron carbide in Table 6.3.2.1 as the reaction proceeds. As time proceeds the hexagonal carbide phase increased from 9.7% at 345 °C, 16.9% at reflux, and 23.9% at 60 minutes at reflux. The slower conversion in comparison to the reactions performed under magnetic stirring pertains to the mixing rate as the mechanical stirring did minimum mixing of the strontium ferrite product within the medium. The percent composition for aliquots taken at 355 °C and 365 °C were inconclusive due to the high noise within the diffraction pattern. This may be attributed to times were there was major conversion of ferrite to carbide which would result in high diffusion and adsorption rates of oxygen and carbon as well as crystal plane reorientation. The lattice parameters determined by Rietveld showed a decrease in the Fe_7C_3 lattice parameters from a = 6.913 Å , c = 4.508 Å at 345 °C to a = 6.86846 Å, c = 4.519 Å at 60 minutes. Like stated previously this can be attributed to lattice strain from the strontium ferrite lattice structure, however in this instance the lattice parameter error was minimal (<.5%).

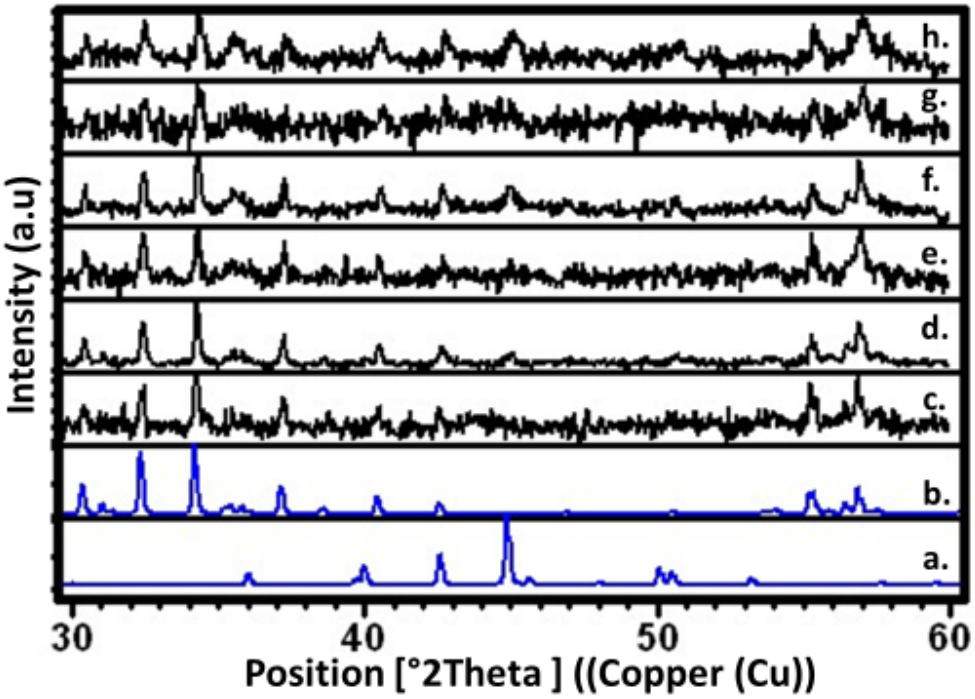

Figure 6.3.2.1 X-ray diffraction of aliquots from strontium ferrite reduction in oleylamine taken at (c) 335 °C, (d) 345 °C, (e) 355 °C, (f) 360 °C, (g) 360 °C 30 min, (h) 360 °C 60 min with (a) hexagonal Fe_7C_3 and (b) $SrFe_{12}O_{19}$ reference pattern.

Table 6.3.2.1 Crystal phase percentage of diffraction patterns from time study, calculated from Rietveld refinement.

Temperature	$SrFe_{12}O_{19}$ (%)	Fe_7C_3 (%)
335 °C	100	0
345 °C	90.3	9.7
355 °C	---	---
360 °C	83.1	16.9
360 °C 30 min	---	---
360 °C 60 min	76.1	23.9

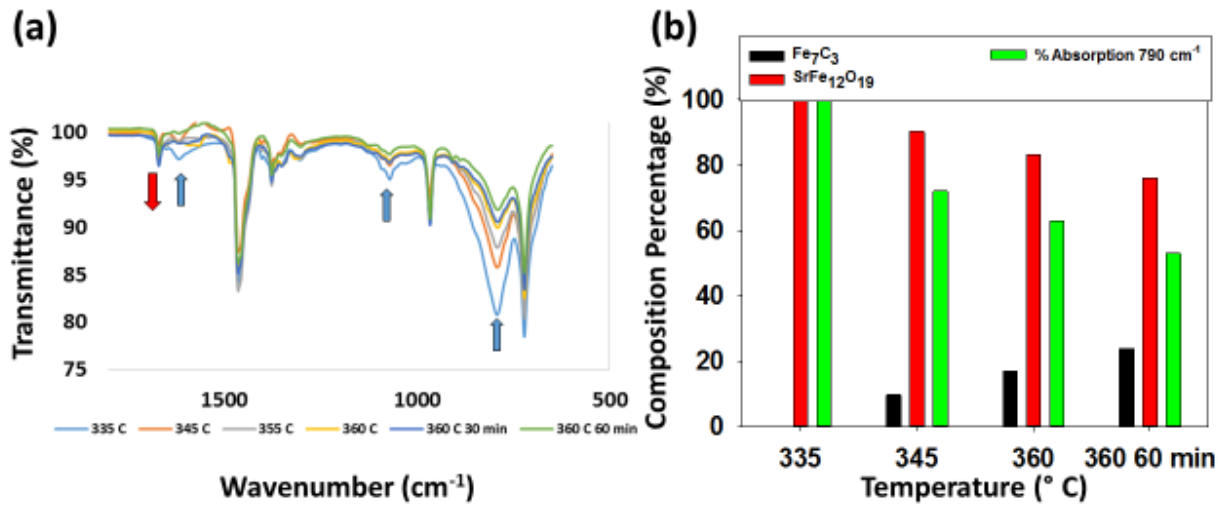

Figure 6.3.3.2 (a) FT-IR of aliquots taken from ferrite reduction. (b) Bar graph of percent composition of aliquots taken over a temperature range of strontium ferrite and iron carbide calculated from x-ray diffraction and normalized N-H stretch at 790 cm^{-1}.

FT-IR spectra in Figure 6.3.3.2a were obtained from the aliquots taken from the time study. Results show formation of C=N stretch observed at 1670 cm^{-1} with loss of the NH_2 scissoring and N-H bend observed at 1620 cm^{-1}, and 790 cm^{-1} which confirms oleylamine still acts as a reduction source for carbide formation within this system. Figure 6.3.3.2b shows the percent phase composition of the products, with consumption of N-H due to reduction of Fe^{3+} to Fe^{0}. It can be observed that the depletion of strontium ferrite correlates to the loss of the N-H bend on FT-IR where they both decrease at a slower rate over time.

Exchanging magnetic stirring for mechanical stirring caused a drastic change in the phase composition and within the final product. Previous reports on stir rates on reaction conditions have shown drastic effects on the kinetics of the system with change in growth rates, particle size,

and morphology control.[161,162,163] Previous mechanistic studies on carbide formation stated that iron oxide acts as a catalyst for carbon cleavage and oxidation of aliphatic amines.[112] In conclusion slow agitation of the mixture leads to low interaction between the ferrite catalyst and oleylamine (reduction and carbon source). Low interaction between the precursor and solvent results in initial inhomogeneous carbide formation and an overall lower carbide percentage formed.

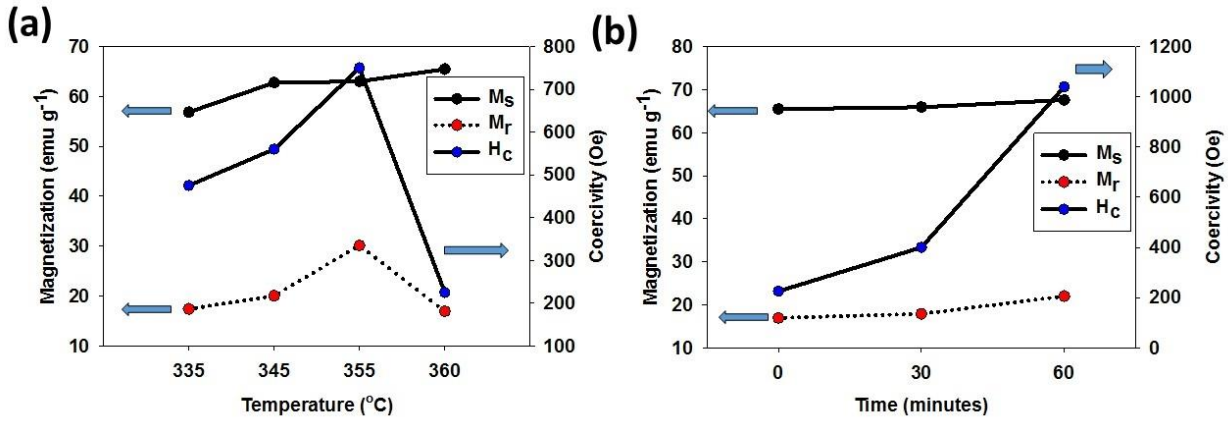

Figure 6.3.3.3 (a) Magnetization (left axis) and coercivity (right axis) versus temperature for samples taken at 335, 345, 355, and 360 °C. (b) Magnetization (left axis) and coercivity (right axis) versus time for samples taken at reflux at time 0, 30, and 60 minutes.

In order to determine the optimum conditions for spring exchange coupling, M-H curves were obtained for each aliquot. Figure 6.3.3.3 shows the saturation, remanence and coercivity values for each sample. A gradual increase in saturation value was witnessed with an increase in temperature due to the higher percentage carbide formation over time. The remanence and coercivity show very similar patterns by increasing up to 335 °C with both values dropping once the reflux temperature was reached. The drop in remanence and demagnetization field can be attributed to an inhomogeneous reduction of carbide at reflux conditions. Once reflux is reached all magnetic properties increase over time from M_s = 65.49 emu g^{-1}, M_r = 16.95 emu g^{-1} H_c = 225 Oe at time zero at reflux, to M_s = 67.62 emu g^{-1}, M_r = 22 emu g^{-1}, and H_c = 1040 Oe at 60 minutes

at reflux. The final product of this reaction resulted in saturation and remanence values higher than the starting material with a coercivity above the threshold for a permanent magnet. This affect may be due to the increase coupling between interstitial sites of the hard and soft phases. The M-H curves can be observed in Figure 3.3.4 from time zero to 60 minutes at reflux, with the original strontium ferrite specimen for comparison. A duck shape is observed in the curves at time zero and 30 minutes which is normally observed in decoupled soft and hard magnetic phases. Over time this duck shape decreases due to the increase spring exchange in the $Fe_7C_3/SrFe_{12}O_{19}$ system.

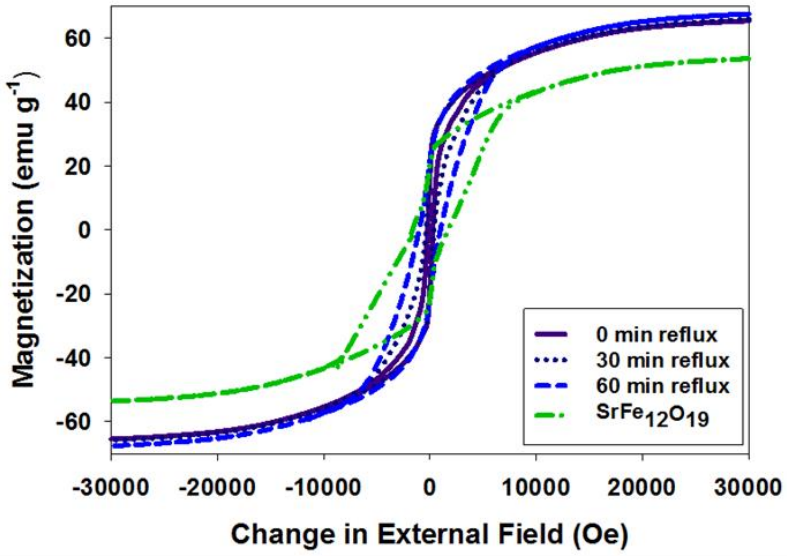

Figure 6.3.3.4 M-H curve of strontium ferrite/iron carbide composites at time 0, 30 min, and 60 minutes at reflux. The strontium original strontium ferrite is plotted as a reference.

6.4 Conclusion

The results conclude $Fe_7C_3/SrFe_{12}O_{19}$ have potential to compete with present day permanent magnets. The addition of a small percentage of strontium ferrite drastically enhanced the coercivity and remanence of the iron carbide. Utilizing iron carbide to further the enhance the magnetic properties of strontium ferrite shows potential from the increase in saturation and remanence values with some depletion of its coercivity in comparison to the strontium ferrite seed. Further enhancement of the microcomposite in future work may come from the synthesis of anisotropic $Fe_xC/SrFe_{12}O_{19}$ nanocomposites and synthesis of a core shell $Fe_xC/SrFe_{12}O_{19}$ material for better interfacial coupling of the hard and soft phases.

Chapter 7. Summary

The main objective of this work is to enhance the magnetic properties of iron carbide materials and nanocomposites for potential application as a rare-earth free permanent magnet alternative. Nanomagnetism, shape anisotropy, magnetocrystalline anisotropy, and exchange anisotropy were concepts used within this work to advance on its magnetic properties. Developments in this work include are listed below:

1. Iron carbide was synthesized from an iron carboxylate precursor in oleylamine, where oleylamine was determined to be the reduction and carbon source. CTAC and CTAB were utilized as an inducing agent to form highly crystalline iron carbide materials. While changing CTAB concentration was observed to have similar properties for all the samples, CTAC could be utilized to control particle, size, shape, crystal phase to manipulate the magnetic properties. Crystal phase control was obtained between orthorhombic Fe_3C and hexagonal Fe_7C_3, a phase rarely observed due to its metastable nature. Moreover hexagonal prisms 150 nm in thickness and 1 micron in length were obtained upon the formation of the hexagonal crystal phase. An increase in coercivity from 154 Oe to 590 Oe was achieved by decreasing the dimensions of iron carbide to 50 nm nanoaggregates.
2. Due to the intrinsic structure of hexagonal Fe_7C_3 further studies were done to probe the role of Cl^-, and quaternary amine in the reaction mixture. Lower boiling point amines were used as a synthesis medium in an attempt to lower the dimensions below 100 nm to achieve an increase in the demagnetization field. Results obtained determined Cl^- ions to have a high affinity for the (102) plane on carbide while long chain quaternary amines were required to maintain control of the hexagonal shape and phase. Lower boiling point solvents resulted in dimensions as low as 75 nm with low shape control due to less

separation of the nucleation and growth step. No impressive change in magnetic properties were achieved with tetradecylamine.

3. The Fe_7C_3 hexagonal structures were determined to have a textured structure from its strong (102) peak within its diffraction pattern. TEM diffraction confirmed single crystalline structures with the face parallel to the <102> axis. By aligning axis parallel to the external field on VSM an increase in magnetic remanence and saturation was observed. The material was determined to have shape-induced texture.
4. Using the synthesis method developed for semi-hard iron carbide, improvements were achieved from formation of a Fe_3C/CoO nanoaggregate material. Exchange bias materials have witnessed enhanced coercivity from the intrinsic interface of ferro-aniferromagnetic materials. Results obtained from VSM showed an increase from 450 to 600 Oe at room temperature. XPS confirmed the presence of a cobalt ferrite alloy at the interface while ZFC observed T_N to be at 275 K for CoO, therefore it is unlikely the enhanced properties are due to Fe_3C/CoO coupling at room temperature. The results confirm the increase in coercivity to attribute to the exchange interaction between Fe_3C and cobalt ferrite at the interface. Exchange bias was also observed in the Fe_3C/CoO nanoaggregates with a 150 Oe shift in the hysteresis curve upon cooling below the Verwey transition for the ferrite at the interface.
5. The hexagonal Fe_7C_3 synthesis was used to form a Fe_7C_3/strontium ferrite spring exchange magnet with enhanced properties. The composite material was achieved by partial reduction of strontium ferrite in oleylamine at different times to achieve different ratios of iron carbide to strontium ferrite. The best results were achieved at longer times without magnetic stirring which drastically slowed down the conversion of carbide (23.9% iron

carbide). Optimum magnetic properties were witnessed with 23.9% Fe_7C_3 and 76.1% strontium ferrite with an M_s of 67 emu g^{-1} and H_c of 1040 Oe.

References

1. Binns, C., *Nanomagnetism: Fundamentals and Applications*. Newnes: 2014; Vol. 6.
2. Poudyal, N.; Liu, J. P., Advances in nanostructured permanent magnets research. *Journal of Physics D: Applied Physics* **2012,** *46* (4), 043001.
3. Gutfleisch, O.; Willard, M. A.; Brück, E.; Chen, C. H.; Sankar, S.; Liu, J. P., Magnetic materials and devices for the 21st century: stronger, lighter, and more energy efficient. *Advanced materials* **2011,** *23* (7), 821-842.
4. Coey, J. M., *Magnetism and magnetic materials*. Cambridge University Press: 2010.
5. Kasap, S. O., *Principles of electronic materials and devices*. McGraw-Hill New York: 2006; Vol. 784.
6. Atkins, P., *Shriver and Atkins' inorganic chemistry*. Oxford University Press, USA: 2010.
7. Wang, Y.; Li, Y.; Rong, C.; Liu, J. P., Sm–Co hard magnetic nanoparticles prepared by surfactant-assisted ball milling. *Nanotechnology* **2007,** *18* (46), 465701.
8. Soares, J.; Galdino, V.; Conceição, O.; Morales, M.; de Araújo, J.; Machado, F., Critical dimension for magnetic exchange-spring coupled core/shell CoFe2O4/CoFe2 nanoparticles. *Journal of Magnetism and Magnetic Materials* **2013,** *326*, 81-84.
9. López-Ortega, A.; Estrader, M.; Salazar-Alvarez, G.; Roca, A. G.; Nogués, J., Applications of exchange coupled bi-magnetic hard/soft and soft/hard magnetic core/shell nanoparticles. *Physics Reports* **2015,** *553*, 1-32.
10. Coey, J., Hard magnetic materials: A perspective. *Magnetics, IEEE Transactions on* **2011,** *47* (12), 4671-4681.
11. Gutfleisch, O., Controlling the properties of high energy density permanent magnetic materials by different processing routes. *Journal of Physics D: Applied Physics* **2000,** *33* (17), R157.
12. Oliver, D.; Shedden, J., Disk damping magnets for electricity energy meters in the newer permanent magnet alloys. *Journal of Scientific Instruments* **1938,** *15* (6), 193.
13. Andriotis, A. N.; Menon, M., The synergistic character of the defect-induced magnetism in diluted magnetic semiconductors and related magnetic materials. *J Phys Condens Matter* **2012,** *24* (45), 455801.
14. Went, J.; Rathenau, G.; Gorter, E.; Van Oosterhout, G., Ferroxdure, a class of new permanent magnet materials. *Philips Tech. Rev* **1952,** *13* (7), 194-208.
15. Cochardt, A., Modified strontium ferrite, a new permanent magnet material. *J Appl Phys* **1963,** *34* (4), 1273-1274.
16. Baykal, A., Solvothermal synthesis of pure SrFe12O19 hexaferrite nanoplatelets. *Journal of Superconductivity and Novel Magnetism* **2014,** *27* (3), 877-880.
17. McCurrie, R. A., *Ferromagnetic materials*. Academic Press: 1994.
18. Das, D., Twenty million energy product samarium-cobalt magnet. *IEEE Transactions on Magnetics* **1969,** *5* (3), 214-216.
19. Hoffer, G.; Strnat, K., Magnetocrystalline anisotropy of YCo 5 and Y 2 Co 17. *IEEE Transactions on Magnetics* **1966,** *2* (3), 487-489.
20. Sagawa, M.; Fujimura, S.; Togawa, N.; Yamamoto, H.; Matsuura, Y., New material for permanent magnets on a base of Nd and Fe. *J Appl Phys* **1984,** *55* (6), 2083-2087.
21. Sagawa, M.; Fujimura, S.; Yamamoto, H.; Matsuura, Y.; Hiraga, K., Permanent magnet materials based on the rare earth-iron-boron tetragonal compounds. *IEEE transactions on Magnetics* **1984,** *20* (5), 1584-1589.

22. Nakamura, H.; Hirota, K.; Shimao, M.; Minowa, T.; Honshima, M., Magnetic properties of extremely small Nd-Fe-B sintered magnets. *IEEE transactions on magnetics* **2005,** *41* (10), 3844-3846.
23. Sepehri-Amin, H.; Ohkubo, T.; Nishiuchi, T.; Hirosawa, S.; Hono, K., Coercivity enhancement of hydrogenation–disproportionation–desorption–recombination processed Nd–Fe–B powders by the diffusion of Nd–Cu eutectic alloys. *Scripta Materialia* **2010,** *63* (11), 1124-1127.
24. Kamino, K.; Kawaguchi, T.; Nagakura, M., Magnetic properties of MnAl system alloys. *IEEE Transactions on Magnetics* **1966,** *2* (3), 506-510.
25. Yang, Y. B.; Chen, X. G.; Wu, R.; Wei, J. Z.; Ma, X. B.; Han, J. Z.; Du, H. L.; Liu, S. Q.; Wang, C. S.; Yang, Y. C.; Zhang, Y.; Yang, J. B., Preparation and magnetic properties of MnBi. *J Appl Phys* **2012,** *111* (7), 3.
26. Chinnasamy, C.; Huang, J.; Lewis, L.; Latha, B.; Vittoria, C.; Harris, V., Direct chemical synthesis of high coercivity air-stable SmCo nanoblades. *Appl Phys Lett* **2008,** *93* (3), 032505.
27. Harris, V.; Chen, Y.; Yang, A.; Yoon, S.; Chen, Z.; Geiler, A.; Gao, J.; Chinnasamy, C.; Lewis, L.; Vittoria, C., High coercivity cobalt carbide nanoparticles processed via polyol reaction: a new permanent magnet material. *Journal of Physics D: Applied Physics* **2010,** *43* (16), 165003.
28. Huba, Z. J.; Carpenter, E. E., A versatile synthetic approach for the synthesis of CoO, CoxC, and Co based nanocomposites: tuning kinetics and crystal phase with different polyhydric alcohols. *Crystengcomm* **2014,** *16* (34), 8000-8007.
29. Minobe, S.; Nakajima, Y.; Hirose, K.; Ohishi, Y., Stability and compressibility of a new iron-nitride β-Fe7N3 to core pressures. *Geophysical Research Letters* **2015,** *42* (13), 5206-5211.
30. Jack, K. In *The Occurrence and the Crystal Structure of $\alpha^{\prime\prime} $-Iron Nitride; a New Type of Interstitial Alloy Formed during the Tempering of Nitrogen-Martensite*, Proceedings of the Royal Society of London A: Mathematical, Physical and Engineering Sciences, The Royal Society: 1951; pp 216-224.
31. Kim, T.; Takahashi, M., New magnetic material having ultrahigh magnetic moment. *Appl Phys Lett* **1972,** *20* (12), 492-494.
32. Kita, E.; Shibata, K.; Yanagihara, H.; Sasaki, Y.; Kishimoto, M., Magnetic properties of core–shell type Fe16N2 nanoparticles. *Journal of Magnetism and Magnetic Materials* **2007,** *310* (2), 2411-2413.
33. Dirba, I.; Schwöbel, C.; Diop, L.; Duerrschnabel, M.; Molina-Luna, L.; Hofmann, K.; Komissinskiy, P.; Kleebe, H.-J.; Gutfleisch, O., Synthesis, morphology, thermal stability and magnetic properties of α ″-Fe 16 N 2 nanoparticles obtained by hydrogen reduction of γ-Fe 2 O 3 and subsequent nitrogenation. *Acta Materialia* **2017,** *123*, 214-222.
34. Wehrenberg, C.; Zande, B.; Simizu, S.; Obermyer, R.; Sankar, S.; Thadhani, N., Shock compression response of α ″-Fe16N2 nanoparticles. *J Appl Phys* **2012,** *111* (8), 083522.
35. Jellinghaus, W., New alloys with high coercive force. *Z. tech. Physik* **1936,** *17*, 33-36.
36. Kaneko, H.; Homma, M.; Suzuki, K., A New Heat-treatment of Pt–Co Alloys of High-Grade Magnetic Properties. *Transactions of the Japan Institute of Metals* **1968,** *9* (2), 124-129.
37. Wang, C.; Hou, Y.; Kim, J.; Sun, S., A general strategy for synthesizing FePt nanowires and nanorods. *Angewandte Chemie* **2007,** *119* (33), 6449-6451.
38. Faraoun, H.; Zhang, Y.; Esling, C.; Aourag, H., Crystalline, electronic, and magnetic structures of θ-Fe 3 C, χ-Fe 5 C 2, and η-Fe 2 C from first principle calculation. *J Appl Phys* **2006,** *99* (9), 093508.
39. Fang, C. M.; van Huis, M. A.; Zandbergen, H. W., Structural, electronic, and magnetic properties of iron carbide Fe7C3 phases from first-principles theory. *Phys Rev B* **2009,** *80* (22).
40. Huang, G. M.; Hu, J.; Zhang, H.; Zhou, Z. J.; Chi, X. Q.; Gao, J. H., Highly magnetic iron carbide nanoparticles as effective T-2 contrast agents. *Nanoscale* **2014,** *6* (2), 726-730.
41. de Smit, E.; Cinquini, F.; Beale, A. M.; Safonova, O. V.; van Beek, W.; Sautet, P.; Weckhuysen, B. M., Stability and Reactivity of epsilon-chi-theta Iron Carbide Catalyst Phases in Fischer-Tropsch Synthesis: Controlling mu(c). *J Am Chem Soc* **2010,** *132* (42), 14928-14941.

42. Giordano, C.; Kraupner, A.; Wimbush, S. C.; Antonietti, M., Iron carbide: An ancient advanced material. *Small* **2010,** *6* (17), 1859-1862.
43. Tajima, S.; Hirano, S.-i., Synthesis and magnetic properties of Fe7C3 particles with high saturation magnetization. *Jpn J Appl Phys* **1990,** *29* (4R), 662.
44. Lamer, V. K.; Dinegar, R. H., Theory, Production and Mechanism of Formation of Monodispersed Hydrosols. *J Am Chem Soc* **1950,** *72* (11), 4847-4854.
45. Thanh, N. T. K.; Maclean, N.; Mahiddine, S., Mechanisms of Nucleation and Growth of Nanoparticles in Solution. *Chem Rev* **2014,** *114* (15), 7610-7630.
46. Lalena, J. N.; Cleary, D. A.; Carpenter, E.; Dean, N. F., *Inorganic materials synthesis and fabrication*. John Wiley & Sons: 2008.
47. Casey, W. H., Entropy Production and the Ostwald Step Rule. *J Phys Chem-Us* **1988,** *92* (1), 226-227.
48. Navrotsky, A., Energetic clues to pathways to biomineralization: Precursors, clusters, and nanoparticles. *P Natl Acad Sci USA* **2004,** *101* (33), 12096-12101.
49. Baumgartner, J.; Dey, A.; Bomans, P. H. H.; Le Coadou, C.; Fratzl, P.; Sommerdijk, N. A. J. M.; Faivre, D., Nucleation and growth of magnetite from solution. *Nat Mater* **2013,** *12* (4), 310-314.
50. Majidi, S.; Zeinali Sehrig, F.; Farkhani, S. M.; Soleymani Goloujeh, M.; Akbarzadeh, A., Current methods for synthesis of magnetic nanoparticles. *Artificial cells, nanomedicine, and biotechnology* **2016,** *44* (2), 722-734.
51. Rockenberger, J.; Scher, E. C.; Alivisatos, A. P., A new nonhydrolytic single-precursor approach to surfactant-capped nanocrystals of transition metal oxides. *J Am Chem Soc* **1999,** *121* (49), 11595-11596.
52. Shan, J.; Wang, L.; Yu, H.; Ji, J.; Amer, W.; Chen, Y.; Jing, G.; Khalid, H.; Akram, M.; Abbasi, N., Recent progress in Fe3O4 based magnetic nanoparticles: from synthesis to application. *Materials Science and Technology* **2016,** *32* (6), 602-614.
53. Teja, A. S.; Koh, P.-Y., Synthesis, properties, and applications of magnetic iron oxide nanoparticles. *Progress in crystal growth and characterization of materials* **2009,** *55* (1), 22-45.
54. Park, J.; An, K.; Hwang, Y.; Park, J.-G.; Noh, H.-J.; Kim, J.-Y.; Park, J.-H.; Hwang, N.-M.; Hyeon, T., Ultra-large-scale syntheses of monodisperse nanocrystals. *Nat Mater* **2004,** *3* (12), 891-895.
55. Belaïd, S.; Laurent, S.; Vermeersch, M.; Vander Elst, L.; Perez-Morga, D.; Muller, R. N., A new approach to follow the formation of iron oxide nanoparticles synthesized by thermal decomposition. *Nanotechnology* **2013,** *24* (5), 055705.
56. (a) William, W. Y.; Falkner, J. C.; Yavuz, C. T.; Colvin, V. L., Synthesis of monodisperse iron oxide nanocrystals by thermal decomposition of iron carboxylate salts. *Chem Comm* **2004,** (20), 2306-2307; (b) Park, J.; Lee, E.; Hwang, N. M.; Kang, M.; Kim, S. C.; Hwang, Y.; Park, J. G.; Noh, H. J.; Kim, J. Y.; Park, J. H., One-nanometer-scale size-controlled synthesis of monodisperse magnetic Iron oxide nanoparticles. *Angewandte Chemie* **2005,** *117* (19), 2932-2937.
57. Jun, Y. w.; Choi, J. s.; Cheon, J., Shape control of semiconductor and metal oxide nanocrystals through nonhydrolytic colloidal routes. *Angewandte Chemie International Edition* **2006,** *45* (21), 3414-3439.
58. Hutchings, G.; Polshettiwar, V.; Asefa, T., *Nanocatalysis: Synthesis and Applications*. John Wiley & Sons: 2013.
59. (a) Lu, A. H.; Salabas, E. e. L.; Schüth, F., Magnetic nanoparticles: synthesis, protection, functionalization, and application. *Angewandte Chemie International Edition* **2007,** *46* (8), 1222-1244; (b) Salazar-Alvarez, G.; Qin, J.; Sepelak, V.; Bergmann, I.; Vasilakaki, M.; Trohidou, K.; Ardisson, J.; Macedo, W.; Mikhaylova, M.; Muhammed, M., Cubic versus spherical magnetic nanoparticles: the role of surface anisotropy. *J Am Chem Soc* **2008,** *130* (40), 13234-13239.
60. Palchoudhury, S.; Xu, Y.; An, W.; Turner, C. H.; Bao, Y., Platinum attachments on iron oxide nanoparticle surfaces. *J Appl Phys* **2010,** *107* (9), 09B311.

61. Palchoudhury, S.; Xu, Y.; Goodwin, J.; Bao, Y., Synthesis of iron oxide nanoworms. *J Appl Phys* **2011,** *109* (7), 07E314.
62. Ge, W.; Sato, R.; Wu, H. L.; Teranishi, T., Simple Surfactant Concentration-Dependent Shape Control of Polyhedral Fe3O4 Nanoparticles and Their Magnetic Properties. *ChemPhysChem* **2015,** *16* (15), 3200-3205.
63. Chen, M.; Feng, Y. G.; Wang, X.; Li, T. C.; Zhang, J. Y.; Qian, D. J., Silver nanoparticles capped by oleylamine: Formation, growth, and self-organization. *Langmuir* **2007,** *23* (10), 5296-5304.
64. Mojahed, F.; Dehghanpour, S.; Alizadeh, M.; Mahmoudi, A., Wet Chemical Synthesis of Oleylamine-Capped Silver Nanoparticles by a Fast and Facile Reproducible Method. *Synthesis and Reactivity in Inorganic, Metal-Organic, and Nano-Metal Chemistry* **2011,** *41* (6), 664-670.
65. De la Presa, P.; Multigner, M.; De la Venta, J.; García, M.; Ruiz-González, M., Structural and magnetic characterization of oleic acid and oleylamine-capped gold nanoparticles. *J Appl Phys* **2006,** *100* (12), 123915.
66. Mourdikoudis, S.; Liz-Marzán, L. M., Oleylamine in nanoparticle synthesis. *Chem Mater* **2013,** *25* (9), 1465-1476.
67. Carenco, S.; Labouille, S.; Bouchonnet, S.; Boissière, C.; Le Goff, X. F.; Sanchez, C.; Mézailles, N., Revisiting the molecular roots of a ubiquitously successful synthesis: nickel (0) nanoparticles by reduction of [Ni (acetylacetonate) 2]. *Chemistry-A European Journal* **2012,** *18* (44), 14165-14173.
68. Yu, Y.; Yang, W.; Sun, X.; Zhu, W.; Li, X.-Z.; Sellmyer, D. J.; Sun, S., Monodisperse MPt (M= Fe, Co, Ni, Cu, Zn) nanoparticles prepared from a facile oleylamine reduction of metal salts. *Nano Lett* **2014,** *14* (5), 2778-2782.
69. Meffre, A.; Lachaize, S.; Gatel, C.; Respaud, M.; Chaudret, B., Use of long chain amine as a reducing agent for the synthesis of high quality monodisperse iron(0) nanoparticles. *Journal of Materials Chemistry* **2011,** *21* (35), 13464-13469.
70. Scherrer, P., Bestimmung der inneren Struktur und der Größe von Kolloidteilchen mittels Röntgenstrahlen. In *Kolloidchemie Ein Lehrbuch*, Springer: 1912; pp 387-409.
71. McCusker, L.; Von Dreele, R.; Cox, D.; Louër, D.; Scardi, P., Rietveld refinement guidelines. *Journal of Applied Crystallography* **1999,** *32* (1), 36-50.
72. Leng, Y., *Materials characterization: introduction to microscopic and spectroscopic methods*. John Wiley & Sons: 2009.
73. Leng, Y., *Scanning Electron Microscopy*. Weinheim, Germany: Wiley-VCH Verlag GmbH & Co. KGaA: Weinheim, Germany, 2013; p 127-161.
74. Foner, S., Versatile and sensitive vibrating-sample magnetometer. *Review of Scientific Instruments* **1959,** *30* (7), 548-557.
75. De, A.; Dewan, M.; Mozumdar, S., Experimental and Theoretical Background to Study Materials. *Advanced Sensor and Detection Materials* **2014**, 453-466.
76. Glaspell, G.; Abdelsayed, V.; Saoud, K. M.; El-Shall, M. S., Vapor-phase synthesis of metallic and intermetallic nanoparticles and nanowires: magnetic and catalytic properties. *Pure and applied chemistry* **2006,** *78* (9), 1667-1689.
77. Turner, S. S., Measurement of Bulk Magnetic Properties. *Multi Length-Scale Characterisation* **2014**, 1-61.
78. Ferraro, J. R., *Introductory raman spectroscopy*. Academic press: 2003.
79. Beams, R.; Cançado, L. G.; Novotny, L., Raman characterization of defects and dopants in graphene. *Journal of Physics: Condensed Matter* **2015,** *27* (8), 083002.
80. Meffre, A.; Mehdaoui, B.; Kelsen, V.; Fazzini, P. F.; Carrey, J.; Lachaize, S.; Respaud, M.; Chaudret, B., A Simple Chemical Route toward Monodisperse Iron Carbide Nanoparticles Displaying Tunable Magnetic and Unprecedented Hyperthermia Properties. *Nano Lett* **2012,** *12* (9), 4722-4728.

81. Davydov, V.; Rakhmanina, A.; Kireev, I.; Alieva, I.; Zhironkina, O.; Strelkova, O.; Dianova, V.; Samani, T. D.; Mireles, K.; Yahia, L. H., Solid state synthesis of carbon-encapsulated iron carbide nanoparticles and their interaction with living cells. *Journal of Materials Chemistry B* **2014,** *2* (27), 4250-4261.
82. Yu, S.; Chow, G., Synthesis, structural, magnetic, and cytotoxic properties of iron oxide coated iron/iron-carbide nanocomposite particles. *J Appl Phys* **2005,** *98* (11), 114306-114306.
83. Carroll, K. J.; Reveles, J. U.; Shultz, M. D.; Khanna, S. N.; Carpenter, E. E., Preparation of elemental Cu and Ni nanoparticles by the polyol method: an experimental and theoretical approach. *The Journal of Physical Chemistry C* **2011,** *115* (6), 2656-2664.
84. Huba, Z. J.; Carpenter, E. E., Ethanol assisted reduction and nucleation of ferromagnetic Co and Ni nanocrystalline particles. *Crystengcomm* **2013,** *15* (44), 8919-8923.
85. El-Gendy, A. A.; Qian, M. C.; Huba, Z. J.; Khanna, S. N.; Carpenter, E. E., Enhanced magnetic anisotropy in cobalt-carbide nanoparticles. *Appl Phys Lett* **2014,** *104* (2).
86. El-Gendy, A. A.; Khavrus, V. O.; Hampel, S.; Leonhardt, A.; Buchner, B.; Klingeler, R., Morphology, structural control, and magnetic properties of carbon-coated nanoscaled NiRu alloys. *The Journal of Physical Chemistry C* **2010,** *114* (24), 10745-10749.
87. Zhou, J.; Qiao, X.; Binks, B. P.; Sun, K.; Bai, M.; Li, Y.; Liu, Y., Magnetic Pickering emulsions stabilized by Fe3O4 nanoparticles. *Langmuir* **2011,** *27* (7), 3308-3316.
88. Ruston, W. R.; Warzee, M.; Hennaut, J.; Waty, J., Solid Reaction Products of Catalytic Decomposition of Carbon Monoxide on Iron at 550 Degrees C. *Carbon* **1969,** *7* (1), 47-&.
89. Mansker, L. D.; Jin, Y. M.; Bukur, D. B.; Datye, A. K., Characterization of slurry phase iron catalysts for Fischer-Tropsch synthesis. *Appl Catal a-Gen* **1999,** *186* (1-2), 277-296.
90. Tajima, S.; Hirano, S., Synthesis and Magnetic-Properties of Fe7c3 Particles with High Saturation Magnetization. *Jpn J Appl Phys 1* **1990,** *29* (4), 662-668.
91. Eckstrom, H. C.; Adcock, W. A., A new iron carbide in hydrocarbon synthesis catalysts. *J Am Chem Soc* **1950,** *72* (2), 1042-1043.
92. Herbstein, F.; Snyman, J., Identification of Eckstrom-Adcock iron carbide as Fe7C3. *Inorganic Chemistry* **1964,** *3* (6), 894-896.
93. Bauergrosse, E.; Frantz, C.; Lecaer, G.; Heiman, N., Formation of Fe7c3 and Fe5c2 Type Metastable Carbides during the Crystallization of an Amorphous Fe75c25 Alloy. *J Non-Cryst Solids* **1981,** *44* (2-3), 277-286.
94. Tsuzuki, A.; Sago, S.; Hirano, S.-I.; Naka, S., High temperature and pressure preparation and properties of iron carbides Fe7C3 and Fe3C. *Journal of materials science* **1984,** *19* (8), 2513-2518.
95. Miura, K.; Itoh, M.; Machida, K., Surfactant-assisted preparation and magnetic properties of iron-based nanowires. *Jpn J Appl Phys* **2008,** *47* (4), 2342-2344.
96. Barinov, V. A.; Tsurin, V. A.; Surikov, V. T., Study of mechanically synthesized carbide Fe7C3. *Phys Met Metallogr+* **2010,** *110* (5), 474-484.
97. Huba, Z. J.; Carpenter, E. E., Monitoring the formation of carbide crystal phases during the thermal decomposition of 3d transition metal dicarboxylate complexes. *Dalton T* **2014,** *43* (32), 12236-12242.
98. Chen, C.-J.; Chiang, R.-K.; Wang, J.-S.; Wang, S.-L., Synthesis and magnetic properties of octahedral magnetite nanoparticles in 20–110 nm range. *J Nanopart Res* **2013,** *15* (8), 1-10.
99. Gomez, E.; Pane, S.; Alcobe, X.; Valles, E., Influence of a cationic surfactant in the properties of cobalt–nickel electrodeposits. *Electrochimica acta* **2006,** *51* (26), 5703-5709.
100. Ahmed, J.; Sharma, S.; Ramanujachary, K. V.; Lofland, S. E.; Ganguli, A. K., Microemulsion-mediated synthesis of cobalt (pure fcc and hexagonal phases) and cobalt–nickel alloy nanoparticles. *Journal of colloid and interface science* **2009,** *336* (2), 814-819.

101. Pearson, W. B., *A handbook of lattice spacings and structures of metals and alloys*. Pergamon Press: 1967.
102. Zhang, S.; Jiang, G.; Filsinger, G. T.; Wu, L.; Zhu, H.; Lee, J.; Wu, Z.; Sun, S., Halide ion-mediated growth of single crystalline Fe nanoparticles. *Nanoscale* **2014,** *6* (9), 4852-4856.
103. Yang, Z.; Zhao, T.; Huang, X.; Chu, X.; Tang, T.; Ju, Y.; Wang, Q.; Hou, Y.; Gao, S., Modulating the phases of iron carbide nanoparticles: from a perspective of interfering with the carbon penetration of Fe@ Fe 3 O 4 by selectively adsorbed halide ions. *Chemical Science* **2017,** *8* (1), 473-481.
104. (a) Zou, Y.; Li, D.; Yang, D., Shape and phase control of CdS nanocrystals using cationic surfactant in noninjection synthesis. *Nanoscale research letters* **2011,** *6* (1), 1-6; (b) Lei, Y.; Liao, Q.; Fu, H.; Yao, J., Phase-and shape-controlled synthesis of single crystalline perylene nanosheets and its optical properties. *The Journal of Physical Chemistry C* **2009,** *113* (23), 10038-10043.
105. Tomaszewski, P. E., The uncertainty in the grain size calculation from X-ray diffraction data. *Phase Transitions* **2013,** *86* (2-3), 260-266.
106. Joseyphus, R. J.; Shinoda, K.; Kodama, D.; Jeyadevan, B., Size controlled Fe nanoparticles through polyol process and their magnetic properties. *Materials Chemistry and Physics* **2010,** *123* (2), 487-493.
107. El-Gendy, A. A.; Almugaiteeb, T.; Carpenter, E. E., Co x C nanorod magnets: Highly magnetocrystalline anisotropy with lower Curie temperature for potential applications. *Journal of Magnetism and Magnetic Materials* **2013,** *348*, 136-139.
108. Chesnel, K.; Trevino, M.; Cai, Y.; Hancock, J.; Smith, S.; Harrison, R. In *Particle size effects on the magnetic behaviour of 5 to 11 nm Fe3O4 nanoparticles coated with oleic acid*, Journal of Physics: Conference Series, IOP Publishing: 2014; p 012004.
109. Niu, W.; Zheng, S.; Wang, D.; Liu, X.; Li, H.; Han, S.; Chen, J.; Tang, Z.; Xu, G., Selective synthesis of single-crystalline rhombic dodecahedral, octahedral, and cubic gold nanocrystals. *J Am Chem Soc* **2008,** *131* (2), 697-703.
110. Zhang, L.; Niu, W.; Xu, G., Synthesis and applications of noble metal nanocrystals with high-energy facets. *Nano Today* **2012,** *7* (6), 586-605.
111. Zhang, J.; Kuang, Q.; Jiang, Y.; Xie, Z., Engineering high-energy surfaces of noble metal nanocrystals with enhanced catalytic performances. *Nano Today* **2016,** *11* (5), 661-677.
112. Yang, C.; Zhao, H. B.; Hou, Y. L.; Ma, D., Fe5C2 Nanoparticles: A Facile Bromide-Induced Synthesis and as an Active Phase for Fischer-Tropsch Synthesis. *J Am Chem Soc* **2012,** *134* (38), 15814-15821.
113. Vansanten, R. A., The Ostwald Step Rule. *J Phys Chem-Us* **1984,** *88* (24), 5768-5769.
114. Zuo, W.-L.; Zhao, X.; Xiong, J.-F.; Zhang, M.; Zhao, T.-Y.; Hu, F.-X.; Sun, J.-R.; Shen, B.-G., Strong textured SmCo5 nanoflakes with ultrahigh coercivity prepared by multistep (three steps) surfactant-assisted ball milling. *Scientific reports* **2015,** *5*, 13117.
115. Kronmüller, H.; Durst, K.-D.; Martinek, G., Angular dependence of the coercive field in sintered Fe77Nd15B8 magnets. *Journal of magnetism and magnetic materials* **1987,** *69* (2), 149-157.
116. Elbaz, D.; Givord, D.; Hirosawa, S.; Missell, F.; Rossignol, M.; Villas-Boas, V., Angular dependence of coercivity in sintered RFeB magnets. *J Appl Phys* **1991,** *69* (8), 5492-5494.
117. Bance, S.; Oezelt, H.; Schrefl, T.; Ciuta, G.; Dempsey, N. M.; Givord, D.; Winklhofer, M.; Hrkac, G.; Zimanyi, G.; Gutfleisch, O., Influence of defect thickness on the angular dependence of coercivity in rare-earth permanent magnets. *Appl Phys Lett* **2014,** *104* (18), 182408.
118. Nakajima, Y.; Takahashi, E.; Suzuki, T.; Funakoshi, K.-i., "Carbon in the core" revisited. *Physics of the Earth and Planetary Interiors* **2009,** *174* (1), 202-211.
119. Žaludová, M.; Smetana, B.; Zlá, S.; Dobrovská, J.; Vodárek, V.; Konečná, K.; Matějka, V.; Matějková, P., Experimental study of Fe–C–O based system below 1000 C. *Journal of thermal analysis and calorimetry* **2013,** *111* (2), 1203-1210.

120. Carroll, K. J.; Huba, Z. J.; Spurgeon, S. R.; Qian, M.; Khanna, S. N.; Hudgins, D. M.; Taheri, M. L.; Carpenter, E. E., Magnetic properties of Co2C and Co3C nanoparticles and their assemblies. *Appl Phys Lett* **2012,** *101* (1), 012409.
121. El-Gendy, A. A.; Qian, M.; Huba, Z. J.; Khanna, S. N.; Carpenter, E. E., Enhanced magnetic anisotropy in cobalt-carbide nanoparticles. *Appl Phys Lett* **2014,** *104* (2), 023111.
122. Huba, Z. J.; Carpenter, E. E., Size and phase control of cobalt–carbide nanoparticles using OH− and Cl− anions in a polyol process. *J Appl Phys* **2012,** *111* (7), 07B529.
123. Gupta, A. K.; Wells, S., Surface-modified superparamagnetic nanoparticles for drug delivery: preparation, characterization, and cytotoxicity studies. *IEEE transactions on nanobioscience* **2004,** *3* (1), 66-73.
124. Yao, X.-J.; He, X.-M.; Song, X.-Y.; Ding, Q.; Li, Z.-W.; Zhong, W.; Au, C.-T.; Du, Y.-W., Enhanced exchange bias and coercivity arising from heterojunctions in Ni–NiO nanocomposites. *Phys Chem Chem Phys* **2014,** *16* (15), 6925-6930.
125. Chen, C.-J.; Chiang, R.-K.; Kamali, S.; Wang, S.-L., Synthesis and controllable oxidation of monodisperse cobalt-doped wüstite nanoparticles and their core–shell stability and exchange-bias stabilization. *Nanoscale* **2015,** *7* (34), 14332-14343.
126. Senapati, S.; Srivastava, S. K.; Singh, S. B., Synthesis, characterization and photocatalytic activity of magnetically separable hexagonal Ni/ZnO nanostructure. *Nanoscale* **2012,** *4* (20), 6604-6612.
127. Tian, Y.; Bakaul, S. R.; Wu, T., Oxide nanowires for spintronics: materials and devices. *Nanoscale* **2012,** *4* (5), 1529-1540.
128. (a) Wang, J.; Sannomiya, T.; Shi, J.; Nakamura, Y., Influence of interface roughness on the exchange bias of Co/CoO multilayers. *J Appl Phys* **2013,** *113* (17), 17D707; (b) Zhang, W.; Krishnan, K. M., Exchange bias and blocking temperature distribution of Fe-film/CoO-nanoparticle hybrid bilayers. *J Appl Phys* **2014,** *115* (17), 17D714.
129. Liu, X.; Pichon, B. P.; Ulhaq, C.; Lefevre, C.; Greneche, J.-M.; Begin, D.; Begin-Colin, S., Systematic Study of Exchange Coupling in Core–Shell Fe3− δO4@ CoO Nanoparticles. *Chem Mater* **2015,** *27* (11), 4073-4081.
130. Lima Jr, E.; Winkler, E. L.; Tobia, D.; Troiani, H. E.; Zysler, R. D.; Agostinelli, E.; Fiorani, D., Bimagnetic CoO Core/CoFe2O4 shell nanoparticles: synthesis and magnetic properties. *Chem Mater* **2012,** *24* (3), 512-516.
131. Fontaíña Troitiño, N.; Rivas-Murias, B.; Rodríguez-González, B.; Salgueiriño, V. n., Exchange Bias Effect in CoO@ Fe3O4 Core–Shell Octahedron-Shaped Nanoparticles. *Chem Mater* **2014,** *26* (19), 5566-5575.
132. Liu, S.; Ding, N.; Ye, E.; Zong, Y.; Wang, D.; Knoll, W.; Han, M.-Y., Oxidation-induced constituent separation of magnetic exchange biased Fe/CoO nanocrystals. *Chem Comm* **2009,** (41), 6255-6257.
133. Williams, B.; Clifford, D.; El-Gendy, A. A.; Carpenter, E. E., Solvothermal synthesis of Fe7C3 and Fe3C nanostructures with phase and morphology control. *J Appl Phys* **2016,** *120* (3), 033904.
134. Zhao, X.; Liang, Y.; Hu, Z.; Liu, B., Oxidation characteristics and magnetic properties of iron carbide and iron ultrafine particles. *J Appl Phys* **1996,** *80* (10), 5857-5860.
135. Razumovskiy, V.; Ghosh, G., A first-principles study of cementite (Fe 3 C) and its alloyed counterparts: structural properties, stability, and electronic structure. *Computational Materials Science* **2015,** *110*, 169-181.
136. Chen, H.-Y.; Maiti, S.; Nelson, C. A.; Zhu, X.; Son, D. H., Tuning Temperature Dependence of Dopant Luminescence via Local Lattice Strain in Core/Shell Nanocrystal Structure. *The Journal of Physical Chemistry C* **2012,** *116* (44), 23838-23843.
137. Petitto, S. C.; Marsh, E. M.; Carson, G. A.; Langell, M. A., Cobalt oxide surface chemistry: The interaction of CoO(1 0 0), Co3O4(1 1 0) and Co3O4(1 1 1) with oxygen and water. *Journal of Molecular Catalysis A: Chemical* **2008,** *281* (1–2), 49-58.

138. Syugaev, A.; Lyalina, N.; Lomayeva, S.; Maratkanova, A., Electrochemical behavior of Co3C carbide. *Journal of Solid State Electrochemistry* **2015,** *19* (10), 2933-2941.
139. Wilson, D.; Langell, M. A., XPS analysis of oleylamine/oleic acid capped Fe3O4 nanoparticles as a function of temperature. *Applied Surface Science* **2014,** *303*, 6-13.
140. Ourry, L.; Mammeri, F.; Toulemon, D.; Gaudisson, T.; Delamar, M.; Ammar, S., A tandem polyol process and ATRP used to design new processable hybrid exchange-biased Co x Fe 3− x O 4@ CoO@ PMMA nanoparticles. *RSC Advances* **2016,** *6* (55), 49973-49979.
141. Long, N. V.; Yang, Y.; Teranishi, T.; Thi, C. M.; Cao, Y.; Nogami, M., Related magnetic properties of CoFe 2 O 4 cobalt ferrite particles synthesised by the polyol method with NaBH 4 and heat treatment: new micro and nanoscale structures. *RSC Advances* **2015,** *5* (70), 56560-56569.
142. Lu, A.; Chen, Y.; Zeng, D.; Li, M.; Xie, Q.; Zhang, X.; Peng, D.-L., Shape-related optical and catalytic properties of wurtzite-type CoO nanoplates and nanorods. *Nanotechnology* **2013,** *25* (3), 035707.
143. Wang, Y.; Dong, L.; Xiong, R.; Hu, A., Practical access to bandgap-like N-doped carbon dots with dual emission unzipped from PAN@ PMMA core–shell nanoparticles. *J Mater Chem C* **2013,** *1* (46), 7731-7735.
144. Anhøj, T. A.; Jacobsen, C. S.; Mørup, S., Magnetic properties of Fe1-xMnx/Fe nanocomposites. *J Appl Phys* **2004,** *95* (7), 3649-3654.
145. Yuan, C., Room-temperature coercivity of Ni/NiO core/shell nanoparticles fabricated by pulsed laser deposition. *The Journal of Physical Chemistry C* **2010,** *114* (5), 2124-2126.
146. Papaefthymiou, V.; Kostikas, A.; Simopoulos, A.; Niarchos, D.; Gangopadyay, S.; Hadjipanayis, G.; Sorensen, C.; Klabunde, K., Magnetic hysteresis and Mössbauer studies in ultrafine iron particles. *J Appl Phys* **1990,** *67* (9), 4487-4489.
147. Primc, D.; Makovec, D., Composite nanoplatelets combining soft-magnetic iron oxide with hard-magnetic barium hexaferrite. *Nanoscale* **2015,** *7* (6), 2688-2697.
148. Zeng, H.; Li, J.; Liu, J. P.; Wang, Z. L.; Sun, S., Exchange-coupled nanocomposite magnets by nanoparticle self-assembly. *Nature* **2002,** *420* (6914), 395-398.
149. Muxworthy, A.; McClelland, E., Review of the low-temperature magnetic properties of magnetite from a rock magnetic perspective. *Geophysical Journal International* **2000,** *140* (1), 101-114.
150. Pham-Huu, C.; Keller, N.; Estournes, C.; Ehret, G.; Greneche, J.; Ledoux, M., Microstructural investigation and magnetic properties of CoFe 2 O 4 nanowires synthesized inside carbon nanotubes. *Phys Chem Chem Phys* **2003,** *5* (17), 3716-3723.
151. Chitu, L.; Jergel, M.; Majkova, E.; Luby, S.; Capek, I.; Satka, A.; Ivan, J.; Kovac, J.; Timko, M., Structure and magnetic properties of CoFe 2 O 4 and Fe 3 O 4 nanoparticles. *Materials Science and Engineering: C* **2007,** *27* (5), 1415-1417.
152. Zhang, W.; Wen, T.; Krishnan, K. M., Positive exchange bias and upward magnetic relaxation in a Fe-film/CoO-nanoparticle hybrid system. *Appl Phys Lett* **2012,** *101* (13), 132401.
153. Roy, D.; Kumar, P. A., Enhancement of (BH) max in a hard-soft-ferrite nanocomposite using exchange spring mechanism. *J Appl Phys* **2009,** *106* (7), 073902.
154. Safi, R.; Ghasemi, A.; Shoja-Razavi, R., The role of shell thickness on the exchange spring mechanism of cobalt ferrite/iron cobalt magnetic nanocomposites. *Ceramics International* **2017,** *43* (1), 617-624.
155. Meng, X.; Liu, T.; Yu, L.; Jin, K.; Xu, S., Nanocrystalline Ni 0.8 Zn 0.2 Fe 2 O 4/SrFe 12 O 19 composite fibers with enhanced exchange coupling behavior. *RSC Advances* **2015,** *5* (59), 48005-48011.
156. Volodchenkov, A.; Kodera, Y.; Garay, J., Synthesis of strontium ferrite/iron oxide exchange coupled nano-powders with improved energy product for rare earth free permanent magnet applications. *J Mater Chem C* **2016,** *4* (24), 5593-5601.
157. Dar, M. I.; Shivashankar, S., Single crystalline magnetite, maghemite, and hematite nanoparticles with rich coercivity. *RSC Advances* **2014,** *4* (8), 4105-4113.

158. Pattanayak, R.; Muduli, R.; Panda, R. K.; Dash, T.; Sahu, P.; Raut, S.; Panigrahi, S., Investigating the effect of multiple grain–grain interfaces on electric and magnetic properties of [50wt% BaFe 12 O 19–50wt% Na 0.5 Bi 0.5 TiO 3] composite system. *Physica B: Condensed Matter* **2016,** *485*, 67-77.
159. Luo, J., Structural and magnetic properties of Nd-doped strontium ferrite nanoparticles. *Materials Letters* **2012,** *80*, 162-164.
160. McCurrie, R.; Jackson, S., Angular variation of the coercivity in anisotropic barium and strontium ferrite permanent magnets. *J Appl Phys* **1987,** *61* (10), 4858-4861.
161. Ibarra-Sánchez, J. J.; Fuentes-Ramírez, R.; Roca, A. G.; del Puerto Morales, M.; Cabrera-Lara, L. I., Key parameters for scaling up the synthesis of magnetite nanoparticles in organic media: stirring rate and growth kinetic. *Industrial & Engineering Chemistry Research* **2013,** *52* (50), 17841-17847.
162. Bai, Y.; Yang, T.; Gu, Q.; Cheng, G.; Zheng, R., Shape control mechanism of cuprous oxide nanoparticles in aqueous colloidal solutions. *Powder technology* **2012,** *227*, 35-42.
163. Mrad, K.; Schoenstein, F.; Nong, T. T. H.; Anagnostopoulou, E.; Viola, A.; Mouton, L.; Mercone, S.; Ricolleau, C.; Jouini, N.; Abderrabba, M., Control of the crystal habit and magnetic properties of Co nanoparticles through the stirring rate. *Crystengcomm* **2017**.

Vita

Brent M. Williams was born in January 10, 1989 in Succasunna, New Jersey before moving to Stone Mountain, Georgia at the age of 3. He graduated from University of West Georgia in Carrollton, Georgia in 2011 with a B.S degree in Chemistry. Shortly after graduation he joined the Nanoscience and Technology program at Virginia Commonwealth University. He worked as a Research Assistant under the supervision of Dr. Everett Carpenter in the VCU Magnetics lab and was a Teaching Assistant for general, organic, and physical chemistry labs and recitations.